GROWTH AND COLLAPSE OF VAPOUR BUBBLES IN CONVECTIVE SUBCOOLED BOILING OF WATER

By

Davood Farajisarir

B.A.Sc. (Engineering) University of British Columbia, 1989

A THESIS SUBMITTED IN PARTIAL FULFILLMENT OF

THE REQUIREMENTS FOR THE DEGREE OF

MASTER OF APPLIED SCIENCE

in

THE FACULTY OF GRADUATE STUDIES

MECHANICAL ENGINEERING

We accept this thesis as conforming

to the required standard

THE UNIVERSITY OF BRITISH COLUMBIA

APRIL 1993

In presenting this thesis in partial fulfilment of the requirements for an advanced degree at the University of British Columbia, I agree that the Library shall make it freely available for reference and study. I further agree that permission for extensive copying of this thesis for scholarly purposes may be granted by the head of my department or by his or her representatives. It is understood that copying or publication of this thesis for financial gain shall not be allowed without my written permission.

(Signature)

Department of Mechanical Engineering

The University of British Columbia
Vancouver, Canada

Date April 30, 1993

DE-6 (2/88)

Abstract

The growth and collapse of vapour bubbles during convective subcooled nucleate boiling of water in an internally heated annular test section was visualized using the high speed filming technique. The experiments were performed at atmospheric pressure, mean flow velocities of *0.08- 0.8 m/s*, liquid bulk subcooling of *10-60 °C* and heat fluxes of *0.1-1.2* MW/m^2. High speed photographic results showed that bubbles grew to a maximum radius while sliding on the heated surface; condensed slowly while still attached to the heated surface; and ejected into the flow with further condensation. The bubble volume, displacement of bubble centroid parallel and normal to the heating surface, and change in the bubble maximum and minimum diameters were evaluated during the bubble lifetime. The effects of heat flux, liquid bulk subcooling and mean flow velocity on maximum bubble radius, growth time, and condensation time were investigated. At low subcoolings, an increase in the heat flux resulted in a decrease in the maximum bubble radius and growth time. At high subcoolings, the maximum bubble radius and growth time were independent of the heat flux. The effect of mean flow velocity on bubble parameters was negligible in the range of this study. Correlations are proposed for the maximum bubble radius, growth time, condensation time, and growth and collapse rates.

Table of Contents

List of Tables

List of Figures

Nomenclature

A	parameter defined in Equation (2.13)
B	parameter defined in Equation (2.13)
C_s	thermal conductivity of heater material (J/kg °C)
C_{pl}	specific heat of liquid (J/kg °C)
c	coefficient defined in Equation (4.14)
D	instantaneous diameter (m)
D_d	diameter of dry area under the bubble (m)
D_h	hydraulic diameter (m)
D_n	diameter along the centroidal principal axis normal to heater surface (m)
D_p	diameter along the centroidal principal axis parallel to heater surface (m)
F	bubble flatness, $\frac{D_p}{D_n}$
Fo	Fourier number, $\frac{\alpha_l t}{R_i^2}$
Fo_c	condensation Fourier number, $\frac{\alpha_l t_c}{R_i^2}$
g	acceleration of gravity (9.81 m/s^2)
H	thermal boundary layer thickness defined in Equation (4.2)
i_{fg}	latent heat of vaporization (J/kg)
h_{con}	convective heat transfer coefficient (W/m^2K)
h_{cb}	convective heat transfer from bubble surface (W/m^2K)
Ja	Jacob number based on liquid subcooling, $\frac{\rho_l C_{pl} \Delta T_{sub}}{\rho_v h_{fg}}$

Ja^*	Jacob number based on liquid superheat, $\frac{\rho_l C_{pl}(T_\infty - T_{sat})}{\rho_v h_{fg}}$
Ja_w^*	Jacob number based on wall superheat, $\frac{\rho_l C_{pl}(T_w - T_{sat})}{\rho_v h_{fg}}$
K	constant defined in Equation (4.4)
k_l	thermal conductivity of liquid (W/m °C)
k_s	thermal conductivity of heater material (W/m °C)
L_n	normal displacement of bubble centroid w.r.t the nucleation site (m)
L_p	parallel displacement of bubble centroid w.r.t the nucleation site (m)
l	location of the filming measured from upstream end of the heater (m)
$\dot{m}$	mass flow rate *(kg/s)*
N	constant defined in Equation (4.4)
Nu	Nusselt number, $\frac{h_{con} D_h}{k_l}$
ONB	onset of nucleate boiling
OSV	onset of significant void
P	heated perimeter (m)
p	ambient pressure (atm)
p_v	vapor pressure inside the bubble
p_∞	pressure far away from the bubble
Pe	Peclet number, $\frac{\rho_l V D_h C_{pl}}{k_l}$
Pe_b	bubble Peclet number, $\frac{2 R_i V_b}{\alpha_l}$
Pr	Prandtl number, $\frac{\mu_l C_{pl}}{k_l}$

Δp	$p_v - p_\infty$
q	heat flux (kW/m^2)
q_b	heat flux to bubble from the micro-layer (W/m^2)
R	instantaneous bubble radius (m)
R_o	initial radius of cavity (m)
$\dot{R}$	bubble growth or condensation rate (m/s)
R_i	bubble break-off radius (m)
R_m	maximum bubble radius
R_m^+	non-dimensional maximum radius defined by Equation (4.9)
R_{cav}	cavity radius
Ra_b	bubble Rayleigh number, $\frac{g(\rho_l - \rho_v)4R_i^2}{\rho_l \nu_l^2}\Pr$
Re	Reynolds number, $\frac{\rho_l V D_h}{\mu_l}$
Re_b	bubble Reynolds number, $\frac{2\rho_l V_b R_i}{\mu_l}$
St_{osv}	Stanton number at OSV, $\frac{\phi_{osv}}{\rho_l V C_{pl} \Delta T_{sub}}$
r	radial distance to the spherical element (m)
$\dot{r}$	velocity of the spherical liquid element (m/s)
T	temperature (°C)
T_B	bulk liquid temperature (°C)
T_{in}	inlet temperature (°C)
T_v	temperature of vapor inside the bubble (°C)
T_{sat}	saturation temperature (°C)
T_w	wall temperature (°C)

T_∞	superheated liquid temperature (°C)
ΔT	liquid superheat, $T_\infty - T_{sat}$ (°C)
ΔT_w	wall superheat, T_w-T_{sat} (°C)
ΔT_{sub}	liquid bulk subcooling, $T_{sat} - T_B$ (°C)
t	time
t_b	bubble lifetime (s)
t_c	bubble condensation time (s)
t_{ejc}	bubble detachment (ejection) time (s)
t_m	bubble growth time (s)
t_W	waiting time (s)
t_c^+	non-dimensional bubble condensation time defined by Equation (4.16)
t_m^+	non-dimensional bubble growth time defined by Equation (4.11)
V	mean flow velocity (m/s)
V_b	bubble velocity (m/s)
V_{ejc}	bubble ejection velocity (m/s)
Vol	measured bubble volume (m^3)
Vol_{max}	Maximum bubble volume (m^3)
v_v	specific volume of liquid (m^3/kg)
v_l	specific volume of vapor (m^3/kg)
x	coefficient defined in Equation (4.14)
Y	normal distance above the heater surface (m)
y	R/R_m
z	coefficient defined in Equation (4.14)

Greek letters

α_l	thermal diffiusivity of liquid (m^2/s)

β	non-dimensional bubble radius, $\frac{R}{R_t}$
δ	parameter defined in Equation (2.25)
ε	sphericity correction factor
ϕ	heat flux (MW/m^2)
ϕ_b	heat flux from the interface to bulk liquid defined in Equation (2.14)
$\Gamma\ (\ )$	gamma function
μ_l	liquid viscosity (Ns/m^2)
θ	non-dimensional temperature defined by Equation (4.8)
ρ_l	liquid density (kg/m^3)
ρ_s	density of heater material (kg/m^3)
ρ_v	density of vapor at saturation (kg/m^3)
ρ^*	non-dimensional density, $\frac{\rho_l - \rho_v}{\rho_l}$,defined in Equation (2.25)
σ_l	liquid surface tension (N/m)

Subscripts

B	bulk
b	bubble
c	condensation
cav	cavity
con	convective
d	dry area
ejc	ejection
h	hydraulic

in	inlet
l	liquid
m	at the end of growth stage
max	maximum
n	normal
p	parallel
s	solid
sat	saturation
sub	subcooling
W	waiting
w	wall
o	initial
∞	far away

Superscripts

+	non-dimensional quantity
*	non-dimensional quantity
•	rate of change

Acknowledgment

I would like to thank my supervisor, Dr. Martha Salcudean, for her continued support and trust through all stages of this work. I would also like to thank Dr. Yacov Barnea for his suggestions and contributions during the analysis of data and thesis write-up and Eric Bibeau for his generous help during high-speed filming. Technical advice of Don Bysouth in digital image processing and Ed Abell and Tony Besic during various stages of the experimental setup is greatly appreciated. I also wish to thank my family and friends for their support, especially Glenn Stefurak and Zenebe Gete for their continous encouragement and Penny Syroid for her love and understanding during this rewarding experience.

CHAPTER 1

INTRODUCTION

The phenomenon of convective subcooled boiling is important in the design of nuclear reactors which use a liquid coolant that is subjected to high heat fluxes. In some of these reactors, the surface boiling is designed into the system or allowed to occur at high loads to increase heat transfer whereas in others the surface boiling is avoided in normal operation but may be allowed only under emergency and transient conditions. The effect of void[1] formation on the reactivity of the system is described by the void coefficient of reactivity. Depending on the design of the reactor and its moderator-to-fuel ratio, a reactor can have a positive or a negative void coefficient of reactivity[1]. In a reactor with a negative void coefficient, an increase in the amount of void in the system results in a decrease in the reactivity of the system.

SLOWPOKE and MAPLE low-pressure, pool-type nuclear reactors, designed by AECL, belong to a class of reactors with negative coefficient of reactivity[2]. The power output of these reactors depends on the density of the moderator (water) which is a function of the volume fraction of the vapour in the flow, expressed as void fraction. These reactors are so designed that, in case of emergencies when the probability of power excursions is high, surface boiling occurs along the fuel rod and the increased void fraction in the moderator causes a decrease in reactivity. In this way the power output of the reactor is controlled to safe levels. Therefore, the evaluation of the volume of steam,

---

[1] In nuclear industry, vapor generated during the process of surface boiling is termed as 'void'.

produced during the process of subcooled flow boiling, is critical for operation of water-moderated low pressure nuclear reactors.

Evaluation of the void fraction has been the subject of many studies in the high-pressure range of operation of commercial nuclear-powered reactors. The development of low-pressure nuclear reactors motivated the study of void fraction at atmospheric pressure. Void fraction experiments conducted at low pressure have revealed differences in the mechanism of void formation between high and atmospheric pressures. This study is part of an extensive project undertaken at the University of British Columbia in collaboration with Atomic Energy Canada Limited, to study the void growth at atmospheric pressure. This thesis presents the results of flow visualization experiments of vapour bubbles generated in the process of subcooled boiling at atmospheric pressure. The flow visualization experiments were carried out to obtain insight on the mechanisms of void growth at atmospheric pressure.

1.1 Void Fraction in Convective Subcooled Boiling

Subcooled boiling is characterized by the growth of vapour bubbles at a heated solid surface and their subsequent condensation or collapse inside the subcooled liquid. These bubbles originate at cavities, pits and scratches on the heater surface where vapour or non-condensable gases are trapped. When the temperature at the liquid-solid interface exceeds the saturation temperature by a few degrees, nucleation sites become active and boiling commences. An active nucleation site produces vapour bubbles which go through a typical periodic cycle of nucleation, growth, departure and collapse (condensation) followed by a waiting period (Figure 1.1). This cycle, repeated hundreds of time in a second, and at hundreds of different locations on the heater rod, results in a two-phase mixture of liquid and vapour.

Figure 1.2 shows schematically the process of subcooled flow boiling and void growth in a vertically mounted annular channel with internal heating used in this study. The single-phase subcooled liquid enters the test section and flows upward parallel to the heater. At some distance downstream where the wall temperature exceeds the saturation temperature by a few degrees, the nucleation sites on the heater become active and bubbles form on the heater. This point is referred to as ONB or Onset of Nucleate Boiling and signifies the first appearance of the vapour bubbles. As the liquid flows past ONB and moves further downstream, the amount of vapour in the mixture increases. The volume fraction of the vapour in the flow is termed 'void fraction' which is defined as the ratio of area occupied by vapour over the total cross-sectional flow area. The void fraction increases in the direction of the flow up to the point of OSV (Onset of Significant Void) which signifies a sudden increase in the void fraction. The point of OSV indicates the condition at which the amount of void increases exponentially and its prediction is critical to the modeling of void growth. The void fraction in the system is dependent on the average bubble size, average bubble lifetime, growth rate and condensation rate of bubbles, number of nucleation sites, and the frequency of bubble formation. These parameters, in turn, are dependent on experimental conditions such as heat flux, pressure, mass flow rate and liquid subcooling.

1.3 Research Background

The project originated at the University of Ottawa with the measurement of void fraction using the Gamma ray attenuation method. Void fraction measurements, conducted in an annular test section with internal heating at atmospheric pressure and low flow rate simulated the flow geometry and conditions in the SLOWPOKE reactors [3,4,5]. The experimental data were compared to various void fraction models derived from high-pressure experiments without satisfactory results[4]. Further experiments were performed

at the University of British Columbia for different hydraulic diameters of the test section for upflow and downflow [6,7,8]. It was concluded that the discrepancies between the measured results and those calculated from the existing models were probably because of the differences in the hydrodynamics and heat transfer mechanisms at low pressure:

- At low pressure the bubble detachment did not coincide with OSV.
- The void prior to OSV was not negligible.

The research continued at the University of British Columbia in the modeling of void fraction at low pressure[9]. A model was proposed to 'account' for all the bubbles that are generated and condensed in the flow. The present work, carried out as a complement to the 'bubble accounting model', evaluates the characteristic bubble parameters employed in the model. Moreover, in void growth models, a correlation for the generation and condensation rate of vapour is required[4,10,11,12]. Usually these terms are approximated without a physical basis. Nevertheless, a constant need exists to express the generation and condensation terms for vapour in terms of basic bubble parameters. This study also evaluates the growth and condensation rates for bubbles generated and condensed during the process of subcooled flow boiling at atmospheric pressure.

1.4 Research Objectives

- Flow visualization using high speed photography of vapour bubbles generated on a heated surface for different flow conditions. The mass flow rate, inlet subcooling and heat flux would be changed systematically so that the effect of each parameter on the bubble growth and collapse could be investigated.

- Design an efficient method for analyzing images of the bubbles with the aid of a computer.

- Quantify the effect of experimental conditions on the maximum bubble size, growth time, condensation time, and growth and collapse rates.

- Investigate the applicability of available models of bubble growth and collapse to the present research.

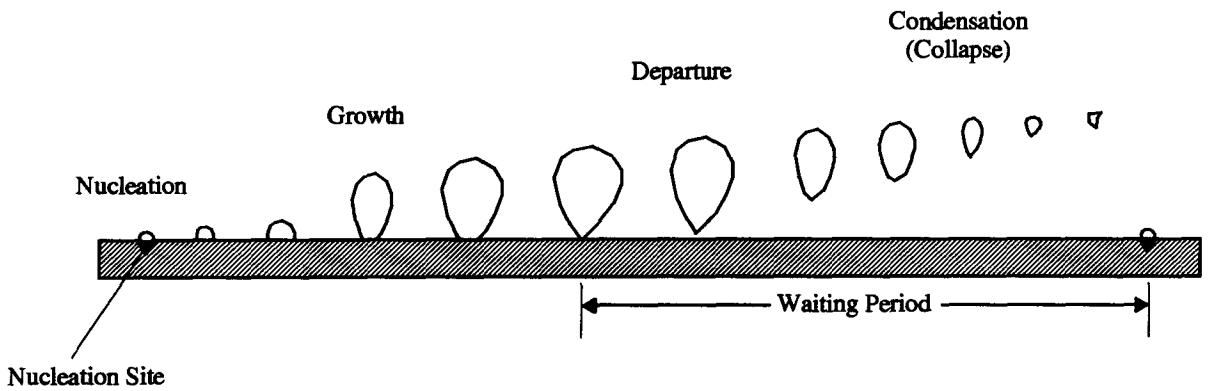

(a)

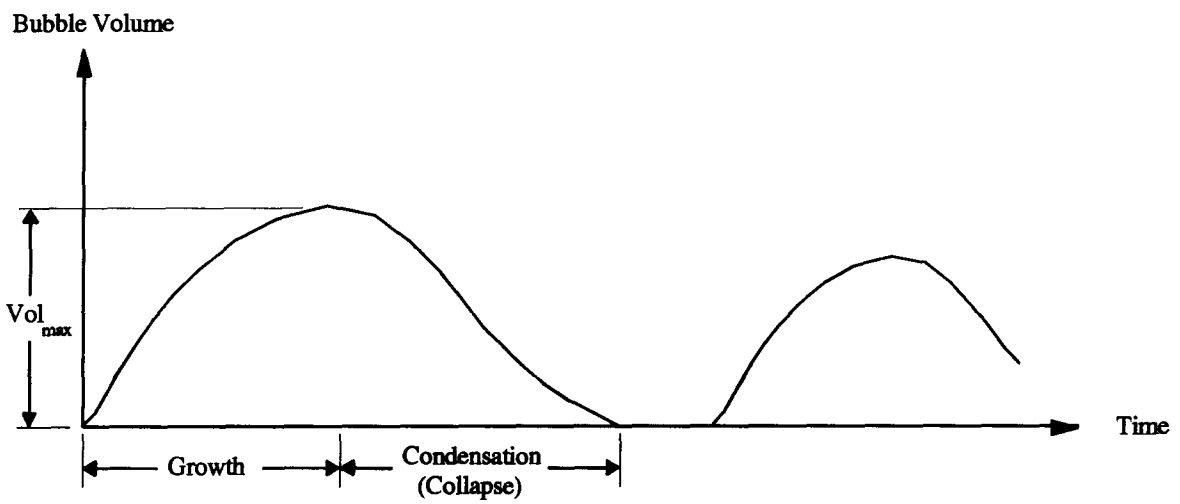

(b)

Figure 1.1. Bubble behavior in subcooled nucleate boiling (a) Schematic diagram of bubble growth and collapse process (b) Typical bubble growth and collapse curve.

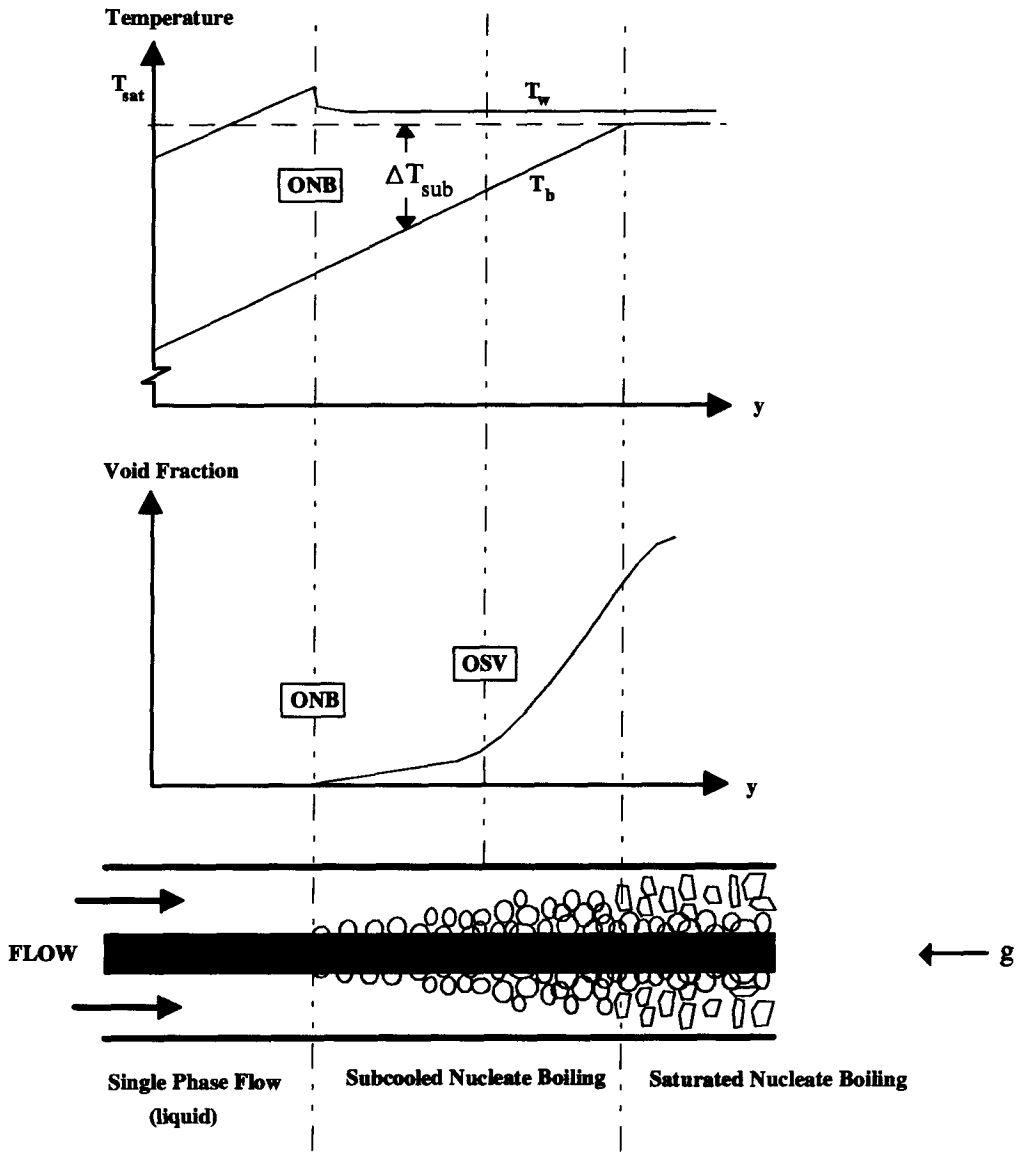

Figure 1.2. Void fraction, wall temperature, and liquid bulk temperature along an internally heated channel.

CHAPTER 2

LITERATURE REVIEW

The augmentation of heat transfer to the liquid during subcooled boiling is attributed to the processes of growth and collapse of bubbles during which the adjacent liquid is violently agitated and latent heat of vaporization is transferred to the liquid[13]. Ascertaining the relative importance of these two heat transfer mechanisms, requires a knowledge of the heat transfer during growth and condensation of a bubble. This has led to the development of mathematical models and experimental investigations of bubble growth and collapse rates in subcooled and superheated liquids.

The growth of a bubble is defined as the macroscopic (visible) expansion of the bubble boundary on the heater surface beyond the boundary of the cavity. Research on the mechanism and physics of bubble growth has led to three points of view[14,15]:

- Inertia-controlled growth;
- Growth due to heat transfer at the liquid-vapour interface on the bubble surface;
- Growth by micro/macro-layer evaporation at the bubble base.

The driving force for bubble growth in an inertia-controlled process is the pressure difference between the inside and outside of the bubble. In heat-transfer-controlled growth, the growth is due to the evaporation of liquid at the liquid-vapour interface on bubble surface, whereas in micro/macro- layer evaporation theory, the evaporation from the thin liquid formed at the bubble base is considered to account for all the vapour inside the bubble.

The following methods are reported in the literature for studying bubble growth and collapse rates[16]:

1. Injection of saturated vapour in uniformly superheated or subcooled liquid;
2. Local heating of a surface by laser beam or electric pulse;
3. Nucleation from prepared sites;
4. Nucleation from a random site during actual boiling.

The study of bubble growth and collapse is facilitated by the use of the first three methods since the complexity of the nucleation process is avoided and interaction between nucleation sites is eliminated. In the present study, the bubble growth and collapse is studied from a random nucleation site during actual subcooled boiling.

This chapter reviews the different bubble growth mechanisms, presents flow visualization experiments of bubble growth and collapse in flow boiling, and outlines the experimental correlations for the condensation of bubbles injected into the subcooled liquid.

2.1 Inertia-Controlled Bubble Growth

In an inertia-controlled bubble growth process, a vapour bubble in a uniformly superheated liquid is idealized as a sphere expanding from an initial radius R_o to R in an infinite, incompressible, non-viscous liquid with constant excess pressure. The conservation of mechanical energy with these assumptions yields the following equation[17]:

$$\frac{1}{2}\rho_l \int_R^\infty 4\pi r^2 \dot{r}^2 dr = \frac{4\pi}{3}(R^3 - R_o^3)\Delta p \tag{2.1}$$

where $\Delta p = p_v - p_\infty$. This equation, combined with the continuity requirement $\left(r/R\right)^2 = \left(\dot{R}/\dot{r}\right)$, results in the inertia-controlled bubble growth equation known as the Rayleigh's equation:

$$R\ddot{R} + \frac{3}{2}\dot{R}^2 = \frac{\Delta p}{\rho_l} \tag{2.2}$$

A solution to (2.2) is approximated by the following[15]:

$$R \cong \left(\frac{2\Delta p}{3\rho_l}\right)^{1/2} t \tag{2.3}$$

The vapour inside the bubble is assumed to be at the saturated state corresponding to the temperature of superheated liquid (Figure 2.1). As long as this assumption holds, the vapour pressure inside the bubble will exceed the ambient pressure and cause the bubble boundary to expand outward. The pressure difference in Equation (2.3) is approximated with the Clausius-Clayperon equation:

$$\frac{\Delta P}{\Delta T} = \frac{i_{fg}}{T_{sat}(v_v - v_l)} \tag{2.4}$$

where $\Delta T = T_\infty - T_{sat}$. Applying this approximation in Equation (2.3) yields:

$$R \cong \left(\frac{2}{3} Ja^* \frac{\rho_v^2 h_{fg}^2}{\rho_l^2 C_{pl} T_{sat}}\right)^{1/2} t \tag{2.5}$$

where $Ja^* = \dfrac{\rho_l C_{pl} \Delta T}{\rho_v i_{fg}}$.

2.2 Heat-Transfer-Controlled Bubble Growth

2.2.1 Bubble Growth in Uniform Temperature

In heat-transfer-controlled growth it is assumed that the growth of the bubble occurs due to the evaporation at the liquid-vapour interface at the bubble surface on account of heat supplied from the superheated liquid by conduction through the boundary layer. In this case the temperature of the vapour inside the bubble is assumed to be at the saturation

temperature corresponding to the ambient pressure (Figure 2.2). A simple energy balance at the interface ($x = 0$) of a spherical bubble yields:

$$\rho_v i_{fg} \dot{R} = k_l \left(\frac{\partial T}{\partial x} \right)_{x=0} \tag{2.6}$$

The temperature gradient at the interface is approximated by the one-dimensional transient heat conduction formulation for a homogeneous semi-infinite body with a plane boundary, i.e.:

$$\frac{1}{\alpha_l} \frac{\partial T}{\partial t} = \frac{\partial^2 T}{\partial x^2} \tag{2.7}$$

with initial and boundary conditions:

$$t = 0 : T(x,0) = T_\infty$$
$$t > 0 : T(0,t) = T_{sat}$$
$$t > 0 : T(\infty,t) = T_\infty$$

The solution of (2.7) combined with the energy balance (2.6) results in an expression for the bubble growth rate for the heat-transfer-controlled mode known as the Bosnjakovic equation:

$$\rho_v i_{fg} \dot{R} = k_l \frac{T_\infty - T_{sat}}{\sqrt{\pi \alpha_l t}}. \tag{2.8}$$

Integrating (2.8) along a time period t, the bubble radius is expressed as [18]:

$$R = 2 \frac{\sqrt{\pi}}{\pi} Ja^* \sqrt{\alpha_l t} = 2 \frac{\sqrt{\pi}}{\pi} \left(\frac{\rho_l c_{pl} \Delta T}{\rho_v i_{fg}} \right) \sqrt{\alpha_l t} \tag{2.9}$$

Plesset and Zwick[19] and Forster and Zuber[20] extended Rayleigh's equation (2.2) to account for both the inertia- and heat-transfer-controlled growth as well as the surface tension effect which were ignored both in (2.2) and (2.6):

$$\rho_l \left(R\ddot{R} + \frac{3}{2} \dot{R}^2 \right) = \left(p_v(T) - p_\infty \right) - \frac{2\sigma}{R} \tag{2.10}$$

where $p_v(T)$ is the pressure inside the bubble and p_∞ is the pressure of the liquid surrounding the bubble. The momentum equation is therefore coupled to the energy equation through the vapour temperature. To obtain a solution, the Clausius-Clapeyron equation was used to relate the pressure difference to the temperature difference. A transient heat conduction equation with a moving spherical boundary was used to evaluate the temperature of the interface[20,21]. The asymptotic solution, valid at large values of radius, was obtained by assuming that the bubble wall temperature falls rapidly to the saturation temperature. This drop in temperature from superheated to saturation is assumed to occur in a "thin boundary layer" near the bubble wall. The solution of (2.10) was given for the heat transfer-controlled growth as follows:

$$R \cong \pi^{\frac{1}{2}} Ja^* \sqrt{\alpha_l t} \qquad \text{(Forster - Zuber)} \tag{2.11}$$

$$R \cong \left(12/\pi\right)^{\frac{1}{2}} Ja^* \sqrt{\alpha_l t} \quad \text{(Plesset - Zwick)} \tag{2.12}$$

The different constants in Equations (2.11) and (2.12) are due to different mathematical schemes used to evaluate the temperature of the interface. These solutions are the same as (2.9) except for the value of the constants mainly because the spherical boundary condition was used in the evaluation of the bubble wall temperature. The larger values of the constant in (2.11) and (2.12) compared to (2.9) implies that the effect of curvature is to increase the rate of bubble growth.

In a different approach, Mikic et al.[22] derived a non-dimensional relation that was applicable in the whole range of inertia-controlled to heat transfer-controlled growth:

$$R^+ = \frac{2}{3}\left[\left(t^+ + 1\right)^{3/2} - \left(t^+\right)^{3/2} - 1\right] \tag{2.13}$$

where

$$R^+ = \frac{A}{B^2} R \qquad and \qquad t^+ = \frac{A^2}{B^2} t.$$

The definitions of A and B are given in Appendix A with the derivation of (2.13). This relation reduces to (2.3) for $t^+ << 1$ and to (2.12) for $t^+ >> 1$.

Figure 2.3 compares the growth rates obtained from Equations (2.5), (2.9), (2.11), (2.12), and (2.13). The growth rate predicted by the inertia-controlled growth model is substantially higher than the predictions of the heat-transfer-controlled models for the same Ja^*. The growth rates predicted by Mikic et al.[22], Forster and Zuber[20], and Plesset and Zwick[21] are in good agreement with each other whereas the Bosnjakovic solution predicts substantially lower growth rate.

2.2.2 Bubble Growth in Non-Uniform Temperature

The models mentioned above were based on the assumption that the growth of a vapour bubble occurs in a stagnant uniform superheated liquid. However, the actual process of subcooled boiling involves a temperature gradient at the vicinity of the wall so that the liquid near the wall is superheated which decreases in temperature to the subcooled temperature in the core. None of the above models predict the maximum diameter reached in subcooled boiling. However, they are a basis for more complicated models that consider non-uniform temperature fields and predict the maximum bubble radius. The common feature of models for non-uniform temperature fields is that the controlling factor is the heat transfer at the interface rather than the liquid inertia and surface tension.

Zuber[23] expressed the non-uniformity in the liquid temperature by including an additional term, ϕ_b, to account for the heat transfer from the vapour interface to the bulk liquid in Equation (2.8):

$$\rho_v i_{fg} \dot{R} = \varepsilon k_l \frac{T_\infty - T_{sat}}{\sqrt{\pi \alpha_l t}} - \phi_b \tag{2.14}$$

where $\varepsilon = \pi/2$ is a correction factor for the sphericity of the bubble. Zuber assumed that the additional heat flux term was approximately the same as the wall heat flux since the

temperature gradient between the vapour phase and liquid was equal to the temperature gradient which existed between the solid and liquid immediately before nucleation. Zuber obtained a non-dimensional relation for bubble radius by integrating (2.14) and normalizing with the maximum radius:

$$\frac{R}{R_m} = \sqrt{\frac{t}{t_m}}\left(2 - \sqrt{\frac{t}{t_m}}\right) \tag{2.15}$$

The maximum radius, R_m, and growth time, t_m, are given by:

$$R_m = \frac{\rho_l c_{pl}(T_w - T_{sat})}{2\rho_v i_{fg}}\sqrt{\pi\alpha_l t_m} = \frac{1}{2} Ja_w^* \sqrt{\pi\alpha_l t_m} \tag{2.16}$$

where,

$$\sqrt{\pi\alpha_l t_m} = \frac{k_l(T_w - T_{sat})}{q}. \tag{2.17}$$

where q is the wall heat flux.

Mikic and Rohsenow[24] expressed the temperature non-uniformity in the liquid as a function of the waiting time, t_W, and thermophysical properties of the liquid. Mikic et al. used one-dimensional transient conduction equation to evaluate the bubble wall temperature and the sphericity of the bubble was taken into account by the use of a correction factor ($\varepsilon = \sqrt{3}$):

$$\rho_v i_{fg}\dot{R} = \varepsilon k_l\left\{\frac{T_w - T_{sat}}{\sqrt{\pi\alpha_l t}} - \frac{T_w - T_b}{\sqrt{\pi\alpha_l (t + t_W)}}\right\} \tag{2.18}$$

The waiting time, t_W, was expressed in terms of the growth time by observing that at $t = t_m, \dot{R} = 0$. The bubble radius is formulated in a non-dimensional form:

$$\frac{R}{R_m} = \frac{\left(\frac{t}{t_m}\right)^{1/2}\left\{1 - \theta\left\{\left(1 + (\theta^2 - 1)\frac{t_m}{t}\right)^{1/2} - \left((\theta^2 - 1)\frac{t_m}{t}\right)^{1/2}\right\}\right\}}{1 - \theta\left(\theta - (\theta^2 - 1)^{1/2}\right)} \tag{2.19}$$

The maximum radius is:

$$R_m = \frac{2}{\pi}\sqrt{3}Ja_w^*\sqrt{\pi\alpha_l t_m}\{1-\theta[\theta-(\theta^2-1)^{\frac{1}{2}}]\} \tag{2.20}$$

where $\theta = \frac{T_w - T_b}{T_w - T_{sat}}$ represents the degree of subcooling and $Ja_w^* = \frac{\rho_l C_{pl}(T_w - T_{sat})}{\rho_v i_{fg}}$.

Figure 2.4 compares the growth and collapse rates obtained from (2.15) and (2.19) for different values of subcooling. The models agree well for bubble growth, however, Mikic's model results in smaller collapse rates than Zuber's model for $\theta < 4.5$. For higher values of θ (indicating higher degree of subcooling) both theories predict similar collapse rates. In Mikic's model the growth rate is insensitive to the change in the degree of subcooling.

2.3 Micro-Macro Layer Evaporation

Other researchers[25-29], assumed that most of the evaporation during bubble growth occurs at the bubble base between the vapour-liquid interface and the heater surface where a very thin liquid is formed. The evaporation from the bubble surface due to conduction from the superheated liquid is assumed to contribute little to bubble growth since the thickness of the superheated layer was found to be much smaller than that of the maximum radius attained by the bubble[26]. Unal[28] applied this model to bubble growth during the process of convective subcooled boiling. It was assumed that a spherical bubble grows on the wall by the evaporation of liquid into vapour at the dried patch while dissipating heat by condensation to the surrounding liquid at its upper half (Figure 2.5). The following heat balance equation is presented by Unal:

$$q_b \frac{\pi D^2}{4}(1-\frac{D_d^2}{D^2}) = h_{cb}\Delta T_{sub}\frac{\pi D^2}{2} + \frac{\pi}{6}\rho_v i_{fg}\frac{dD^3}{dt} \tag{2.21}$$

where q_b is the heat flux to the bubble from the very thin liquid film under it, and h_{cb} is the heat transfer coefficient for condensation at the surface of the bubble. The final expression for the bubble radius is cast into a non-dimensional form:

$$\frac{R}{R_m} = 1.368\left(\frac{t}{t_m}\right)^{1/2} \frac{1 + 0.228\, t/t_m}{1 + 0.685\, t/t_m} \tag{2.22}$$

The derivation and solution for the maximum radius and growth time for this model are given in Appendix B.

In Figure 2.4, Unal's model is compared with Equations (2.15) and (2.19). Unal's model predicts lower growth rates and unlike the other two models, fails to predict a maximum radius.

2.4 Bubble Condensation (Collapse) Models

The collapse or condensation of a bubble is defined as the decrease in the size of the bubble from its maximum size at the end of the growth stage to undetectable microscopic size. Similar to the growth stage, the bubble collapse is categorized into the inertia-controlled and the heat-transfer-controlled modes.

Akiyama[30] solved the extended Rayleigh's Equation (2.10) for the condensation of a spherical bubble in stagnant, uniform subcooled liquid with the initial condition of $t = 0: R = R_m, \dot{R} = 0$. For an inertia-controlled process, the condensation rate was given in terms of the Gamma function:

$$\frac{t}{t_c} = 3\frac{\Gamma(\frac{4}{3})}{\Gamma(\frac{5}{6})\Gamma(\frac{1}{2})} \int_y^1 \frac{y^{3/2}}{(1-y^3)^{1/2}} dy \tag{2.23}$$

where $y = R/R_m$ and

$$t_c = \sqrt{\frac{1}{6\delta}} \frac{\Gamma(\frac{5}{6})\Gamma(\frac{1}{2})}{\Gamma(\frac{4}{3})} \tag{2.24}$$

$$\delta = \frac{g}{4.186 R_m^2} \frac{i_{fg}\Delta T_{sub}}{T_{sat}(v_v - v_l)\rho^* \rho_l} \tag{2.25}$$

Zuber[23] solved Rayleigh's equation (2.2) for the condensation of a spherical bubble in subcooled liquid and reached a similar result:

$$\frac{t}{t_c} = 1 - \frac{\int_0^y \frac{y^{3/2} dy}{(1-y^3)^{1/2}}}{\int_0^1 \frac{y^{3/2} dy}{(1-y^3)^{1/2}}} \tag{2.26}$$

Analysis of the heat-transfer-controlled condensation process was given by Florschuetz and Chao[31] by solving (2.10) for the heat transfer controlled bubble collapse and by Voloshko and Vurgaft[32] using Bosnjakovic's simpler analysis. The condensation rate is given as follows:

$$\frac{R}{R_m} = 1 - \left(\frac{t}{t_c}\right)^{1/2} \tag{2.27}$$

where

$$t_c = \frac{\pi}{4\alpha_l} \frac{R_m^2}{Ja^2}. \tag{2.28}$$

Figure 2.6 compares the condensation rates obtained by (2.23), (2.26) and (2.27). Akiyama's and Zuber's equations compare well with each other as expected; however, they differ drastically from the heat-transfer-controlled models of Florschuetz et al. and Voloshko et al.. In heat-transfer-controlled collapse the condensation rate is rapid at the beginning and slows at the end of condensation process whereas in the inertia-controlled model, the condensation rate is initially slow and substantially faster at the end.

The condensation time predicted by Akiyama[30] and Florschuetz and Chao[31] are shown in Figure 2.7 as a function of subcooling for different maximum radii. The predictions by Florschuetz et al. were at least one order of magnitude higher than those of Akiyama at low subcoolings but matched Akiyama's values at higher subcoolings *(60 °C)* for small values of maximum radii.

2.5 Flow Visualization Studies of Bubble Growth and Collapse

The survey of experimental studies on bubble growth and collapse showed that very few of the flow visualization experiments were performed to visualize bubble dynamics during void growth experiments. Unal[33] and Shoukri et al.[34] used a high speed filming technique to study the effect of different flow conditions on the bubble population in void growth experiments. Aside from these studies, other researchers concentrated on visualization of bubble dynamics and behavior which led to burnout condition or enhancement of heat transfer. Most of the experiments on convective boiling were performed at higher velocities and heat fluxes.

Table 2-1 summarizes flow visualization studies of vapour bubbles during convective subcooled boiling of water with the high speed filming technique. In a pioneer study, Gunther[35] studied the influence of heat flux, liquid subcooling, and mass flow rate on bubble size, lifetime and population during convective subcooled boiling. The test section consisted of a *0.10 mm* metal strip suspended lengthwise inside a vertical transparent channel of rectangular cross-section. The metal strip divided the channel into two flow passages and boiling occurred on both sides of the metal strip. The experiments were done at higher flow velocities and heat flux than those used in the present study. The surface boiling activity in these experiments, consisted of small hemispherical vapour bubbles which grew and collapsed (while still attached to the heating surface) sliding downstream under the influence of the coolant flow. At high heat fluxes, the bubble population increased to the limit at which bubbles coalesced to form vapour clumps on the heated surface. The effect of increasing heat flux, subcooling and mass flow rate was to decrease the maximum bubble size and the average bubble lifetime. For instance, bubble size and lifetime decreased by *40%* with an increase of heat flux from ONB $(2.4\ {}^{MW}/_{m^2})$ to the burnout condition $(10.4\ {}^{MW}/_{m^2})$ at flow velocity of *3 m/s* and subcooling of *85 °C*. At near burnout condition, the bubble frequency was estimated at *1000* bubbles per second

for subcooling of *85 °C*. No correlations were given to generalize the findings to lower flow velocities and heat flux.

Tolubinsky and Kostanchuk[39] investigated the effect of subcooling and pressure on maximum bubble size and frequency of bubble formation at low flow rates. The test section was made of an electrically heated stainless steel plate *0.25 mm* thick positioned inside a horizontal channel with rectangular cross-section. Bubble frequency and size decreased with increasing subcooling and pressure. Bubble size and lifetime were independent of heat flux, in contradiction of Gunther's results. The frequency of bubble formation was reported to be *100* bubbles/second for subcooling of *5 °C* and *400* bubbles/second for subcooling of *60 °C* at flow velocity of *0.2 m/s* and atmospheric pressure. The effect of flow velocity was not reported.

Abdelmessih et al.[36] studied the effect of flow velocity on the growth and collapse of bubbles in slightly subcooled water *(2 °C)* during surface boiling. The test section consisted of an electrically heated stainless steel strip, *0.15 mm* thick insulated on its undersurface, and was positioned concentrically inside a vertical channel of circular crossection. An artificial nucleation site was constructed by making a depression of *0.18 mm* in diameter on the heated surface. The bubbles slid on the heater surface while changing shape and detached from the surface with a shape of an inverted pear. An increase in the flow velocity resulted in a decrease in bubble lifetime and average bubble radius. However, increasing the heat flux resulted in an increase in bubble size and lifetime, in contradiction of the result of Gunther[35] and Tolubinsky and Kostanchuk[39]

Akiyama and Tachibana[38] investigated the effect of flow velocity and subcooling on the maximum bubble size, lifetime and growth time in an annular channel similar to that of the present study for a wide range of flow rates and subcoolings. The circular heated section was made of stainless steel of *0.2 mm* thickness. The hydraulic diameter of the test section was twice the one used in the present study. It was concluded that the effect of forced convection was important only at velocities higher than *0.3 m/s* (see Figure 2.8).

Moreover, the distribution of the liquid temperature normal to the heating surface was investigated. The temperature gradient in the thermal boundary layer was controlled by the mass flow rate and was independent of the heat flux. The thickness of the superheated layer was estimated to be smaller than *0.2 mm* for flow velocity range of *0.1-5 m/s*. The effect of the heat flux on bubble parameters was not described in this study.

Del Valle and Kenning[37] investigated the bubble size, lifetime, frequency and the pattern of the interaction of nucleation sites at constant flow velocity of *1.7 m/s* and subcooling of *84 °C* for high heat fluxes. The test section consisted of an electrically heated stainless steel plate, *0.08 mm* thick, set into one side of a vertical flow channel of rectangular cross-section. The surface boiling activity, unlike in Gunthers' observations, consisted of bubbles growing and collapsing at their nucleation sites without sliding on the heated wall. At higher heat flux, activation of nucleation sites became irregular and many sites were observed to become inactive, although some sites were reactivated with further increase in heat flux. The waiting time was estimated to be *0.9-2.9 ms* and the maximum radius was found to be normally distributed. Maximum bubble size and bubble lifetime were independent of heat flux confirming the results of Tolubinsky and Kostanchuk[39].

Other researchers[16, 40-44] studied only the bubble condensation by injecting bubbles inside stagnant subcooled liquid. Table 2.2 presents the experimental correlations given by these experiments for condensation rate and time of bubbles after detachment from the orifice. The initial bubble radius in these experiments is much larger than that encountered in the actual process of subcooled boiling.

Apparently, the experimental observations of bubble behavior and the effect of flow conditions on bubble parameters differ from study to study. However, researchers have shown that surface boiling is a local effect and is dependent on many parameters e.g., heat flux, liquid subcooling, pressure, surface quality, thermal boundary layer thickness, interaction between the nucleation sites, and the amount of dissolved air in the system. Moreover, surface boiling is a statistical process in which the bubble lifetime and bubble

sizes are statistically distributed. These complexities of the boiling process necessitate more investigations on the effect of different experimental conditions on bubble parameters.

Table 2.1 Flow visualization studies of vapour bubbles in subcooled flow boiling.

Investigator	Channel Geometry	$p(atm)$	$\phi(MW/m^2)$	$V(m/s)$	$\Delta T_{sub}(°C)$
Gunther[35]	rectangular	*1.7*	*2.3 - 10.7*	*1.5 - 6.1*	*33 - 110*
Tolubinsky[39]	rectangular	*1-10*	*0.05 - 1.0*	*0.08 - 0.2*	*5 - 60*
Del Valle et al.[37]	rectangular	*1*	*3.44 - 4.67*	*1.7*	*84*
Abdelmessih et al.[36]	cylindrical	*1*	*0.19 - 0.46*	*0.92 - 2.30*	*1.9*
Akiyama[38]	annular	*1*	*0.1-0.8*	*0.1 - 5*	*20-80*
Unal[28]	annular	*1 - 177*	*0.47 - 10.64*	*0.08 - 9.15*	*3 - 86*
Present Investigation	annular	*1*	*0.1-1.2*	*0.08 - 0.80*	*10 - 60*

Table 2.2 Correlations for condensation rate and time for injected bubbles into uniformly subcooled liquid.

Investigator	$p(atm)$	ΔT_{sub} (°C)	$R_i(mm)$	Condensation time	Condensation rate
Brucker et al.[44]	*10.3-62.1*	*15-100*	*1.5*	$Fo_c = 55.5\,Ja^{-3/4}Ra_b^{-1/2}$	
Mayingeret al.[16]	*1*	$1<Ja<120$	*2*	$Fo_c = 1.784\mathrm{Re}_b^{-0.7}\,\mathrm{Pr}^{-0.5}\,Ja^{-1.0}$	$\beta = (1-0.56\mathrm{Re}_b^{0.7}\,\mathrm{Pr}^{0.5}\,Ja\,Fo)^{0.9}$
Simpson et al.[43]	*1-2*	*5-36.6*	*4*	$Fo_c = 0.263Ja^{-1.0}Pe_b^{0.5}$	$\beta = (1-4.35Ja^{1.1}Pe_b^{0.55}Fo^{1.1})^{0.67}$
Kamei et al.[40,41]	*1-10*	*10-70*	*5*	$Fo_c = 55.5\,Ja^{-3/4}Ra_b^{-1/2}$	
Voloshko et al.[32]	*1*	$40<Ja<75$	*5 - 12.5*	$Fo_c = 5.90\times10^{-5}$	$\beta = 1-1.694\times10^{4}\,Fo$

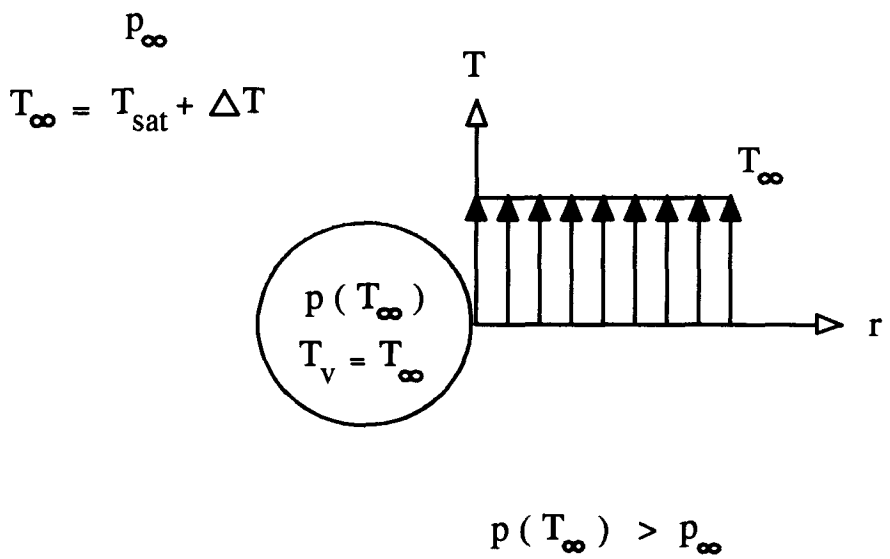

Figure 2.1. Schematic diagram of inertia-controlled bubble growth.

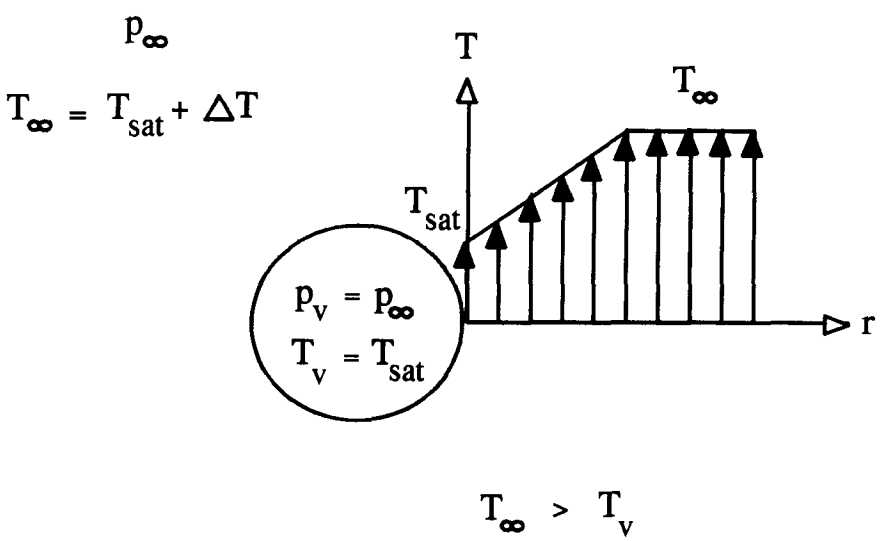

Figure 2.2. Schematic diagram of heat-transfer-controlled bubble growth.

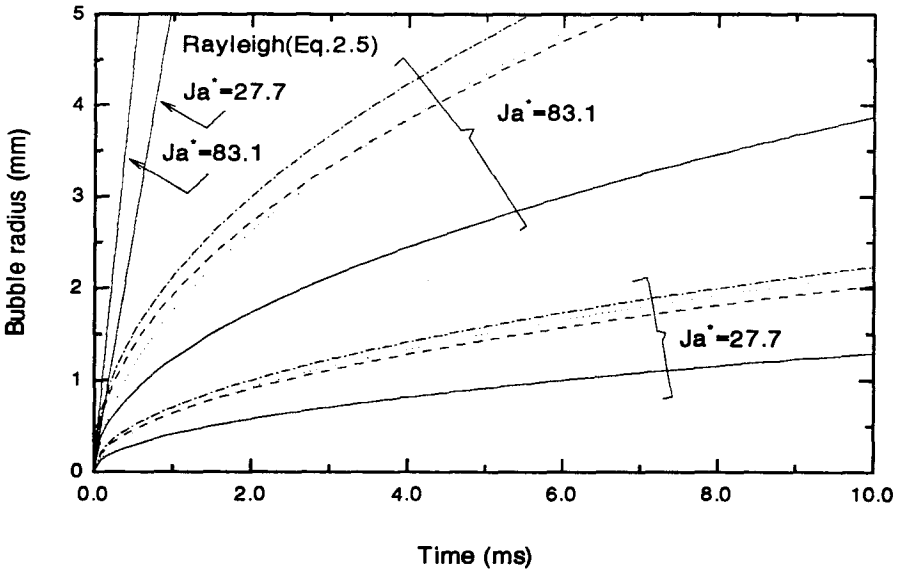

Figure 2.3. Comparison of bubble growth models in uniformly superheated liquid - — - — -Plesset and Zwick[19], ... Mikic et al.[22], ——— Bosnjakovic (Equation 2.9), ------ Forster and Zuber[20] and Rayleigh (Equation 2.5).

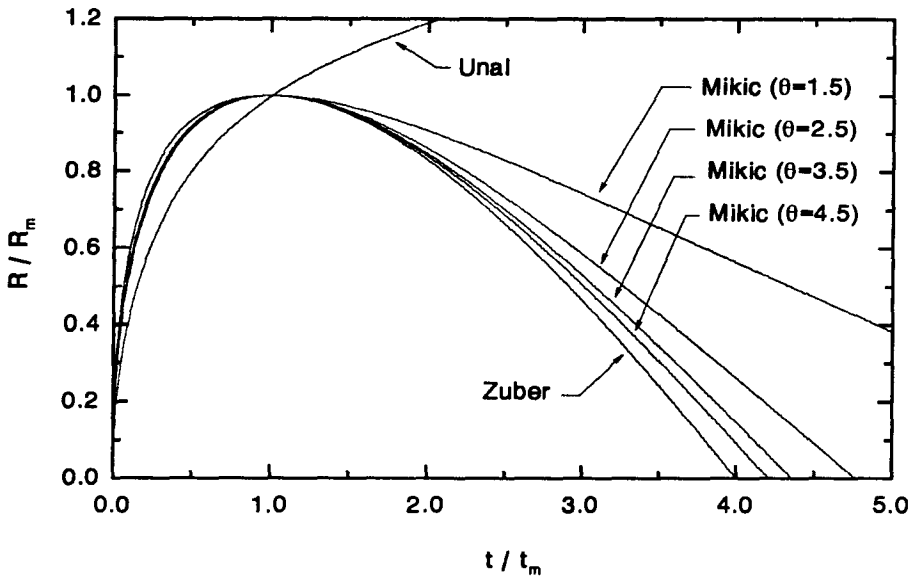

Figure 2.4. Comparison of bubble growth models in non-uniform temperature (Mikic et al.[24], Zuber[23] and Unal[28]).

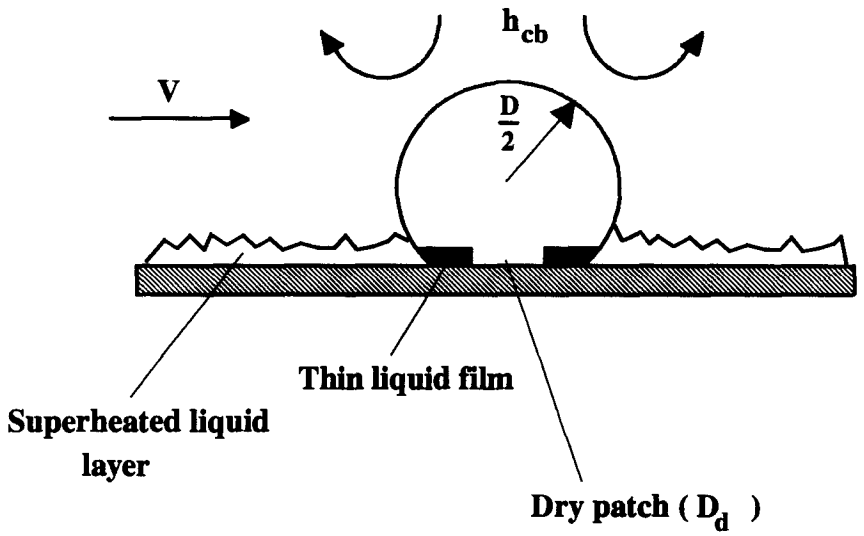

Figure 2.5. Schematic diagram of bubble growth model proposed by Unal[28].

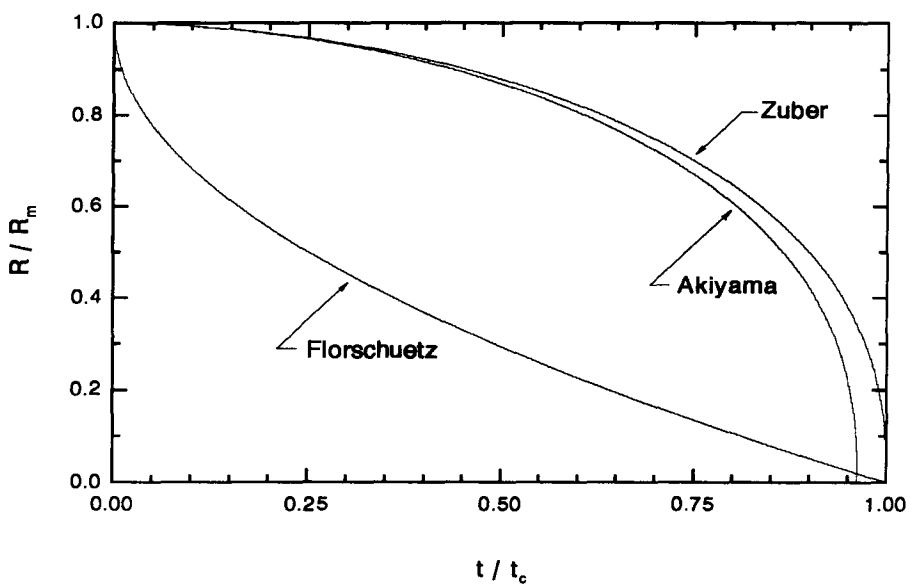

Figure 2.6. Comparison of bubble collapse models in uniformly subcooled liquid (Florschuetz and Chao[31], Akiyama[30], Zuber[23]).

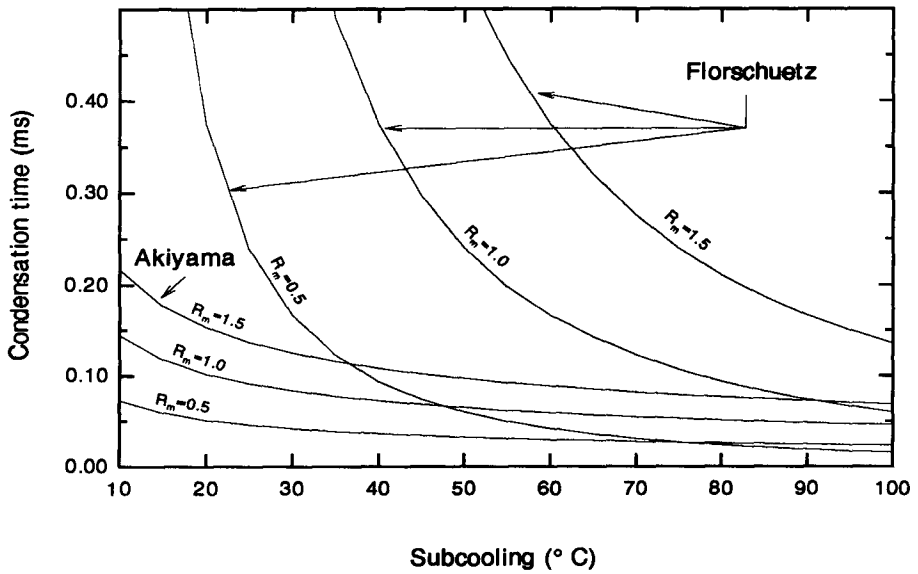

Figure 2.7. Comparison of condensation time predicated by Florschuetz and Chao[31] and Akiyama[30].

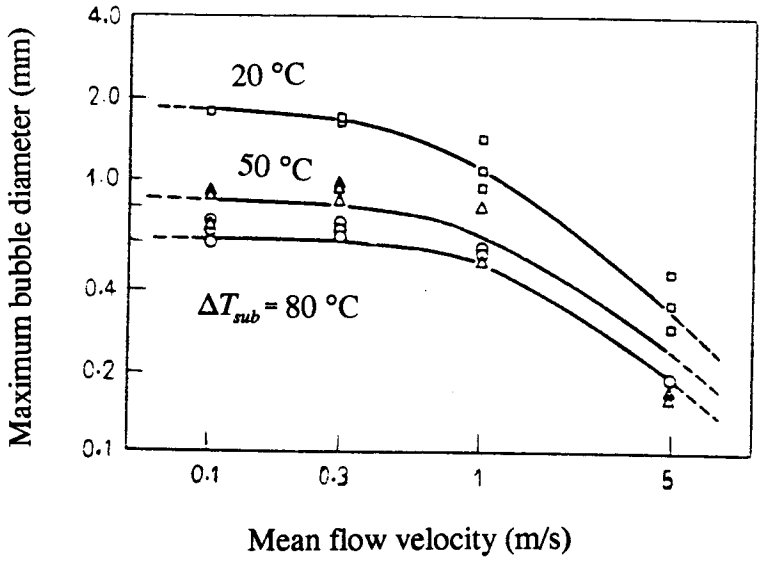

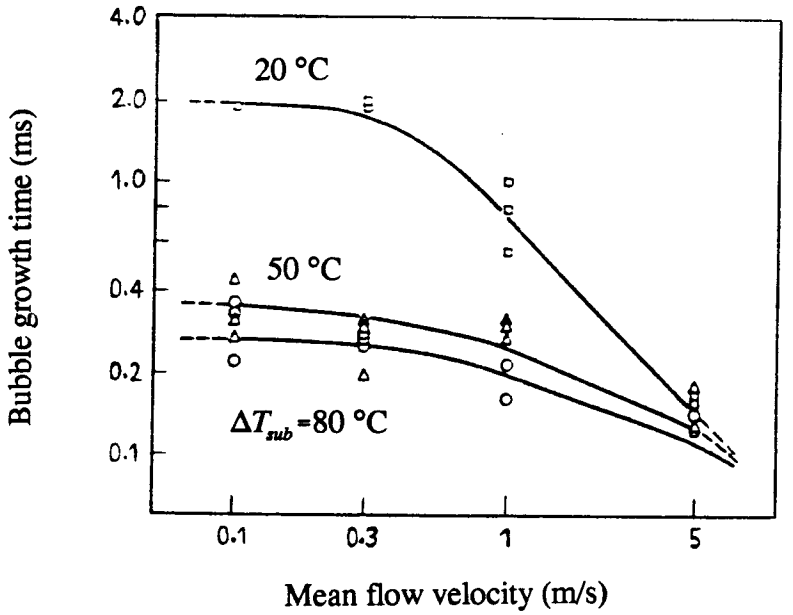

Figure 2.8. Effect of mean flow velocity on bubble maximum diameter and growth time (from Akiyama[38]).

CHAPTER 3

EXPERIMENTAL APPARATUS AND DATA PROCESSING

The flow visualization experiments were performed on the test facility designed at the University of British Columbia to simulate the thermohydraulic conditions of SLOWPOKE reactors and used previously for void fraction measurements by Bibeau[6]. This chapter describes the facility and the procedure followed prior to filming, discusses the choice of the experimental conditions under which the films were taken, and elaborates on the flow visualization setup and image processing system for bubble analysis.

3.1 Test Facility

Figure 3.1 is a schematic diagram of the test facility. The test section, where the boiling occurred, was located in series with a pump, a condenser, an immersion heater, and flow meters. A *3 H.P.* centrifugal pump was used to circulate distilled water through the loop and the flow through the test section was adjusted by a by-pass line located downstream of the pump. The temperature of the loop was controlled by a *4.5 kW* immersion heater. The flow entered at the bottom of the test section at a preset temperature and flow rate and exited to the condenser at the top of the test section where all the vapour was condensed. An additional heat exchanger mounted before the main pump facilitated the cooling of the flow for lower inlet temperature. The distilled water

was produced by the use of a distiller and collected for later use inside a clean, sealed 100-gallon polyethylene tank.

The test section consisted of a hollow stainless steel tube (type 316) , *2.1 mm* thick, with outside diameter of *12.7 mm* and *480 mm* long heating length. The stainless steel tube was located concentrically inside a bigger glass tube of inside diameter of *21.8 mm* forming an annular flow area (Figure 3.2). Both ends of the stainless steel tube (heater) were welded to hollow copper tubes of the same outside diameter (heater assembly). The heater assembly was vertically mounted on a four-legged support where it was connected to the rest of the loop via copper piping. The test section was heated by large amounts of current (up to *2000 amperes*) passed through the stainless tube with the use of a *64 kVA a.c.* adjustable power supply. The current was carried from the power supply to the test section by copper bars attached to copper tubes at the ends of the heater at the top and the bottom of the support frame.

3.2 Instrumentation

The average inlet temperature was measured at the bottom plenum while the average outlet temperature was measured at one meter downstream of the outlet plenum to avoid vapour patches. The thermocouples used were ungrounded, shielded, K-type thermocouples.

The heater wall temperature was measured at the location of filming (*440 mm* from the upstream end of the stainless steel heater) with an ungrounded K-type thermocouple spot welded to the heater surface. The thermocouple wires were *0.102 mm* in diameter, in a *0.508 mm* diameter stainless steel sheath. The heater assembly and thermocouple attachments were fabricated and designed by Atomic Energy Canada Limited.

Two turbine flow meters each with a different sensitivity *(0.006-0.6 kg/s)* measured the mean flow rate in the test section. The frequency output of the flow meters were converted to d.c. voltage using a frequency-to-voltage converter. The current was measured with an induction coil which generated an a.c. signal proportional to the current. The a.c. voltage across the heater element was conditioned to a 0 to 10 volts d.c. voltage signal.

The conditioned output d.c. signals from the instruments were all fed to an analog to digital converter board in an IBM 486 PC computer. The data were collected by scanning the various channels in the analog to digital converter by the use of a data acquisition program written in C-language. More detailed information on the test facility is in reference [6].

3.3 High-Speed Photography Setup

A 16-mm Hycam high-speed camera was used to perform the flow visualization due to high bubble growth and collapse rates. Snap-shots of the boiling process with a shutter speed of *1/4000 sec* provided less expensive means of optimizing the lighting conditions and magnification (Figure 3.3). These snap-shots revealed the approximate sizes of the bubbles and aided determination of the approximate orientation and the number of lights to be used for optimum illumination. The setup shown in Figure 3.4 provided the best lighting and magnification. The camera was operated at *4000 - 6000* frames per second. The images of bubbles were recorded on *100 ft* long *16 mm* Kodak reversal films with ASA rating of *400*. The duration of filming corresponded to *800 ms* of the boiling process (*4500* frames in one roll). A neon lamp inside the camera was activated by a pulse generator of *1000 Hz* to produce timing marks on the films at an interval of *1 ms*. The test section was back lit with the use of two racks of lights each consisting of six *300-watt*

tungsten halogen projector lamps located *25 cm* from the test section. A light diffuser screen positioned half way between the test section and the lighting source provided a uniform illumination of the area of interest. High magnification was achieved on the film with the use of a macro-telephoto Tamron SP lens (set at *80 mm* focal length) attached to a *40 mm* extension tube. When the distance from the base of the lens to the glass tube was set to approximately *20 cm*, the magnification on the film corresponded to the actual dimension of the bubble. The field of view with this magnification covered *8 mm* of the length of the heater with a width from the glass tube up to the surface of the heater element(dotted rectangle in Figure 3.4).

Due to the requirement of high magnification and frame speeds, many trial and error tests were run to achieve the best possible lighting and magnification. Although higher magnification could be achieved on the film, the depth of view and the field of view would be lessened. With the reduction of the depth of field, the bubble image would be lost if the bubble traveled towards or away from the camera. A smaller field of view would result in the loss of bubble image if the bubble traveled great distances before condensing completely. A maximum of *10,000 fps* was attainable with the Hycam though that would demand more illumination and also less time of the boiling activity would be captured on the film. Therefore, for best magnification, illumination and frame speed, aside from the snap-shots mentioned, about *10* trial and error runs were conducted with the Hycam. The arrangements and specifications discussed and shown in Figure 3.4 were the results of these lengthy trial and error tests.

3.4 Procedure for Degassing

Eexperiments were started by first degassing the system to get rid of the dissolved air in the loop. The flow was directed inside the test section (the by-pass line was almost

closed) and the pressure in the loop was raised to three atmospheres to avoid surface boiling on the heater surface. The heater was turned on and set at maximum power (approx. *24 kW*) to raise the temperature of the water. When the temperature in the loop had reached approximately *105 °C* (*45* minutes, *2 °C/min*), the heater was shut off and the pressure was dropped to atmospheric pressure. The system was degassed by opening the vent valves located at the top of immersion heater and condenser and also at various elevated points in the loop where the chance of trapped air was high. Degassing was repeated two or three times at the beginning of every experiment to ensure that all the air was removed from the system before the filming. Before the condition was set for an experiment, surface boiling at the heater surface was initiated (for about *15* minutes) by raising the power in the heater at relatively small flow rates so that air adhered to the heater surface would detach. When the system had been thoroughly degassed (three hours later), the experimental conditions for filming were set. These variables included the flow rate ($\dot{m}$), heat flux(ϕ), and the subcooling (ΔT_{sub}).

3.5 Experimental Conditions

As has been noted, the purpose of these flow visualization experiments was to visualize the bubbles produced under the same conditions as those of the void growth experiments performed by Bibeau[6]. In these experiments, the flow rate and inlet temperature were kept constant while the heat flux was varied from ONB to approximately *35%* void fraction. This procedure implied that, at the location of void measurement, both the heat flux and subcooling changed. In this study, the flow visualization were performed at constant bulk liquid subcooling and flow rate by varying the heat flux (Table 3.1). The loop was set at atmospheric pressure and the flow rate was set only at three different values of *0.02*, *0.10* and *0.20 kg/s* (corresponding to *0.08*, *0.4*,

0.8 m/s receptively). The inlet temperatures corresponded to the bulk liquid subcoolings of *10, 20, 30, 40, 60 °C* at the location of filming. The inlet temperature was related to the bulk liquid subcooling by the heat balance equation from the upstream end of the heater to the location of filming (l):

$$\Delta T_{sub} = T_{sat} - T_{in} - \frac{\phi P l}{\dot{m} C_{pl}} \tag{3.1}$$

where $l = 440\ mm$, $P = 39.89\ mm$ and $T_{sat} = 102.1\,°C$. The range of heat flux extended from values corresponding to the onset of nucleate boiling (ONB) to the vicinity of onset of significant void (OSV). Heat fluxes corresponding to ONB were obtained from the correlation of Hahne et al[45] as:

$$\phi_{onb} = h_{con}\left\{\frac{2\sigma_l T_{sat}(1/\rho_v - 1/\rho_l)}{R_{cav} i_{fg}} + \Delta T_{sub}\right\} \tag{3.2}$$

where $R_{cav} = 4.5 \times 10^{-6} m$ given by [9] and h_c was calculated by Dittus-Boelter correlation [46]:

$$Nu = 0.023\,\mathrm{Re}^{0.8}\,\mathrm{Pr}^{0.33} \tag{3.3}$$

The heat fluxes for OSV were obtained from Bibeau[9] as:

$$St_{osv} = a_1 Pe^{a_2} \tag{3.4}$$

where the coefficients $a_1 = 136$ and $a_2 = -0.88$ were given by [9] obtained from the void fraction experiments for the present experimental conditions. Figure 3.5 illustrates the relative position of each experiment with respect to ONB and OSV heat fluxes evaluated from (3.2) and (3.4). A total of 45 different conditions were filmed with each condition denoted by a dot in Figure 3.5. Experiments were performed at constant subcooling and

mass flow rates by varying the heat flux from ONB to OSV. The choice of flow conditions were limited by two constraints of the test facility: both the inlet temperatures of less than *15 °C* and heat fluxes larger than *1.2* MW/m^2 were unattainable. Due to the first limitation, the point of OSV was not achieved for subcoolings larger than *10 °C* at low flow rate. Due to the second limitation, the point of OSV was not attainable at subcoolings of *40* and *60 °C* at high flow rate.

3.6 Data Processing

3.6.1 Digitizing Setup

The films were analyzed by a digital image processing system shown in Fig 3.6. The system consisted of a video adapter (PhotovixII) with a Tamron CCD solid state camera focused on a high intensity light source. The film was placed on top of the light source and the image was captured by the camera. Passing the *16 mm* film, frame by frame, through PhotovixII converted each frame to a video signal. The video signal was fed to a PCVision-Plus frame grabber which resided in a host PC 486 computer. The frame grabber digitized the video signal into *640* by *480* pixel digital image with *256* levels of gray scales. With this setup, great magnifications (of up to *30* times the actual bubble size) on the monitor were obtained (see Figure 3.7). For analysis of the digitized images of bubbles and evaluation of the bubble parameters, a computer program in C-language was developed and interfaced with the frame grabber.

3.6.2 Evaluation of Bubble Volume

Most researchers used the average of the major and minor axes of the assumed spheroid to evaluate an average diameter for the bubble. However, this study first evaluates the volume and second, deduces an equivalent spherical radius by the use of:

$$R = \left(\frac{3Vol}{4\pi}\right)^{1/3} \tag{3.5}$$

Observations of images of the bubbles showed that the bubbles possessed at least one axis of symmetry during most of their lifetime. The bubble volume was evaluated by finding the volume of revolution of the areas on each side of the axis of symmetry of the bubble. Depending on the flow conditions, the growth and collapse process of a typical bubble was recorded on *10* to *60* frames. The volume-versus-time graph for bubbles was obtained by evaluating bubble volume at successive frames from its birth to its total collapse. From the volume-versus-time graph, the maximum bubble volume (Vol_{max}), bubble growth time (t_m), condensation time (t_c) and lifetime (t_b) were deduced (see Figure 3.8).

Figure 3.9 is a schematic diagram of the procedure used to evaluate the bubble volume with the pixel integration technique. The outline of the bubble was discretized with line segments of *10* to *40* pieces, depending on the bubble size (Figure 3.10a). The pixels comprising the image of the bubble were scanned (Figure 3.10b) and the area of the projection of the bubble and its centroid were calculated (Figure 3.10c). The orientation of the symmetry axis was found by observing that the axis of symmetry coincides with one of the principal centroidal axis of the area for a symmetric body[47]. The principal centroidal axis were drawn on the bubble (Figures 3.10d) and the symmetry axis was selected from the two choices of the axes. The areas and centroids on each side of the symmetry axis were evaluated (Figure 3.10e) and the volume of the revolution of each area around the axis of symmetry was calculated. The bubble volume was defined by the average of the

two volumes of revolution. In addition to the bubble volume, the displacement of the centroid parallel and normal to the heater wall (L_n, L_p) and change in bubble shape (D_n, D_p) with time were sought (Figure 3.11). For more information on the computer program and pixel integration refer to Appendix C.

The inputs to the program were the coordinates of the boundary of the bubble, the reference point, the location of the nucleation site, the scale and the time marks. The coordinates of the pixels at the edges of the bubble were obtained by selecting points at the bubble outline with the use of a mouse. Although different edge-enhancement image processing softwares were tested to avoid this tedious task, no outcome was satisfactory. The reference point was the center of the cross-hair marking built in the camera lens which appeared on every frame. The location of the nucleation site corresponded to the mid-point of the bubble on the wall in the first frame where the bubble was visible. A scale in *mm* was placed on the side of the glass tube and was visible on every frame. The scale and the nucleation site location were entered by the use of a mouse, once at the beginning of the digitization process; however, the reference point had to be entered for every frame. The output of the program was the volume(Vol), equivalent spherical radius(R), displacement of bubble centroid from the nucleation site(L_n, L_p) and the diameters along the principal axis of inertia of the bubble(D_n, D_p) as shown in Figure 3.12.

3.6.3 Procedure for selecting an 'average bubble'

The statistical nature of the process of growth and collapse of vapour bubbles in subcooled water has been reported by many researchers[35-38]. Therefore, for a set condition, variations in bubble parameters from one nucleation site to another are expected. Moreover, given a specific nucleation site, the bubble parameters also exhibit statistical variations with time. Since the employment of rigorous statistical methods for

measuring and evaluating the bubble parameters would have been extremely difficult and time-consuming, different researchers have used varied approaches in evaluating the bubble parameters and in avoiding statistical analysis. For instance, Gunther estimated bubble lifetime and maximum radius by 'digitizing' four to eight bubbles for one condition and taking the average value of radius and lifetime from these observations. Akiyama[30] digitized the largest and smallest, and a few in-between, bubbles and used an average value based on these bubbles.

This study takes a different approach in the selection of an average bubble. First, a nucleation site which was active in most of the films was located and all the bubbles emerging from that nucleation site were marked. Therefore, all the bubbles analyzed were initiated from one specific nucleation site eliminating the spatial variation of bubble parameters from site to site. For the random variation of bubble parameters from one nucleation site, the following procedure was implemented. The lifetime of all marked bubbles was found for every film, and an average bubble lifetime was defined. Then, three to five bubbles with closest lifetime to the average bubble lifetime for the condition were digitized. From the digitized bubbles, one with maximum radius closest to the average maximum radius of the digitized bubbles was chosen to represent the bubble behavior for that condition. This method of selection of an average bubble is justified since the distribution of the bubble lifetime from a nucleation site was found to be approximately normal (Figure 3.13). Moreover, Del valle and Kenning[37] reported that the distribution of the maximum radius is also normal. Depending on the flow conditions about *15* to *45* bubbles were available for analysis in one film.

Figure 3.14 shows the volume versus time graph for the three bubbles digitized for the following conditions (D24): $V = 0.4\ (m/s)$, $\Delta T_{sub} = 20(°C)$ and $\phi = 0.3(MW/m^2)$. For this condition, the average bubble lifetime based on *15* bubbles observed in the entire roll of

the film was *8.35 ms* . Since bubble # D24-10 had a maximum radius closer to the average maximum radius, this bubble is selected to represent the typical behavior of bubbles in that condition.

3.7 Error Analysis

Tables 3.2 and 3.3 list the experimental errors for the measured and calculated parameters. The errors in the measured quantities $(T_w, T_{in}, \dot{m})$ were either estimated from the manufacturers' specifications or reference[9]. The estimation of uncertainties in the calculated parameters $(\phi, \Delta T_{sub})$ is given in Appendix D. The estimated errors for measured quantities from image processing $(Vol, R, D_n, D_p, L_n, L_p)$ are obtained by measurement of the volume, centroid, and maximum and minimum diameters of a known shape and are further discussed in Appendix D.

Table 3.1. Range of experimental parameters.

Experimental promoters	Range of parameters
Pressure, P (atm)	1
Mass flow rate, $\dot{m}$ $(^{kg}/_{s})$	0.02, 0.10, 0.20
Mean flow velocity, V $(^{m}/_{s})$	0.08, 0.4, 0.8
Subcooling, $\Delta T_{sub}(^{\circ}C)$	10, 20, 30, 40, 60
Heat flux, ϕ $(^{MW}/_{m^2})$	0.1 - 1.2

Table 3.2. Estimated error for measured and calculated experimental parameters.

Measured or Calculated quantity	Error
Inlet temperature, T_{in}	$\pm 1\,^{\circ}C$
Wall temperature, T_w	$-2.2 / +1.2\,^{\circ}C$
Subcooling, ΔT_{sub}	$\pm 2\,^{\circ}C$
Heat flux, ϕ	± 2 %
Mass flow rate, $\dot{m}$	± 0.3 %

Table 3.3. Estimated error for measured quantities obtained from high-speed photography.

Measured or Calculated quantity	Error
Volume, Vol	± 5 %
Radius, R	± 1.7 %
Parallel / Normal displacement, L_n, L_p	± 0.08 mm
Parallel / Normal diameters, D_n, D_p	± 5 %
Time, t	± 0.02 ms

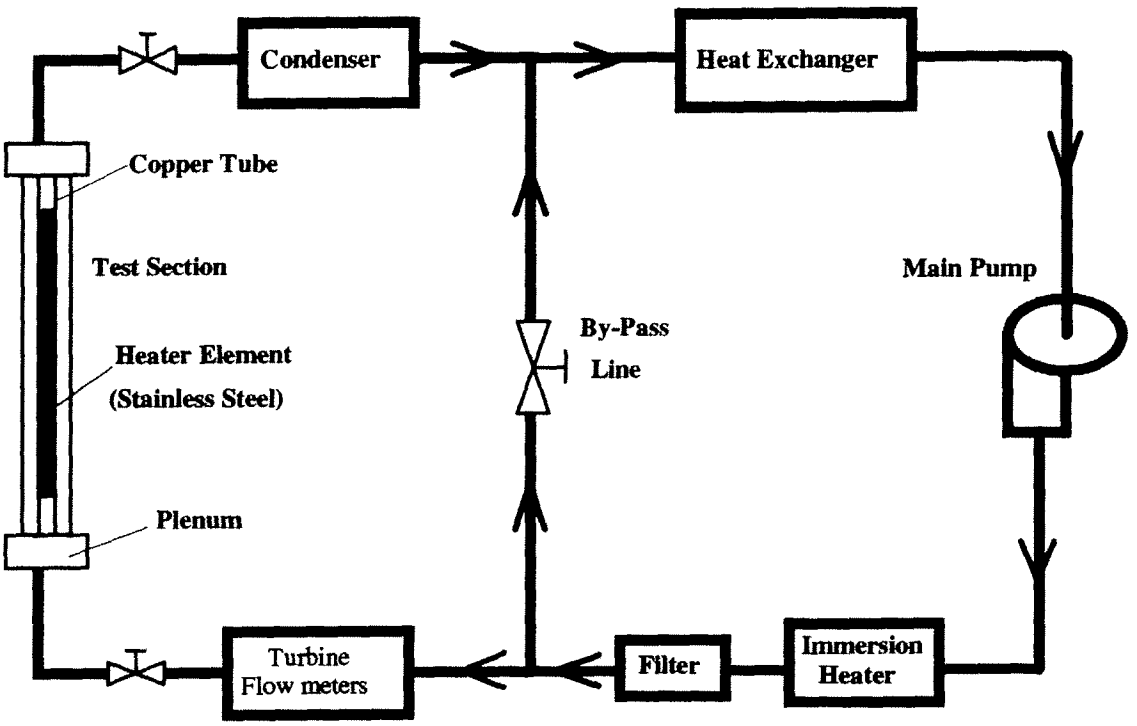

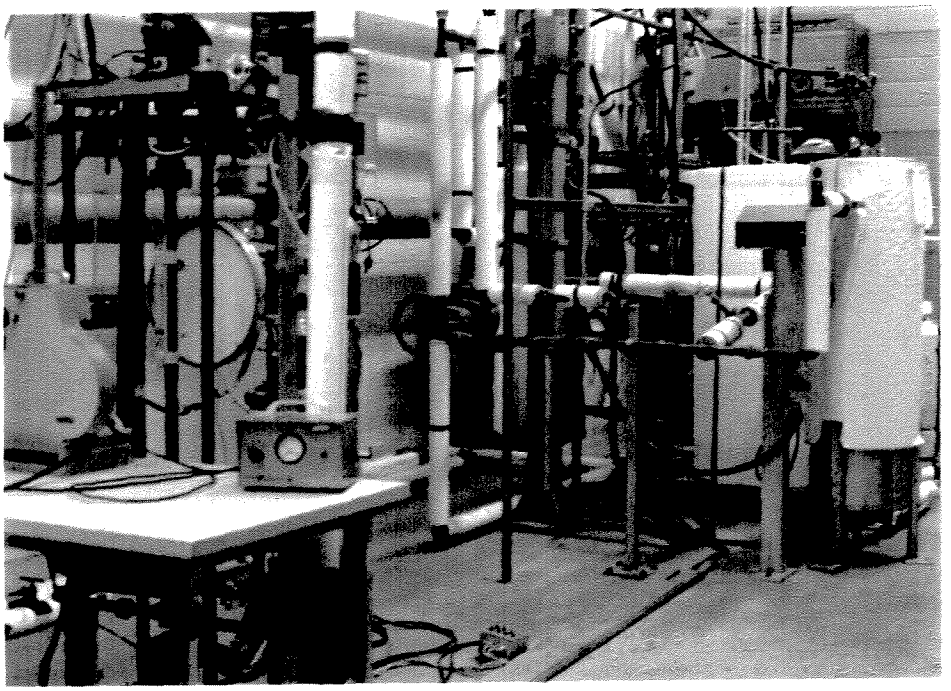

Figure 3.1. Schematic diagram and photograph of test facility.

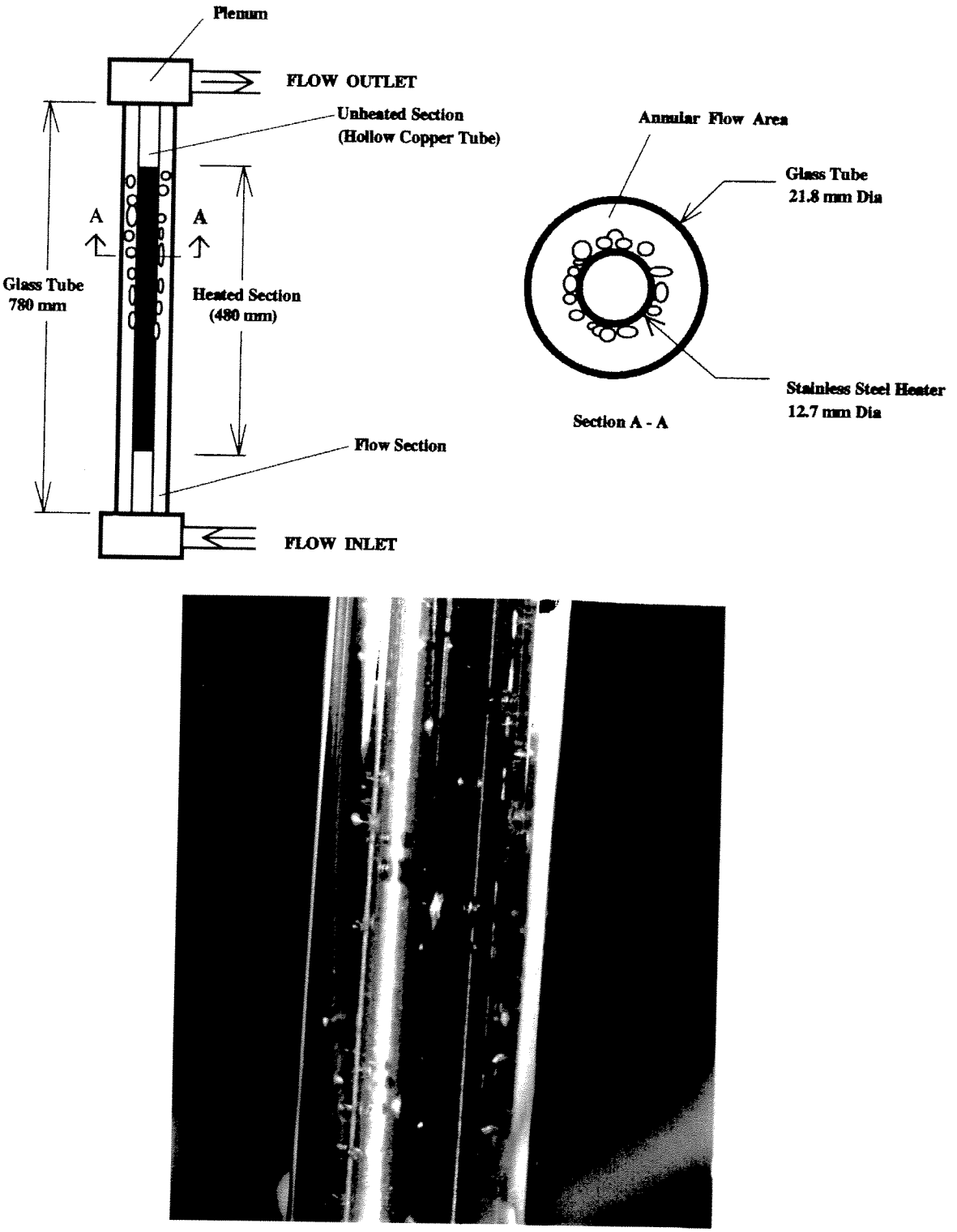

Figure 3.2. Schematic diagram and photograph of the test section.

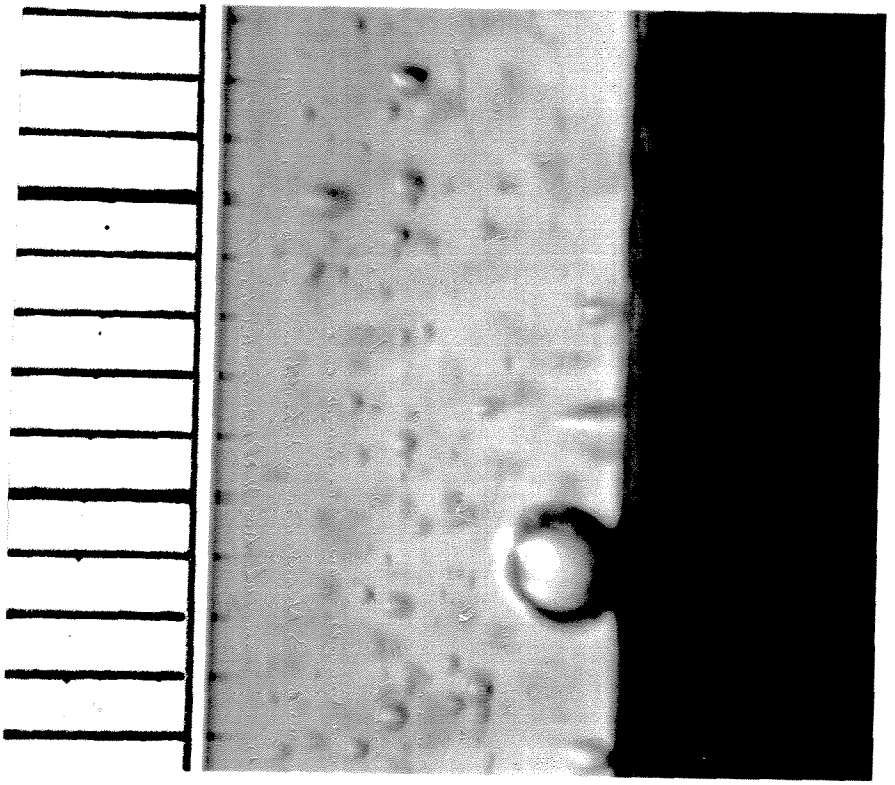

Figure 3.3. Snapshots of bubbles with a shutter speed of 1/4000 sec.

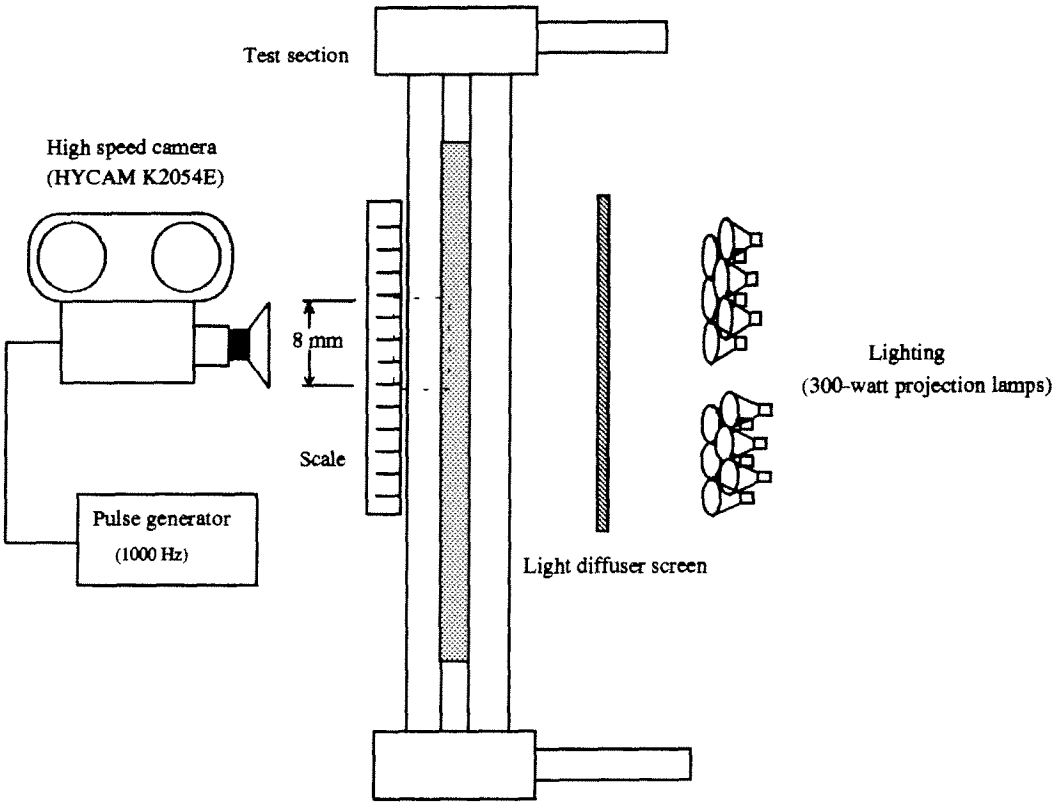

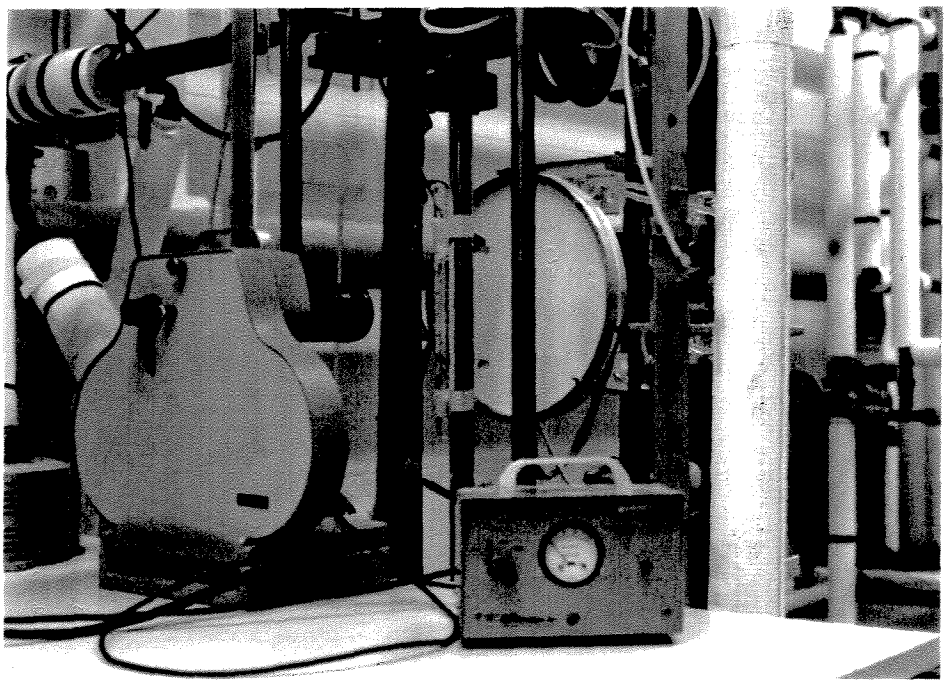

Figure 3.4. Schematic diagram and photograph of high speed filming setup.

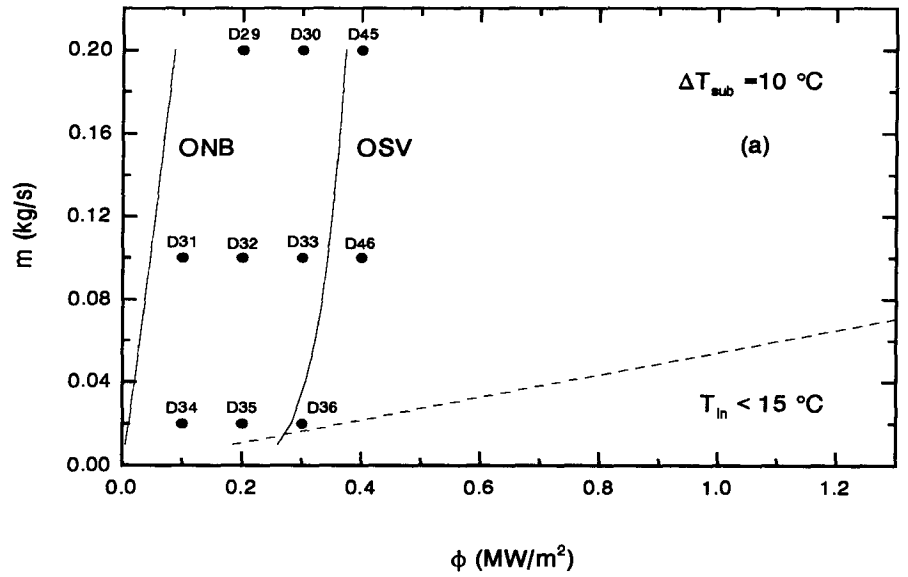

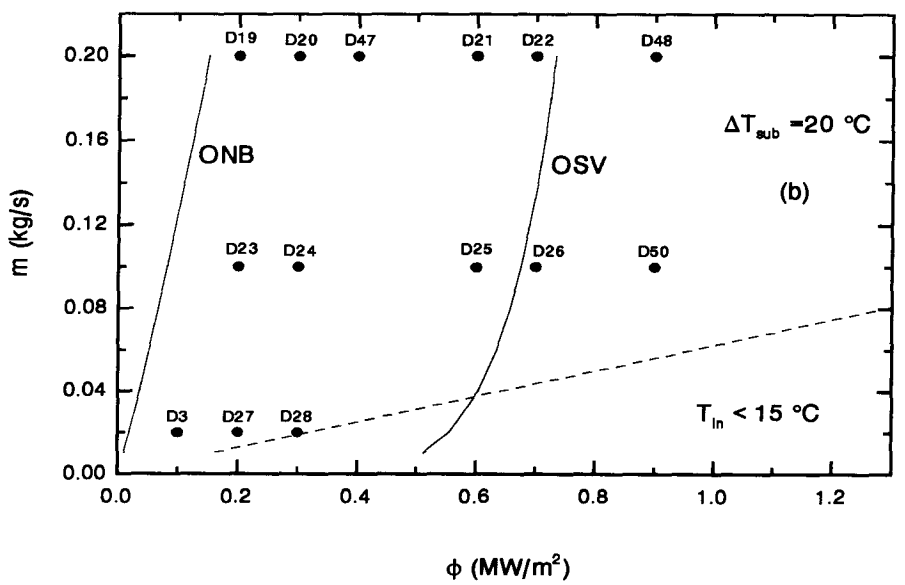

Figure 3.5. Filmed conditions for subcoolings of (a) 10 C (b) 20 C.

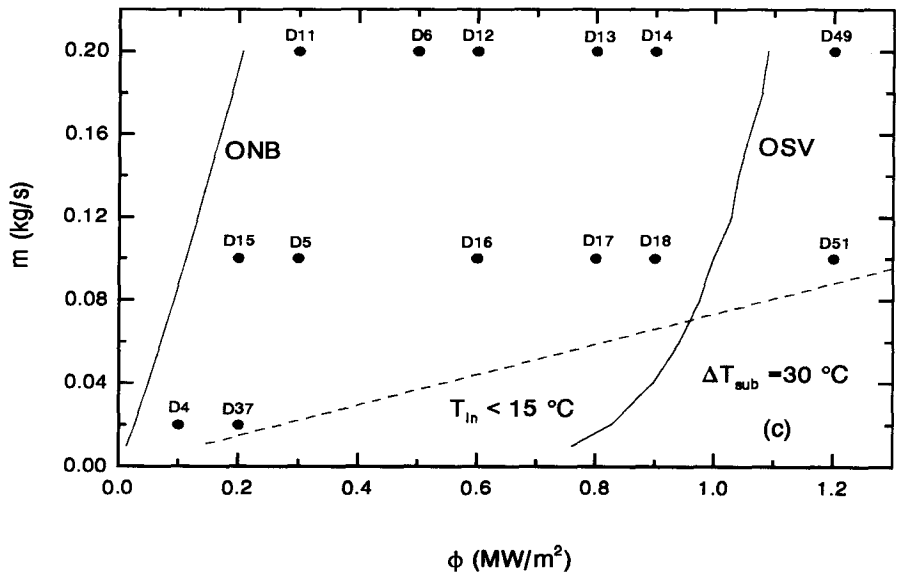

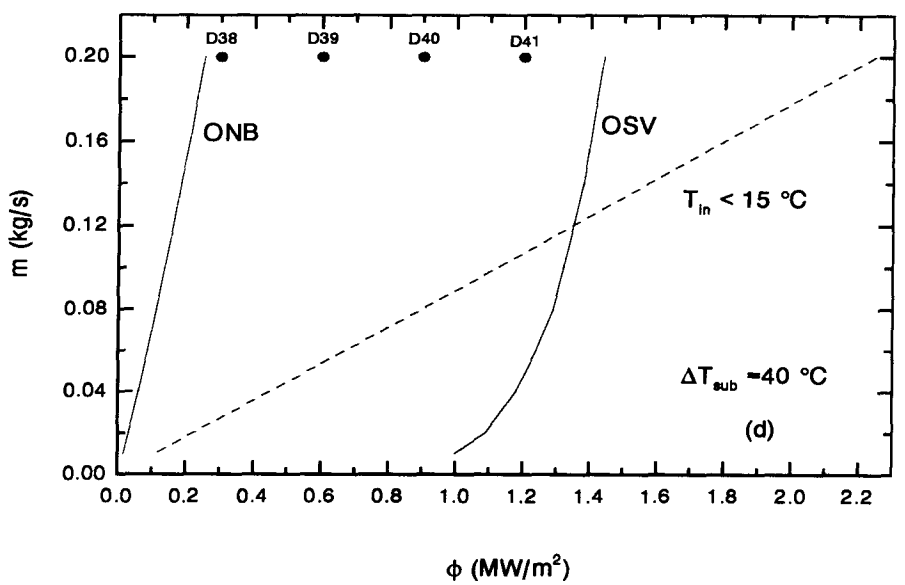

Figure 3.5 Filmed conditions for subcoolings of (c) 30 C (d) 40 C.

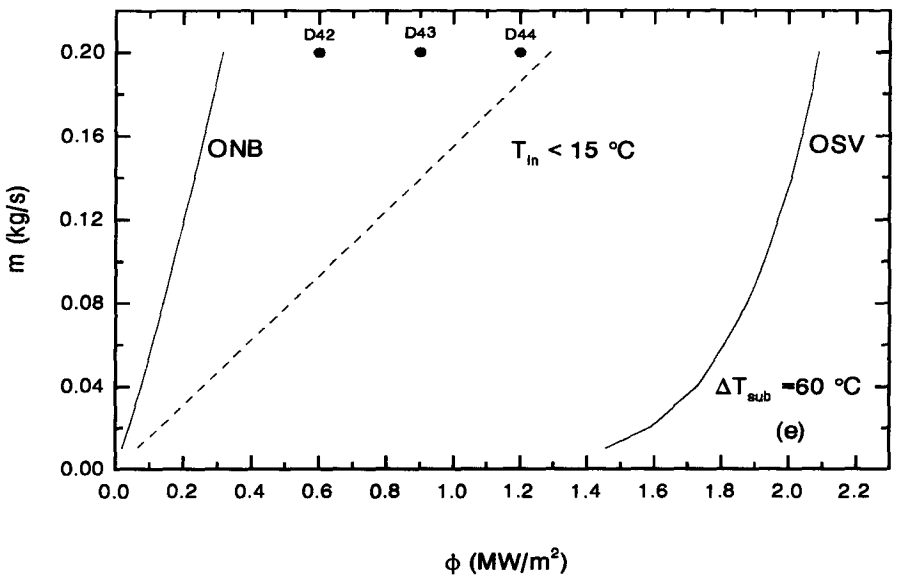

Figure 3.5. Filmed conditions for subcoolings of (e) 60 C.

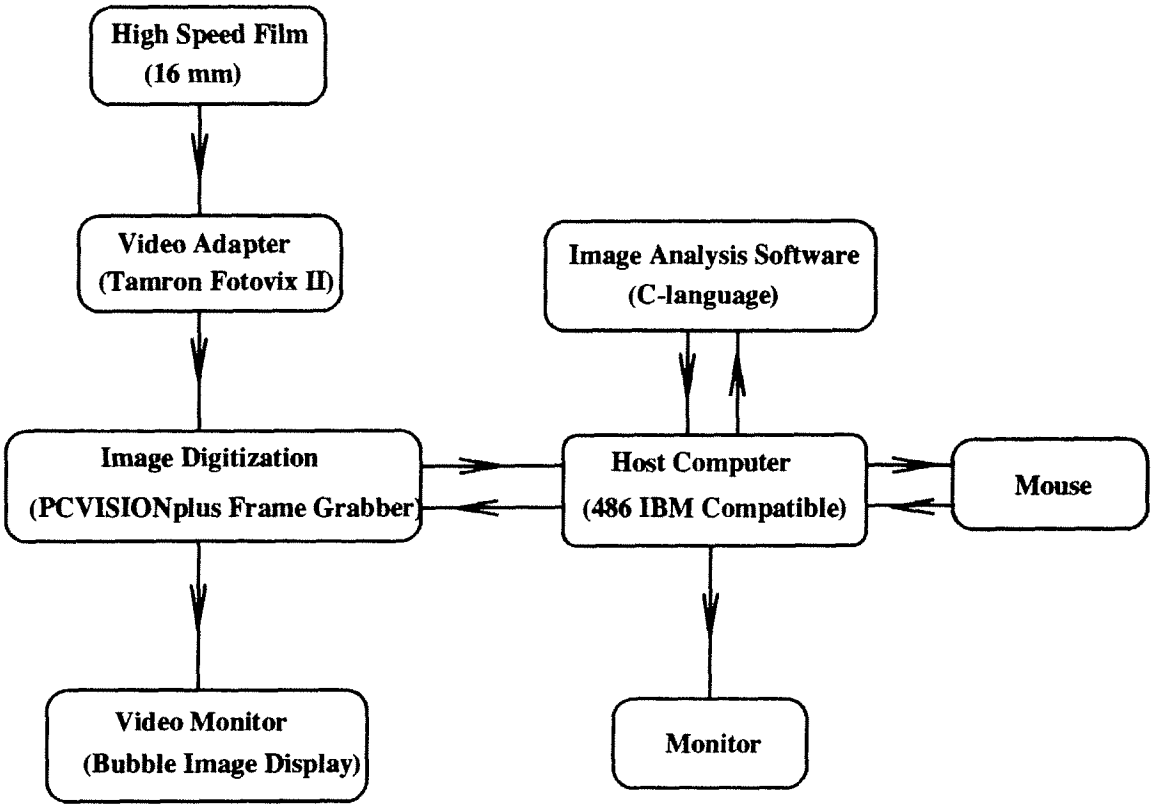

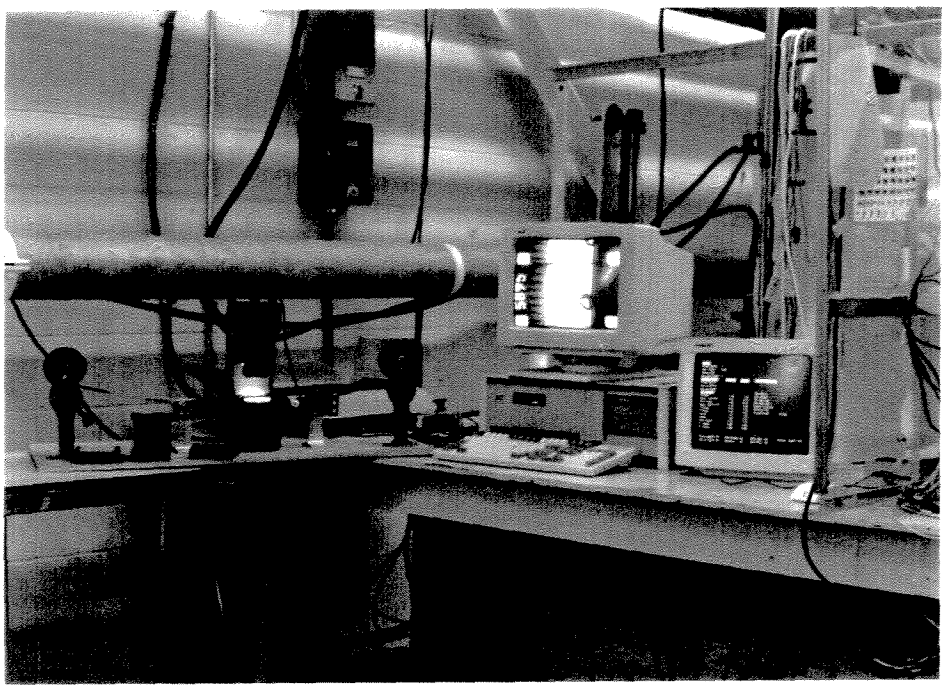

Figure 3.6. Schematic and photograph of image processing system.

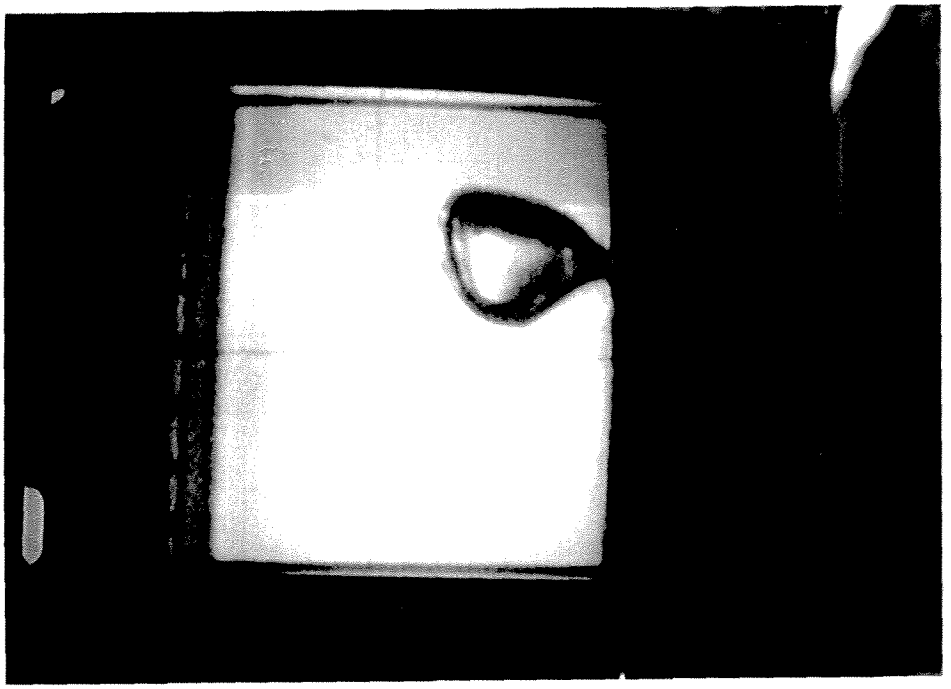

Figure 3.7. Magnified image of a bubble on the monitor.

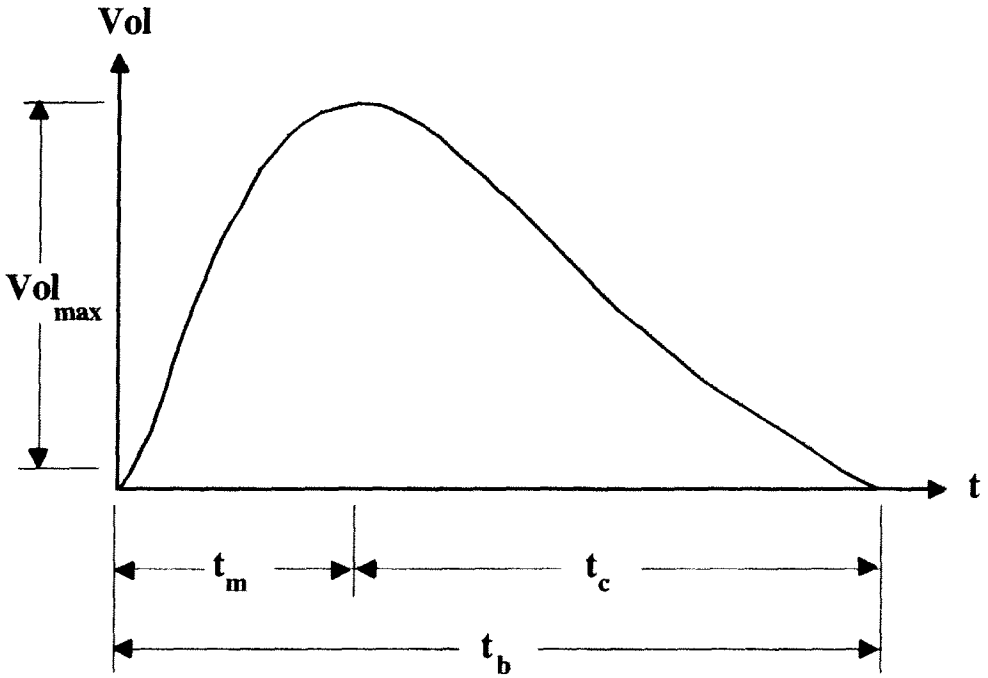

Figure 3.8. Definitions of bubble parameters.

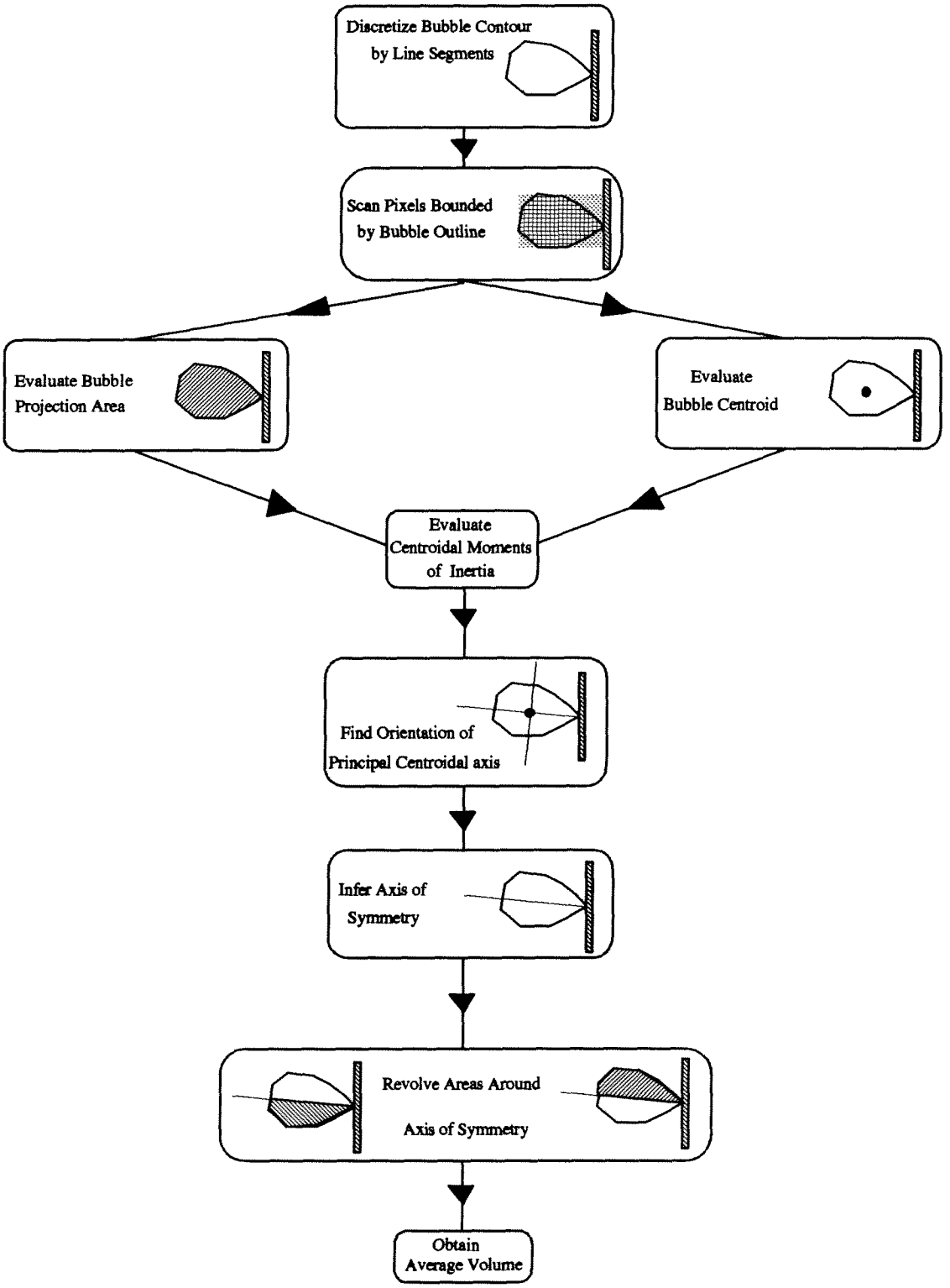

Figure 3.9. Steps in the evaluation of bubble volume.

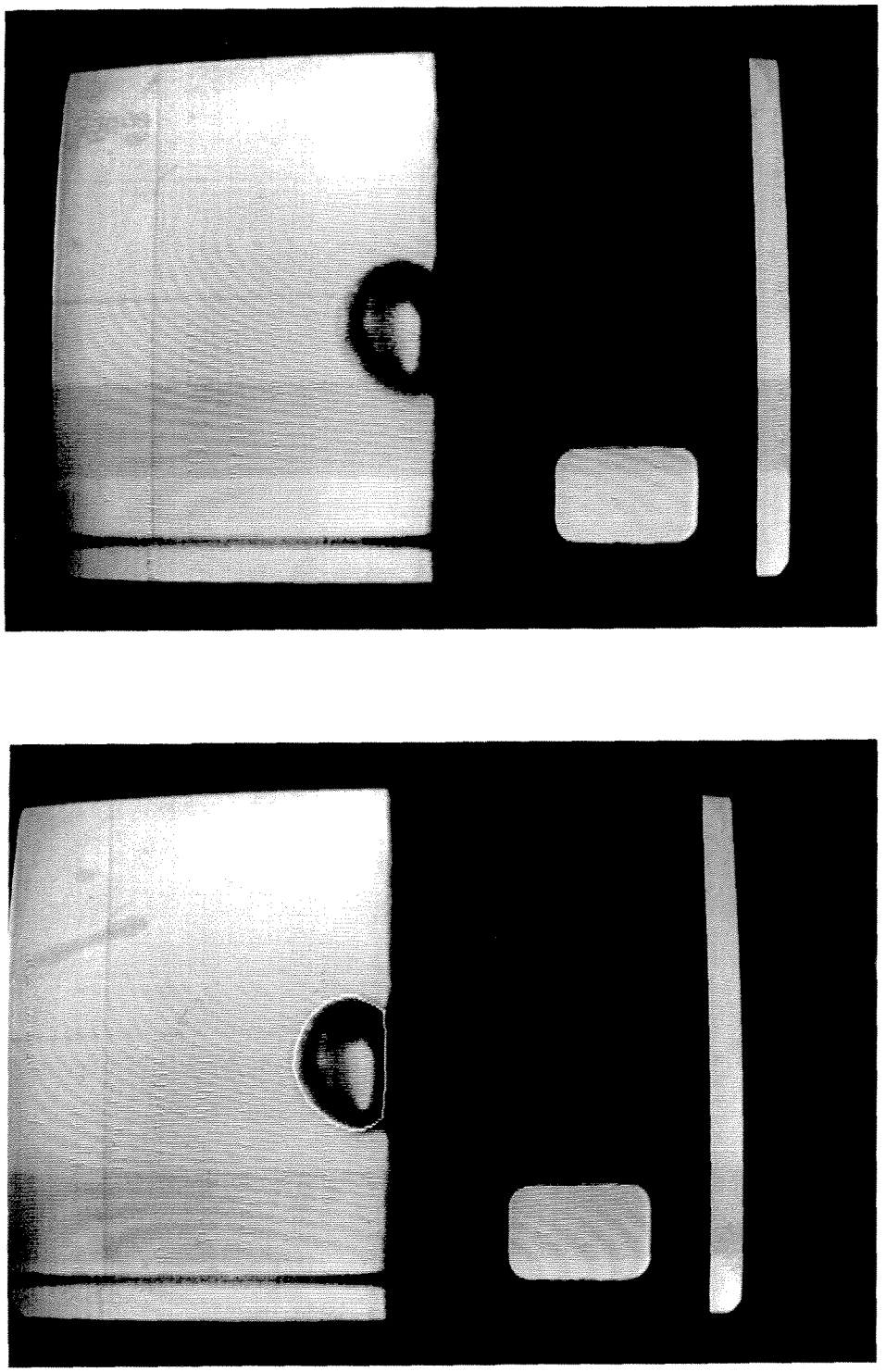

Figure 3.10. Photographs of the digitizing steps for evaluating bubble volume (a) Discritizing bubble outline.

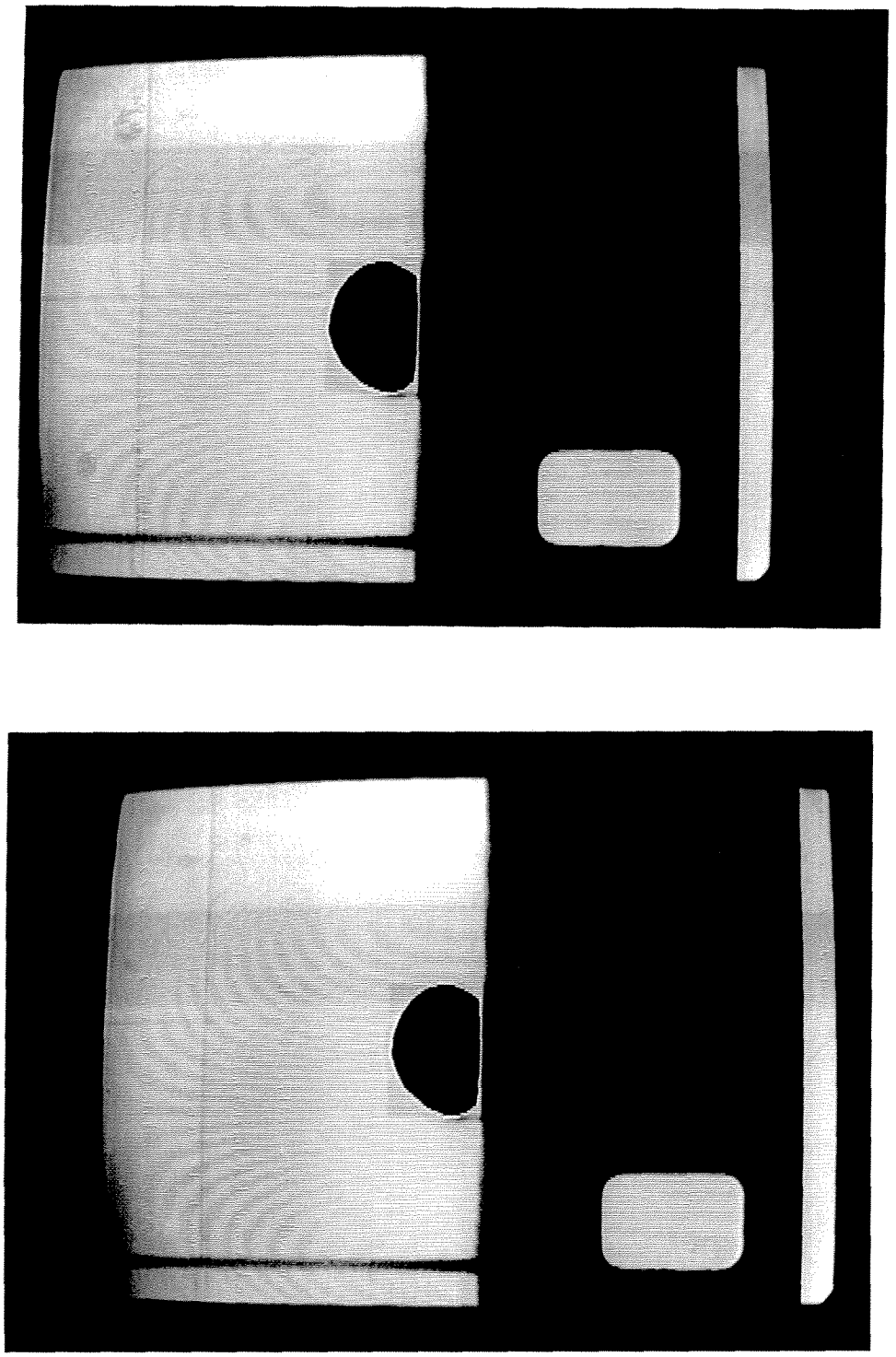

Figure 3.10. Photographs of digitization steps for evaluating bubble volume (b) Scaning bubble outline (c) determination of bubble projection area and centroid.

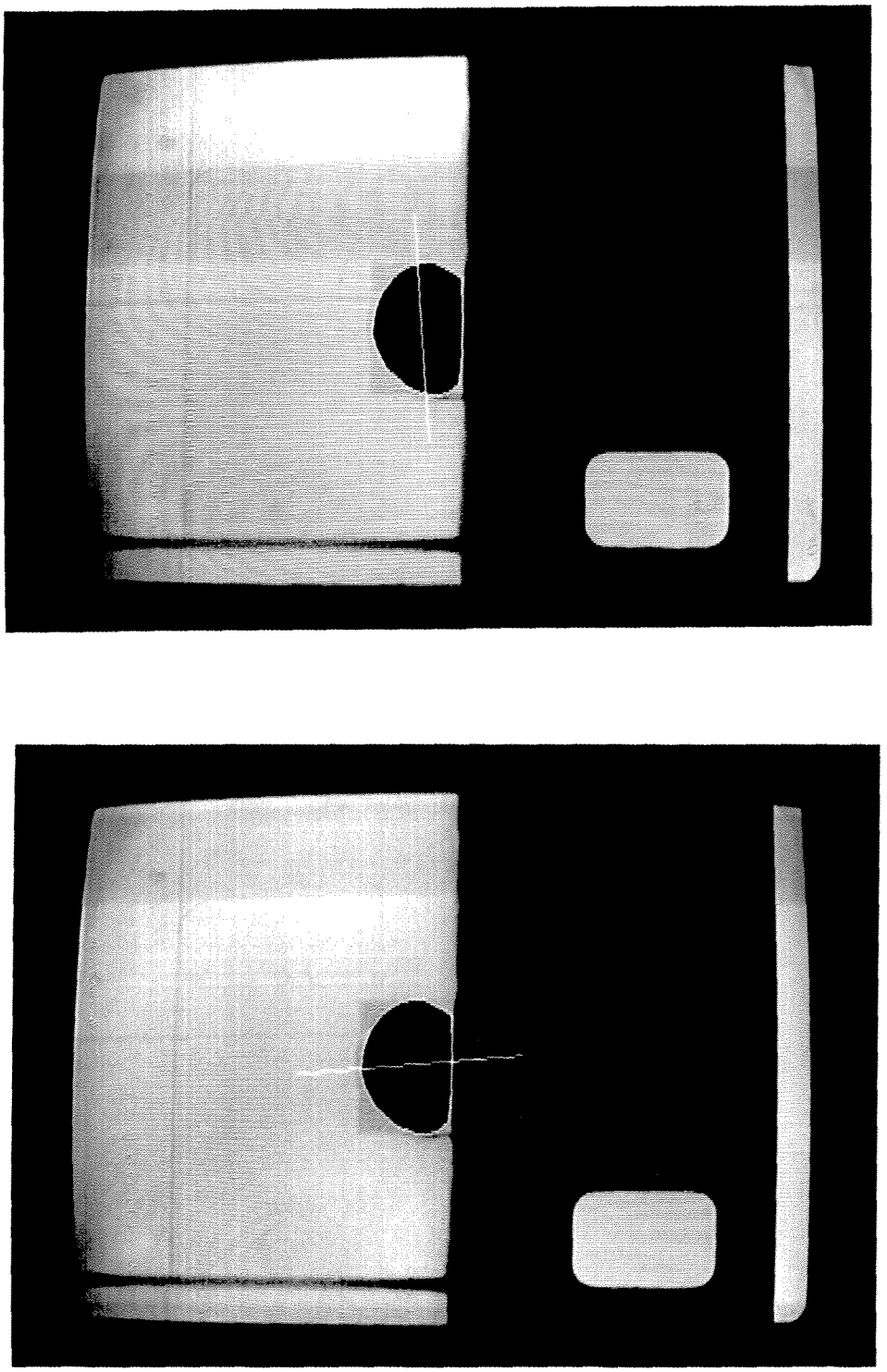

Figure 3.10. Photographs of digitization steps for evaluating bubble volume (d) evalution of centroidal principal axis of bubble projection area.

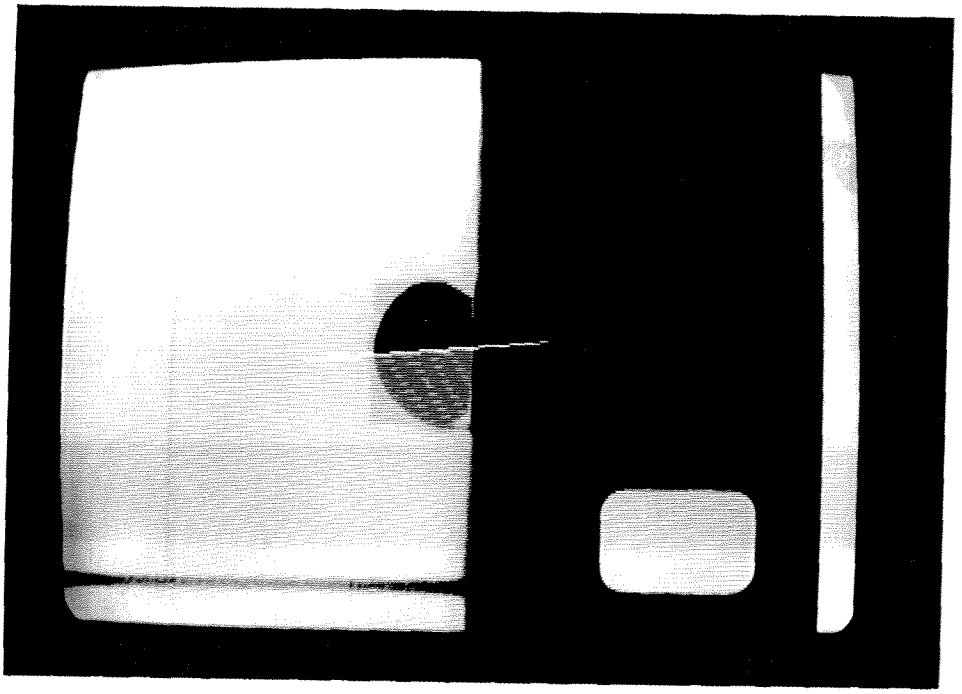

Figure 3.10. Photographs of digitization steps for evaluating bubble volume (e) evaluation of the volume of revolution of the areas on each side of the axis of symmetry.

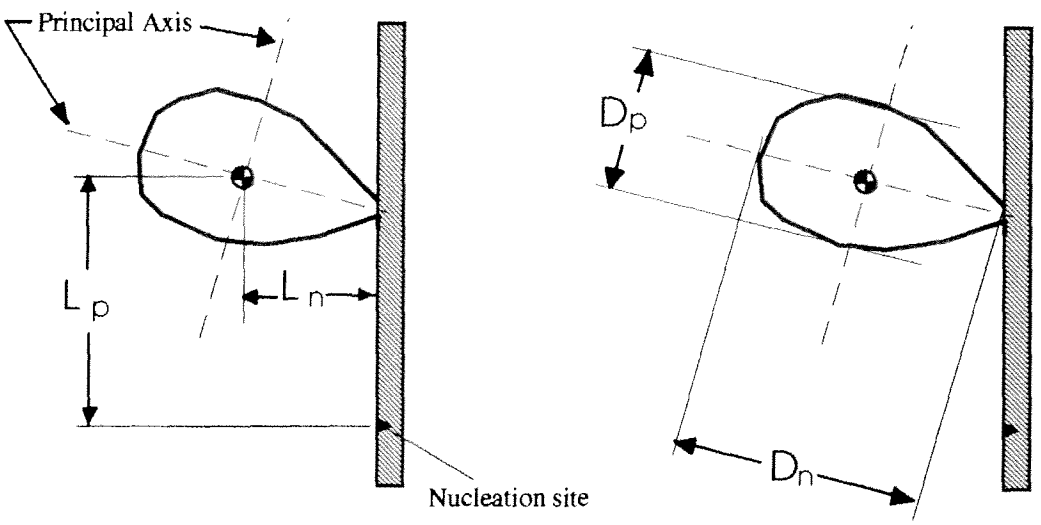

(a) (b)

Figure 3.11. (a) displacement of bubble centroid parallel and normal to heated surface with respect to the nucleation site (b) diameters along the centroidal principal axes.

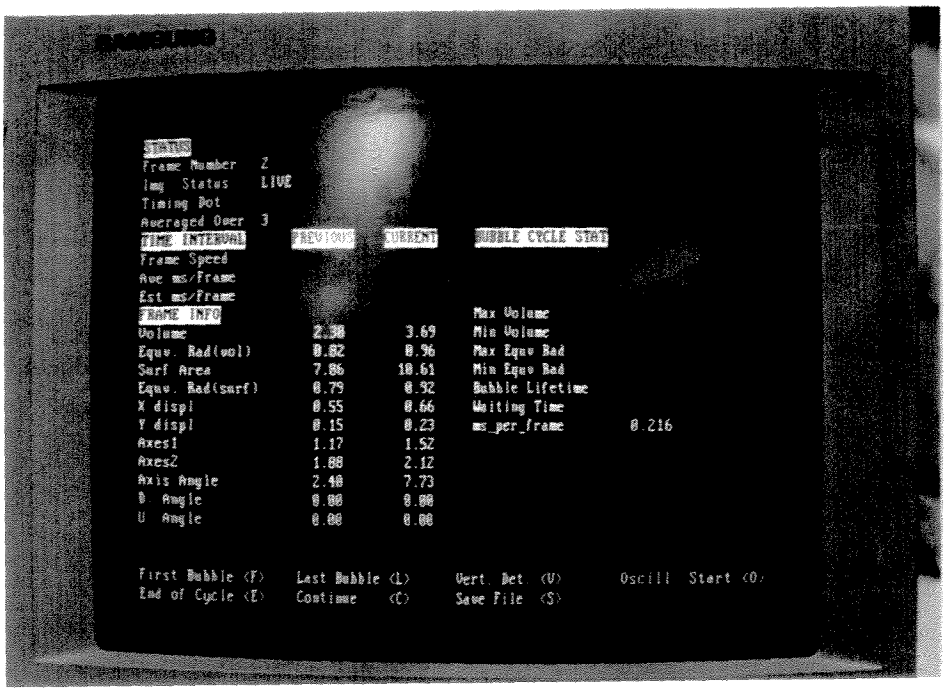

Figure 3.12. Photograph of frame analysis results displayed on the computer monitor.

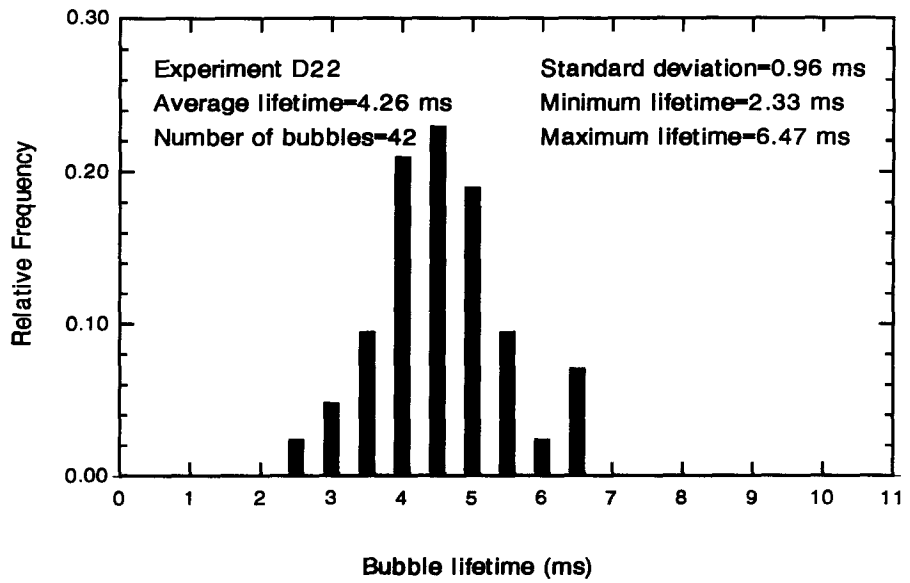

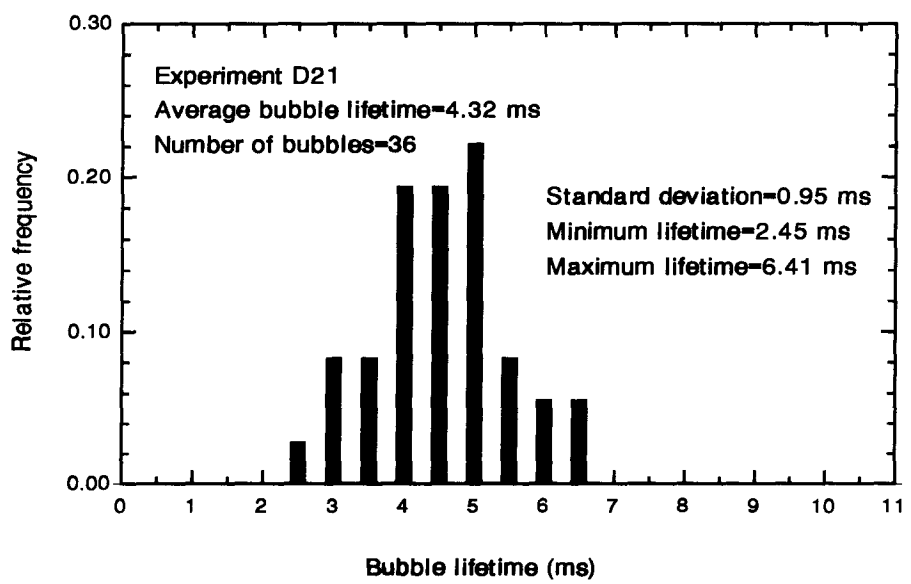

Figure 3.13. Distribution of bubble lifetime for conditions D21 and D22

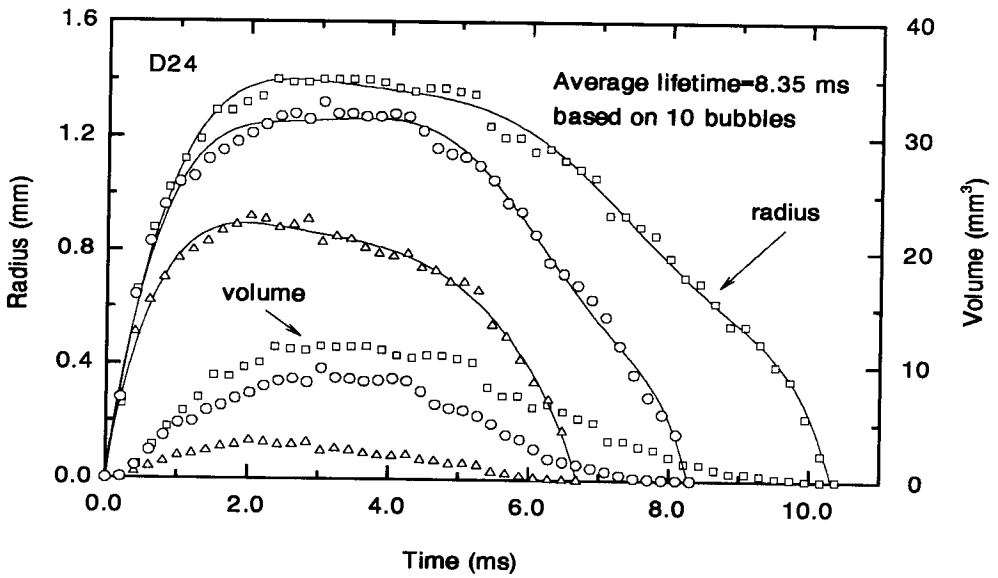

Figure 3.14. Selection of an 'average bubble' for condition D24.

CHAPTER 4

RESULTS AND DISCUSSION

This chapter describes the characteristics of a typical vapour bubble in subcooled boiling through the analysis of high-speed photographs, discusses the effect of experimental conditions (heat flux, subcooling, flow rate) on bubble parameters (R_m, t_c, t_m, t_b), and presents simple correlations for the bubble parameters based on the experimental data.

4.1 Observations on Bubble Dynamics in Convective Subcooled Boiling

Figure 4.1 shows the high-speed filming results of the growth and collapse process of a typical bubble photographed at mean flow velocity of $V=0.4\ m/s$, bulk subcooling of $\Delta T_{sub}=20\ °C$ and heat flux of $\phi\ =0.3\ MW/m^2$ (Reference condition D24-10). Figures 4.2 - 4.6 shows the digitized results for this bubble.

4.1.1. Bubble Growth and Collapse Curves

Figure 4.2 shows the temporal variation of the bubble volume and the equivalent spherical radius. The bubble lifetime is divided into two regions of growth and condensation separated by the solid line. The condensation region is further divided into two sub-regions: condensation on the wall and condensation after ejection (distinguished by the dashed line). The growth region included the period from nucleation to the

maximum bubble size and the condensation region comprised the remaining portion of the bubble lifetime where bubble size decreased first while attached to the heater surface and later after being ejected[1] into the flow. The duration of each region depended on the experimental conditions (see Section 4.2).

Based on Akiyama's[38] conclusions on the superheated layer thickness(section 2.5), the bubble spends only a small fraction of its growth in the superheated layer ($t<0.10\,t_m$). Therefore the bubble growth is influenced more by micro/ macro-layer evaporation, than by conduction through the superheated layer. At the end of the growth period, characterized by the maximum bubble size, evaporation from the bubble base is balanced with condensation at the bubble top surface. At this part of the bubble lifetime, the bubble top surface has intruded well into the subcooled core, and the condensation at the bubble interface becomes dominant while the bubble is still in contact with the heater surface. Meanwhile, a surface tension gradient is formed along the bubble interface due to temperature gradient across the flow[9]. This surface tension gradient is the driving force for the bubble ejection from the wall. The condensation rate increases slightly after bubble detachment due to the lack of bubble contact with the heater surface and due to the bubble distance from the superheated layer. The following observations were made on bubble ejection:

- In high subcooling (*60 °C*) most of the condensation occurred while the bubble was attached to the wall, although ejection was still present. This differs from the results of Gunther[35] who observed that bubbles grew and collapsed on the heater surface as hemispheres.
- Contrary to void growth model assumptions that the OSV point coincided with bubble ejection, ejection was observed well before the point of OSV.

---

[1] The term 'ejection' used in this thesis refers to the departure of the bubble from the heated surface.

- Unlike pool boiling, the ejection of a bubble did not occur at its maximum size. This confirms the observations of Tolubinsky and Kostanchuck[39].

4.1.2. Bubble Shape

Figure 4.3 shows the change in bubble shape characterized by the variation of the bubble diameters along the bubble principal axes (D_p, D_n) with the ratio $F = \frac{D_p}{D_n}$ representing the flatness of the bubble shape. In the growth region, the bubble shape was ellipsoidal with a maximum flatness of approximately *1.6* reached at $\frac{t}{t_{ejc}} \approx 0.2$ where t_{ejc} is the time at detachment. As the bubble grew, the shape changed from ellipsoidal to spherical. At the point of detachment, the shape of bubble resembled a tear drop (pear shape) with a flatness of approximately *0.8*. In the condensation region after detachment, the bubble shape became highly irregular and was approximated by an ellipsoid for the purpose of analysis. The observations on bubble shape agree with similar observations of Akiyama[38]. The bubble face adjacent to the heater underwent the greatest and most irregular deformation immediately after detachment. This deformation is perhaps due to surface tension gradient adjacent to the heater surface.

Contrary to the observations of continuous transformation in bubble shape, most researchers have assumed that the bubble shape approximated a spheroid throughout bubble lifetime with an effective radius defined by the average of the maximum and minimum radii of the irregular shape. Figure 4.4 shows the volume measured in this study compared with the volume evaluated with the spheroidal assumption. The value of the maximum volume is underpredicted by approximately *15%* with the spheroidal assumption.

For comparison of the bubble sizes obtained in this study with those of the literature, the measured volume is converted to an equivalent spherical radius from:

$$R = \left(\frac{3Vol}{4\pi}\right)^{1/3} \tag{4.1}$$

In Figure 4.2, the measured volume and the equivalent spherical radius with the above definition (4.1) are shown for reference condition D24. The growth and collapse regions are defined from the volume graph since the maximum bubble size is clearly defined by the curve fitted through the experimentally obtained points. The curve fitted through the calculated radius points has a flatter maximum due to the definition of the radius with equation (4.1) where the radius is given as the function of the third root of the volume.

4.1.3 Parallel and Normal Displacements

Figure 4.5 presents the normal and parallel displacement of the bubble centroid with respect to the nucleation site on the heater surface. The bubble translation velocity parallel to the heater, defined by the slope of the parallel displacement curve, is constant throughout the growth and collapse process and is of the order of magnitude of the mean flow velocity. Table 4.1 lists the slip ratio, defined as the ratio of bubble translation velocity parallel to heater surface to mean flow velocity, for the different conditions. The values of the slip ratio ranged from *0.71 - 2.33,* dependent on local conditions. No dependence of slip ratio on bubble size was found unlike Gunther[35] who reported an average value of *0.8* increasing slightly with the bubble size. Akiyama[38] reported values of *0.3 - 0.8* for the slip ratio, constant throughout the process of growth and collapse and independent of the bubble size.

The normal velocity of the bubble, defined by the slope of the normal displacement of bubble centroid with respect to the heater surface, is shown in Figure 4.5. The growth and ejection regions are marked by high normal velocity of the bubble centroid while at the maximum bubble size the normal velocity is approximately zero. The ejection velocity, defined by the slope of the line through the points past the dotted line, was evaluated for

most conditions (see Table 4.1). The values of ejection velocities fell into the range of *0.36* to *1.13 m/s*. With higher temperature gradient anticipated at higher subcooling, the ejection velocity was expected to depend on the bulk liquid subcooling. However, such a dependence was not established from the experimental data.

Figure 4.6 displays the path of the bubble centroid for different subcoolings at constant flow velocity and heat flux. The origin in the graph corresponds to the location of the nucleation site with the y-axis representing the heater surface. The flow is in the direction of positive y-axis. The bubble path curves in the direction of the cross-flow before bubble ejection which indicates the influence of the cross-flow. However, the ejection of bubble into the flow marks a change in the slope of the displacement curve which demonstrates the high normal velocity of the bubble compared to the mean flow velocity. At high subcoolings (ΔT_{sub}=60 °*C*), the bubble normal and parallel displacements were limited to the vicinity of the wall due to the rapid condensation process; at low subcooling, the bubble traveled farther and penetrated more deeply into the flow. The bubble behavior at high subccoling might explain the reason why some researchers described a distinct region close to the heater surface as the 'bubble boundary layer' (Jiji and Clark[48]).

4.2 Effect of Experimental Conditions on Bubble Parameters

4.2.1 Maximum Radius

Figure 4.7 shows the effect of flow velocity and heat flux on bubble maximum radius for constant subcooling of *30 °C* and for flow velocities of *0.40* and *0.80 m/s*. As indicated by the scatter of the data points for the two flow velocities, the effect of flow velocity on maximum bubble radius is negligible. The effect of flow velocity is appreciable when a relative velocity between the bubble and the flow exists. However, in section 4.1.3, it was

shown that bubbles translated with the velocity of the flow. Akiyama[38], in similar experiments evaluating the effect of flow velocity on bubble size, concluded that increased flow velocity decreased the bubble maximum size at mean flow velocities greater than 0.3 m/s (see Figure 2.8). The scatter of Akiyama's data points at flow velocity of *1 m/s* and the small change in the values of maximum diameter for flow velocity range of *0.1* to *1 m/s* at low subcooling do not support his proposed limit of *0.3 m/s*. The same is valid for the other bubble parameters. From the present experimental data and Akiyama's data, the effect of flow velocity on bubble parameters is concluded to be negligible for flow velocities smaller than 1 m/s.

Figure 4.8 presents the effect of heat flux and subcooling on the maximum bubble radius for subcoolings of *20* to *60* °*C*. At low subcoolings, an increase in heat flux reduced the maximum bubble size. At high subcoolings, the maximum radius was independent of heat flux. For a given heat flux, increased subcooling resulted in smaller bubble sizes at the vicinity of ONB. At high heat fluxes (near the OSV point), the maximum radius was independent of both the heat flux and liquid bulk subcooling. The decrease of the maximum bubble radius with increasing heat flux and the constant value of maximum radius at higher subcoolings are consistent with the experimental results of Gunther[35] and Del Valle and Kenning[37] respectively. The maximum radii obtained in this work are slightly larger than those of Akiyama[38] for the same subcooling (see Figure 2.8). This could be either due to the choice of the nucleation site or the selection of the 'average' bubble.

Table 4.2 compares the experimental maximum bubble radii with maximum radii predicted by theories of Unal[28], Zuber[23] and Mikic et al.[24]. Unal derived an expression for the maximum radius based on the micro-layer evaporation theory. He assumed that bubble growth resulted from the evaporation of the thin liquid film formed at the bubble base balanced by the dissipation of heat to the surrounding subcooled liquid at the bubble top surface. The expression for the maximum radius, Equation (B.18), is derived

in Appendix B. Unal underpredicted the maximum radius for all the conditions (see Table 4.2). The range of predicted radii fell between *0.17* to *0.46 mm.* In Unal's model an increase in the heat flux resulted in an increase in the bubble size, contrary to the observations of this investigation. Moreover, referring to Equation (2.22), the expression given by Unal does not contain a maximum and the model does not predict the entire cycle of bubble growth and collapse as shown in Figure 2.4.

Zuber[23] derived an expression for the maximum bubble radius by assuming that bubble growth was due to the evaporation of the liquid to vapour at the bubble interface by the supply of heat from the superheated layer (see section 2.2.2). The energy balance yielded an expression in which the maximum bubble radius is inversely proportional to the heat flux and directly proportional to the wall superheat, $\frac{(T_w - T_{sat})^2}{q}$, (see Equations 2.16 and 2.17). Therefore, in evaluating the maximum radius with Zuber's expression, the experimental wall superheat was used. Contrary to Unal's predictions, Zuber predicted a range of radii that was closer to the experimentally obtained radii except at low flow rate ($V=0.08$ *m/s*) at which the predictions were up to three times the maximum radii obtained in this study. In this study the wall temperature increased with increased heat flux; however, the trend was not linear (see Table 4.2). Due to the dependence of the wall superheat on the heat flux, Equation (2.16) predicts increasing as well as decreasing maximum radii with increased heat flux.

Mikic et al [24] used a similar approach to Zuber in analyzing bubble growth (see Section 2.2.2). The expression derived for the maximum radius, Equation (2.20), unlike Zuber's model, contained the effect of liquid subcooling as well as wall superheat. The expression, more complicated than that proposed by Zuber, contained an additional parameter, the growth time, the value of which was taken from this experiment. Mikic's predictions were comparable to Zuber's predictions except at low flow rates which Mikic

predicted lower values closer to those of the present study. The effect of increased heat flux on bubble maximum radius was inconsistent, perhaps due to the experimental values of wall superheat and growth time input into Mikic's model.

In none of these models are the phenomena of decreasing bubble size with increasing heat flux embedded in the theory and the theoretical results do not predict the trend in the experimental observations. Gunther has shown that with increased heat flux the density of nucleation site and the frequency of bubble formation increase significantly. It follows that, as heat flux is increased, the energy input to the flow will be distributed among more nucleation sites. The result is a smaller amount of energy per nucleation site and hence smaller bubble sizes. Therefore, the inability of these models to predict the observed trend of decreasing maximum bubble radius with increasing heat flux indicates a need for a correlation based on the experimental results of the present study.

4.2.2 Bubble Growth Time

The effect of heat flux on the bubble growth time for subcoolings of *20* to *60 °C* is shown in Figure 4.9. The trend, similar to the trend of decreasing maximum radius with increasing heat flux, implies that the growth time is proportional to the maximum radius, i.e., the larger the maximum radius, the longer the growth time. Akiyama also showed that the maximum growth time followed the same trend as that of the maximum radius when the effect of flow velocity was investigated. Gunther[35] and Del Valle and Kenning[37] showed that the bubble lifetime followed the same trend as that of the maximum radius versus heat flux.

Table 4.3 shows the ratio of growth and condensation time to bubble lifetime for all the experiments. The values for the ratio of bubble growth time to bubble lifetime fell in the range of $\left(0.27 < \frac{t_m}{t_b} < 0.44\right)$ with an average value of *0.33*± *0.04* based on all the

experiments. Akiyama[38] reported a range of *0.2-0.5* and found a range of *0.3-0.55* for Gunther's data.

4.2.3 Bubble Condensation Time

Figure 4.10 presents the effect of heat flux on the condensation time for subcoolings of *20* to *60* °*C*. An increase in heat flux is accompanied by a decrease in condensation time. However, this decrease is not the result of the direct effect of heat flux or superheat but that of the small maximum bubble sizes obtained at high heat fluxes. Since the growth time was found to be proportional to the maximum bubble radius, the condensation time is also expected to be proportional to the maximum bubble radius. At a given subcooling, the larger bubbles will take longer to condense.

Table 4.4 compares the condensation time obtained in this study with the analytical predictions based on inertia-controlled collapse by Akiyama[30] (Equation 2.24) and heat-transfer-controlled collapse by Florschuetz and Chao[31] (Equation 2.28). Akiyama's predictions were up to two orders of magnitude lower than the experimentally obtained condensation times. Florschuetz' predictions at low subcooling of *10* °*C* compared well with the experimental results but at higher subcoolings the predictions were up to two orders of magnitude lower than the experimental values. These discrepancies might be due to the assumption of uniform subcooling in the derivations of the models. This assumption might not be valid in subcooled boiling since, as shown earlier, the condensation process commences adjacent to heater where large temperature gradients exist and local subcooling differs from the bulk subcooling. Better agreement at low subcooling between the experimental values and the predictions of Florschuetz et al. could be explained by the fact that, at low subcooling, the difference in temperature between the main flow and the wall is smaller so that the assumption of uniform temperature during the condensation stage may be justified.

A better estimation of the local subcooling should include the effect of the radial temperature gradient in the flow. In this study, the temperature across the flow was not measured. However, the temperature across the flow during subcooled nucleate boiling is given by Forster[49] as:

$$T(Y) = T_{sat} + \left(\Delta T_w + \Delta T_{sub}\right)e^{\frac{-Y}{H}} - \Delta T_{sub} \tag{4.2}$$

where ΔT_w is the wall superheat and H is the thermal layer thickness defined as the distance where the non-dimensional temperature difference in Equation (4.2) drops to *1/e*. Akiyama obtained values of *0.05* to *0.2 mm* for the thermal boundary layer thickness for a velocity range of *0.08* to *0.8* m/s, respectively. An estimate of the local subcooling, based on the temperature of the liquid at a distance equal to bubble diameter and the saturation temperature is given by:

$$\left(\Delta T_{sub}\right)_{local} = \frac{T(Y = 2R_m) + T_{sat}}{2} \tag{4.3}$$

Since the thermal boundary layer thickness is small compared to the maximum bubble diameter, the liquid temperature at $Y=2R_m$ can be approximated by the bulk liquid temperature. This approximation limited the range of local subcooling to *5 - 30 °C* from bulk subcoolings of *10- 60 °C* respectively. The condensation time was recalculated from Equation (2.28) using the local subcooling from Equation (4.3). This recalculation resulted in higher condensation times overall as expected. However at low subcooling a small change in the value of local subcooling resulted in a drastically changed value of the condensation time because Equation (4.28) has a steep slope at low subcooling (see Figure 2.7). The refinement of this approach was not pursued since Equation (4.3) was found to represent poorly the condensation rates obtained in this experiment and is further discussed in Section 4.3.1.

4.2.4 Effect of Subcooling on Bubble Parameters at *V=0.08 m/s*

The lowest inlet temperature that could be achieved with the loop was approximately *15 °C* . Since reaching the point of OSV at low flow rates *(V=0.08 m/s)* required an inlet temperature lower than *15 °C,* the effect of subcooling was investigated at only one value of heat flux. Figure 4.11 presents the effect of subcooling on the maximum radius, bubble growth time, condensation time and bubble lifetime for a heat flux of $0.20\ MW/m^2$. The same trend of decreasing values of bubble parameters with increased subcooling is observed as previously shown for higher flow rates.

Over the entire range of the present experimental conditions, the maximum bubble radius ranged from approximately *0.50 mm* at high heat fluxes and high subcoolings up to *1.75 mm* at low heat flux and low subcoolings. Table 4.5 compares the experimentally obtained values for the maximum radius and bubble lifetime with similar experiments performed at atmospheric pressure. The range of maximum radii and bubble lifetime obtained in this study is larger than that of Akiyama's similar study due to the range of bulk subcoolings *(20-80 °C)* used by Akiyama compared to the present range of *(10-60 °C)*.

4.3 Correlations

4.3.1 Normalized Bubble Growth and Collapse Curves

Zuber's[23] non-dimensional expression (Equation 2.15) for the instantaneous bubble radius was based on heat-transfer-controlled growth and collapse of a single bubble. Figure 4.12 shows the experimental data normalized with maximum radius and growth time and compared to Equation 2.15. In the growth region, Zuber's growth-rate predictions matched the experiments; however, the normalization procedure failed in the condensation region.

Akiyama[38] suggested a correlation for the bubble growth and collapse curves in terms of maximum bubble radius and bubble lifetime:

$$\frac{R}{R_m} = 1 - 2^K \left| \frac{1}{2} - \left(\frac{t}{t_b} \right)^N \right|^K \tag{4.4}$$

where N and K are constants. N was evaluated from the fact that at $t/tm=1$, $R/Rm=1$:

$$\left(\frac{t_m}{t_b} \right)^N = \frac{1}{2} \tag{4.5}$$

and the parameter K was found by the curve being fitted to the data. Akiyama used a value of $K=3$ and found a value of $K=2$ for Gunther's data. Figure 4.13 compares the experimental data normalized with the maximum bubble radius and bubble lifetime with equation (4.4) for the adjusted values of $K=2.2$ and $N=0.67$ [2] based on experimental results:

$$\frac{R}{R_m} = 1 - 2^{2.2} \left| \frac{1}{2} - \left(\frac{t}{t_b} \right)^{0.67} \right|^{2.2} \tag{4.6}$$

A good representation is obtained for both growth and condensation regions by the use of Equation (4.6).

Figure 4.14 compares the growth rate obtained by Equation (4.6) with the predictions of the growth models described in Chapter 2, and Akiyama's correlation with $N=0.66$ and $K=3$. Growth rates obtained in this work are in good agreement with the growth models of Mikic and Zuber. Unal predicted lower growth rates with the micro-macro layer evaporation model.

Figure 4.15 compares the collapse rates obtained with Equation (4.6) with the collapse rates predicted by the inertia-controlled and the heat transfer-controlled collapse

---

[2] The values of t_m/t_b are shown in Table 4.5. In evaluating N, a value of t_m/t_b=0.36 was used.

models[30,31]. The shape of the experimental curve is similar to those of the inertia-controlled models with the experimental collapse rates lower at the beginning of the condensation stage. This result contrasts with the heat-transfer-controlled collapse models in which the condensation process is fast at the beginning and slow at the end of the condensation stage. It was shown in Section (4.2.3) that at low subcooling, the condensation time was in good agreement with the heat transfer-controlled predictions. Figure 4.16, which compares an experiment at low subcooling to the Florschuetz' model, shows that even though the condensation times for the experiment and the theory are approximately the same, the collapse rates differ significantly. In the experiments, as bubbles condense on the heater surface, slower collapse rates are expected. When bubbles eject inside the subcooled liquid, higher condensation rates are expected due to the larger temperature gradients between the vapour and the bulk liquid. Higher temperature gradients imply higher heat transfer rates through the bubble wall and lower bubble wall temperatures with lowest possible wall temperature of T_{sat}. This assumption implies an isothermal collapse which is the assumption in inertia-controlled collapse models. In the actual case, due to the lack of perfect heat transfer rates, the bubble wall temperature is higher than the saturation temperature so that a slower condensation rate is expected (see the experimental curve Figure 4.15).

4.3.2 Correlations for Bubble Parameters

The experimental results compared to those of different theoretical models led to the conclusion that the expression given by Mikic, Zuber and Unal for the maximum radius of the bubble did not predict the experimental results, i.e., their prediction of increasing bubble size with wall superheat contradicted those of Gunther, Del Valle and Kenning and the present study. Comparison of the experimental values of the condensation time did not compare well with models proposed by Akiyama and Florschuetz et al.. Therefore,

correlations had to be developed in order to predict the maximum radius and the lifetime of the bubble at the subcooled nucleate boiling for heat flux range corresponding from ONB to OSV. The result of these correlations for bubble maximum radius, growth time and condensation time is the subject of this section.

The bubble lifetime is divided into two regions for the purpose of the correlations: the growth region and the condensation region. In the growth region, the effect of heat flux and subcooling are considered the most significant parameters that limit the maximum bubble size and the growth time is assumed to be directly proportional to the maximum radius. In the condensation region, the time for the bubble to condense is assumed to be a function of the degree of subcooling and the maximum bubble size.

In the correlation of the maximum bubble radius two non-dimensional numbers are used:

$$Ja_w^* = \frac{\rho_l C_{pl}(T_w - T_{sat})}{\rho_v i_{fg}} \tag{4.7}$$

$$\theta = \frac{T_w - T_B}{T_w - T_{sat}} \tag{4.8}$$

The effect of heat flux is shown with modified Jacob number, Ja_w^*. In this study, its value ranged from *45* to *110* with higher values of Ja_w^* indicating larger wall superheat. The properties ρ_l and C_{pl} are evaluated at saturation temperature since during growth the bubble is close to the heated surface where the bulk temperature of the liquid is close to the saturation temperature. The non-dimensional temperature difference, θ, represents the degree of liquid subcooling. The values of θ ranged form 1.3 to 4 with the larger values of θ indicating higher degree of subcooling.

The maximum bubble radius is non-dimensionalized with R_m^+:

$$R_m^+ = \frac{R_m \sigma}{\rho_l \alpha_l^2} \tag{4.9}$$

where α_l, ρ_l, σ are evaluated at the saturation temperature. This non-dimensional number, used by Cooper and Chandratilleke[50] in the analysis of vapour bubble growth at a wall with a temperature gradient, was derived as a result of a non-dimensional analysis. Dimic[51] arrived at the same non-dimensional number (R_m^+) in his analytical work on bubble condensation in a subcooled liquid. A different approach for non-dimensionalizing the maximum radius was applied by Mikic[24] as $\frac{R_m}{\sqrt{\alpha_l t_m}}$. This required a knowledge of the growth time to obtain the maximum bubble radius, i.e., coupling the effect of the two bubble parameters.

The experimental data for the maximum bubble radius were correlated with Ja_w^* and θ as follows:

$$R_m^+ = 5.01 \times 10^9 \, Ja_w^{*\,-1.65} \theta^{\,-1.65} \tag{4.10}$$

The data points and the correlating line are shown in Figure 4.17. The coefficient of determination for this correlation was 0.70 (see appendix E). The correlation predicts a decrease in the maximum bubble size with increasing superheat and subcooling as expected. The equal exponents of Ja_w^* and θ indicate that wall superheat and subcooling are of equal influence in determination of the bubble maximum size.

Since the growth time is proportional to the maximum radius as shown in Section (4.2.2), the growth time is correlated with the same non-dimensional parameters as the maximum radius. The growth time is non-dimensionalized as[3]:

$$t_m^+ = \frac{\alpha_l t_m}{\left(\frac{\rho_l \alpha_l^2}{\sigma}\right)^2} \tag{4.11}$$

[3] This non-dimensional number was also derived from dimensional analysis by Cooper and Chandratilleke[50].

This non-dimensional time is similar to the Fourier number:

$$Fo_m = \frac{\alpha_l t_m}{(length\ scale)^2} \tag{4.12}$$

However, the length scale used in the denominator is consistent with the length scale used in the definition of $R_m^+ = \frac{R_m}{\left(\frac{\rho_l \alpha_l^2}{\sigma}\right)}$. Based on the experimental data, the following correlation was obtained for the growth time:

$$t_m^+ = 3.21 \times 10^{14}\, Ja_w^{*\ -2.58} \theta^{\ -2.88} \tag{4.13}$$

The data points and correlating line are shown in Figure 4.18. The coefficient of determination for this correlation is slighlty lower than the correlation for the maximum radius. Since the exponents for Ja_w^* and θ are almost equal, the growth time is assumed to be proportional to the maximum bubble radius, i.e.:

$$t_m = c\, R_m^x \tag{4.14}$$

where c and x are found by correlating t_m with R_m from the data:

$$t_m = 56.7\, R_m^{1.49} \tag{4.15}$$

Equation (4.15) provides a simpler expression to determine the growth time when the maximum radius is obtained.

The condensation time is expressed in terms of liquid subcooling and as a function of the maximum radius. The condensation time is non-dimensionalized with:

$$t_c^+ = \frac{\alpha_l t_c}{\left(\frac{\rho_l \alpha_l^2}{\sigma}\right)^2} \tag{4.16}$$

and correlated with the Jacob number and the non-dimensional maximum radius:

$$Ja = \frac{\rho_l C_{pl}(T_{sat} - T_B)}{\rho_v i_{fg}} \tag{4.17}$$

$$R_m^+ = \frac{R_m \sigma}{\rho_l \alpha_l^2} \tag{4.18}$$

Based on the experimental data , the correlating equation for the condensation time was given by:

$$t_c^+ = 106.8\, Ja^{-0.45}\, R_m^{+\,1.30} \tag{4.18}$$

The data points and the correlating line are shown in Figure 4.19. The coefficient of determination for this correlation was *0.96*. As expected, increasing the liquid bulk subcooling *Ja*, reduced the time of condensation. Moreover, the condensation time is directly related to the maximum size of the bubble.

Table 4.1 Slip ratio of bubbles in different conditions.

Ref Number	ΔT_{sub} (°C)	V (m/s)	ϕ (MW/m²)	V_b (m/s)	V_b/V	V_{ejc} (m/s)
D35	10	0.08	0.2	0.25*	3.13*	0.42
D36	10	0.08	0.3	0.05*	0.63*	0.36
D33	10	0.40	0.3	0.61	1.53	0.43
D27	20	0.08	0.2	0.35*	4.38*	0.60
D28	20	0.08	0.3	-0.11*	-1.38*	0.64
D24	20	0.40	0.3	0.44	1.10	0.79
D25	20	0.40	0.6	0.50	1.25	0.95
D26	20	0.40	0.7	0.93	2.33	0.42
D50	20	0.40	0.9	0.45	1.13	0.45
D21	20	0.80	0.6	1.08	1.35	0.49
D22	20	0.80	0.7	0.84	1.05	0.82
D48	20	0.80	0.9	0.89	1.11	1.28
D37	30	0.08	0.2	0.076	0.95	1.13
D05	30	0.40	0.3	0.37	0.93	0.75
D16	30	0.40	0.6	0.48	1.20	0.93
D17	30	0.40	0.8	0.54	1.35	0.44
D18	30	0.40	0.9	0.37	0.93	1.06
D51	30	0.40	1.2	0.80	2.00	1.03
D06	30	0.80	0.6	0.76	0.95	0.71
D13	30	0.80	0.8	0.81	1.01	1.01
D14	30	0.80	0.9	0.94	1.18	0.98
D49	30	0.80	1.2	0.83	1.04	0.69
D39	40	0.80	0.6	0.81	1.01	**
D40	40	0.80	0.9	0.60	0.75	**
D41	40	0.80	1.2	0.84	1.05	**
D42	60	0.80	0.6	0.60	0.75	**
D43	60	0.80	0.9	0.70	0.88	**
D44	60	0.80	1.2	0.57	0.71	**

*Bubbles in these conditions were affected by the growth and collapse of neighboring bubbles.

** Not available.

Table 4.2. Comparison of experimental maximum bubble radius with predictions of Unal[28] (Equation B.18.), Zuber[23] (Equation 2.16) and Mikic et al.[24] (Equation 2.20).

Ref Number	$\Delta T_{sub}(°C)$	$\dot{m}(^{Kg}/_{s})$	$\phi(^{MW}/_{m^2})$	$T_w(°C)$	$R_m(mm)$ Unal[28]	$R_m(mm)$ Zuber[23]	$R_m(mm)$ Mikic[24]	$R_m(mm)$ Experiment
D35	10	0.02	0.2	130.3	0.40	3.04	1.47	1.36
D36	10	0.02	0.3	131.8	0.46	2.24	1.13	1.16
D33	10	0.1	0.3	127.1	0.45	1.59	1.07	1.23
D27	20	0.02	0.2	128.3	0.28	2.62	1.17	1.77
D28	20	0.02	0.3	132.0	0.32	2.28	1.61	1.60
D24	20	0.1	0.3	124.6	0.30	1.29	0.99	1.33
D25	20	0.1	0.6	127.7	0.40	0.83	0.89	1.03
D26	20	0.1	0.7	129.9	0.42	0.84	0.87	0.73
D50	20	0.1	0.9	142.0	0.46	1.35	0.92	0.56
D21	20	0.2	0.6	126.0	0.35	0.73	0.71	0.79
D22	20	0.2	0.7	126.1	0.38	0.63	0.69	0.74
D48	20	0.2	0.9	141.1	0.42	1.29	0.80	0.64
D37	30	0.02	0.2	131.2	0.22	3.23	0.85	0.83
D05	30	0.1	0.3	120.6	0.24	0.81	0.64	0.86
D16	30	0.1	0.6	126.7	0.32	0.77	0.66	0.79
D17	30	0.1	0.8	126.5	0.36	0.57	0.62	0.53
D18	30	0.1	0.9	126.7	0.37	0.51	0.56	0.48
D51	30	0.1	1.2	132.3	0.42	0.58	0.67	0.46
D06	30	0.2	0.6	119.9	0.26	0.46	0.49	0.68
D13	30	0.2	0.8	123.5	0.32	0.44	0.55	0.61
D14	30	0.2	0.9	124.5	0.33	0.43	0.54	0.46
D49	30	0.2	1.2	131.0	0.37	0.53	0.54	0.51
D39	40	0.2	0.6	123.2	0.23	0.57	0.52	0.66
D40	40	0.2	0.9	125.1	0.28	0.45	0.67	0.71
D41	40	0.2	1.2	129.8	0.32	0.49	0.68	0.51
D42	60	0.2	0.6	123.6	0.17	0.59	0.43	0.52
D43	60	0.2	0.9	126.6	0.22	0.51	0.57	0.61
D44	60	0.2	1.2	130.1	0.25	0.50	0.60	0.54

Table 4.3. Ratio of condensation and growth time to bubble lifetime.

Ref Number	$\Delta T_{sub}(^{\circ}C)$	$\dot{m}(^{Kg}/_{s})$	$\phi(^{MW}/_{m^2})$	$\frac{t_c}{t_b}(\%)$	$\frac{t_m}{t_b}(\%)$
D35	10	0.02	0.2	67	33
D36	10	0.02	0.3	72	28
D33	10	0.1	0.3	66	34
D27	20	0.02	0.2	73	27
D28	20	0.02	0.3	67	33
D24	20	0.1	0.3	66	34
D25	20	0.1	0.6	68	32
D26	20	0.1	0.7	69	31
D50	20	0.1	0.9	63	37
D21	20	0.2	0.6	70	30
D22	20	0.2	0.7	71	29
D48	20	0.2	0.9	73	27
D37	30	0.02	0.2	66	34
D05	30	0.1	0.3	70	30
D16	30	0.1	0.6	71	29
D17	30	0.1	0.8	65	35
D18	30	0.1	0.9	65	35
D51	30	0.1	1.2	65	35
D13	30	0.2	0.8	68	32
D14	30	0.2	0.9	62	38
D49	30	0.2	1.2	71	29
D39	40	0.2	0.6	67	33
D40	40	0.2	0.9	56	44
D41	40	0.2	1.2	56	44
D42	60	0.2	0.6	71	29
D43	60	0.2	0.9	67	33
D44	60	0.2	1.2	67	33

Table 4.4. Comparison of condensation time with predictions of Akiyama[30] (Equation 2.24) and Florschuetz et al.[31] (Equation 2.28).

Ref Number	$\Delta T_{sub}(^{\circ}C)$	$\dot{m}(^{Kg}/_{s})$	$\phi(^{MW}/_{m^2})$	$t_c(ms)$ Akiyama	$t_c(ms)$ Florschuetz	$t_c(ms)$ Experiment
D35	10	0.02	0.2	0.1280	11.02	10.2
D36	10	0.02	0.3	0.109	8.02	7.2
D33	10	0.1	0.3	0.126	9.02	6.4
D27	20	0.02	0.2	0.118	4.74	8.1
D28	20	0.02	0.3	0.130	5.75	9.1
D24	20	0.1	0.3	0.088	2.67	5.5
D25	20	0.1	0.6	0.069	1.60	3.8
D26	20	0.1	0.7	0.049	0.81	3.3
D50	20	0.1	0.9	0.037	0.47	1.5
D21	20	0.2	0.6	0.053	0.94	3.0
D22	20	0.2	0.7	0.050	0.83	2.9
D48	20	0.2	0.9	0.043	0.62	1.9
D37	30	0.02	0.2	0.045	0.47	2.3
D05	30	0.1	0.3	0.047	0.50	3.7
D16	30	0.1	0.6	0.043	0.42	2.4
D17	30	0.1	0.8	0.029	0.19	1.7
D18	30	0.1	0.9	0.026	0.16	1.3
D51	30	0.1	1.2	0.025	0.14	1.3
D06	30	0.2	0.6	0.037	0.31	2.2
D13	30	0.2	0.8	0.033	0.25	1.9
D14	30	0.2	0.9	0.025	0.14	1.3
D49	30	0.2	1.2	0.028	0.18	1.2
D39	40	0.2	0.6	0.031	0.17	1.6
D40	40	0.2	0.9	0.034	0.19	1.4
D41	40	0.2	1.2	0.024	0.10	1.0
D42	60	0.2	0.6	0.020	0.05	1.2
D43	60	0.2	0.9	0.024	0.07	1.4
D44	60	0.2	1.2	0.021	0.05	1.2

Table 4.5. Comparison of experimental maximum radii with literature.

Investigator	$P(atm)$	$\phi(MW/m^2)$	$V(m/s)$	$\Delta T_{sub}(°C)$	$R_m(mm)$	$t_b(ms)$
Gunther [35]	1.7	2.3 - 10.7	1.5 - 6.1	33 - 110	0.13 - 0.50	0.10 - 0.40
Tolubinsky et al.[39]	1	0.05 - 1.0	0.08 - 0.2	5 - 60	0.20 - 0.65	N/A
Abdelmessih et al.[36]	1	0.19 - 0.46	0.92 - 2.30	1.9	0.15 -0.25	1.5 - 5.5
Akiyama[38]	1	0.1-0.8	0.1 - 5	20-80	0.20 - 1.0	0.40 - 5.0
Del Valle et al.[37]	1	3.44 - 4.67	1.7	84	0.20	0.40
This investigation	1	0.1-1.2	0.08 - 0.80	10 - 60	0.50 - 1.75	2 - 15

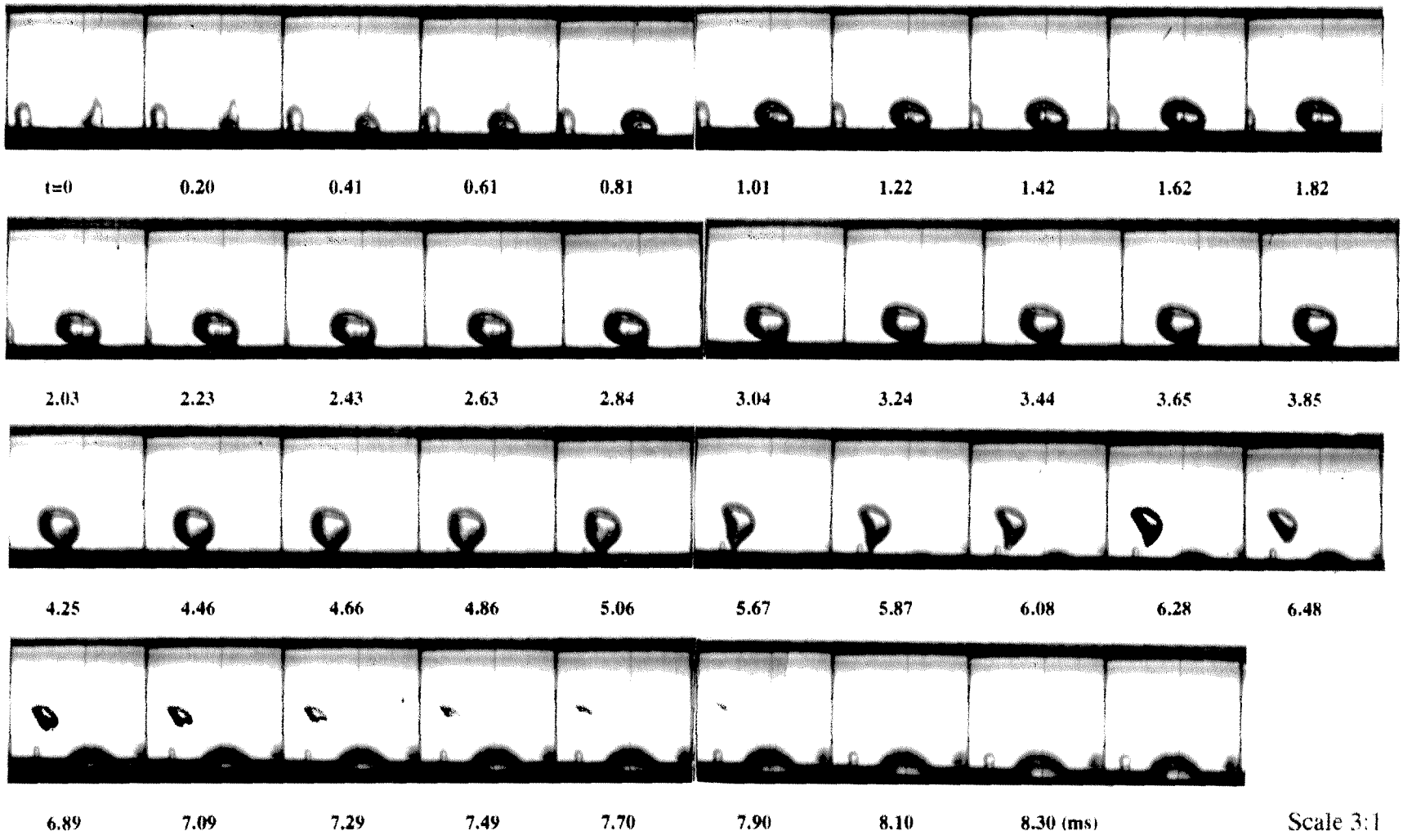

Figure 4.1. Photographs of bubble growth and collapse (D24-10) for V=0.4 m/s, ΔT_{sub}=20 °C and φ=0.3 MW/m^2

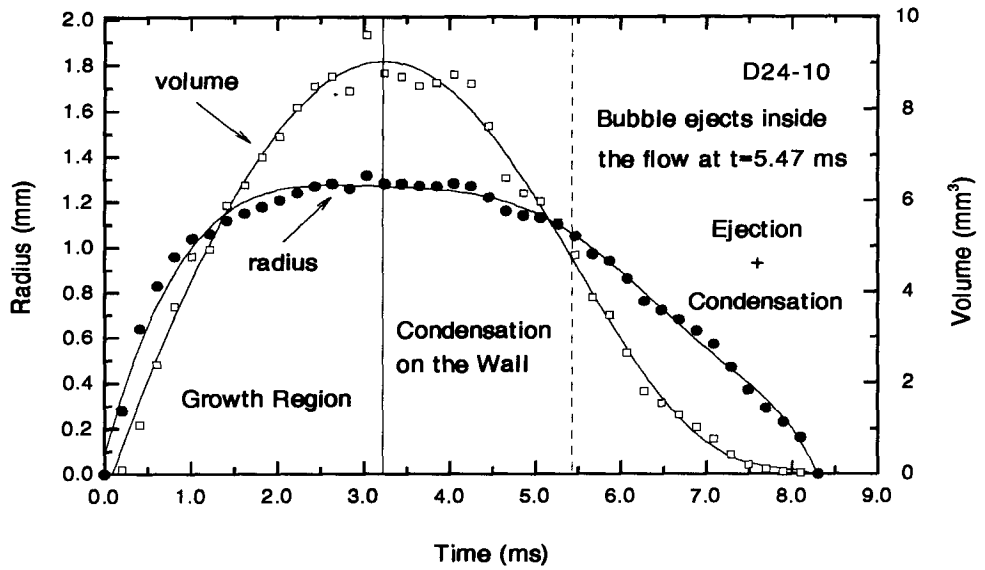

Figure 4.2. Growth and collapse curve for a typical bubble (D24-10)

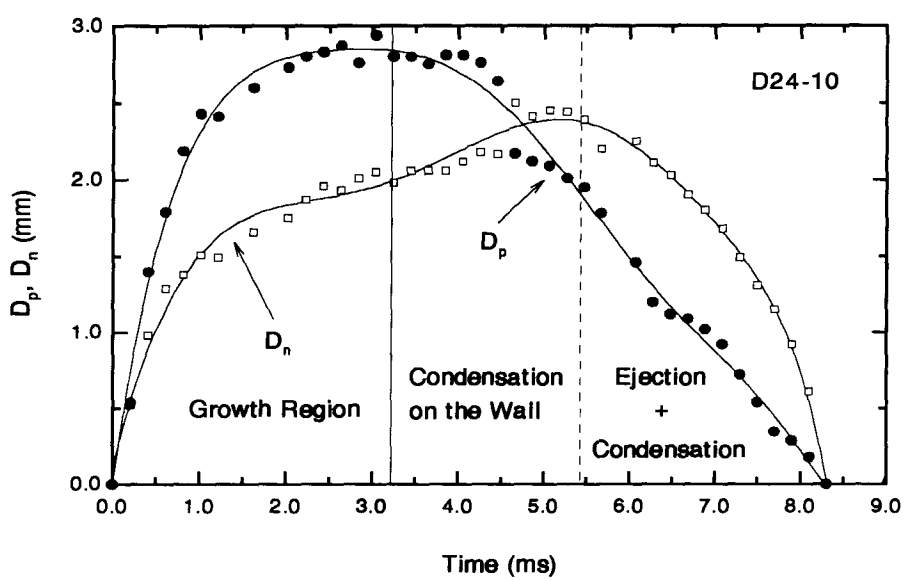

Figure 4.3. Change in bubble shape during its lifetime.

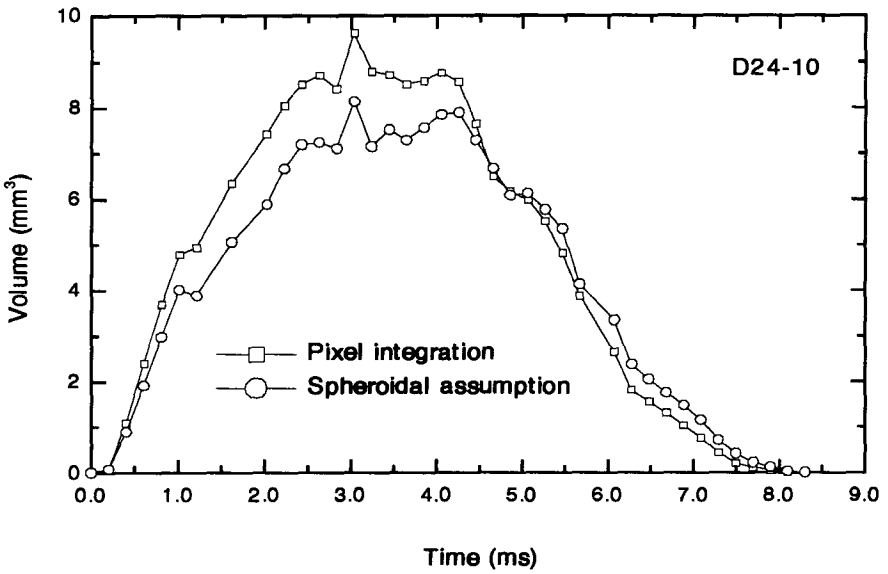

Figure 4.4. Comparison of bubble volume obtained in this study with volume evaluated by spheroidal assumption.

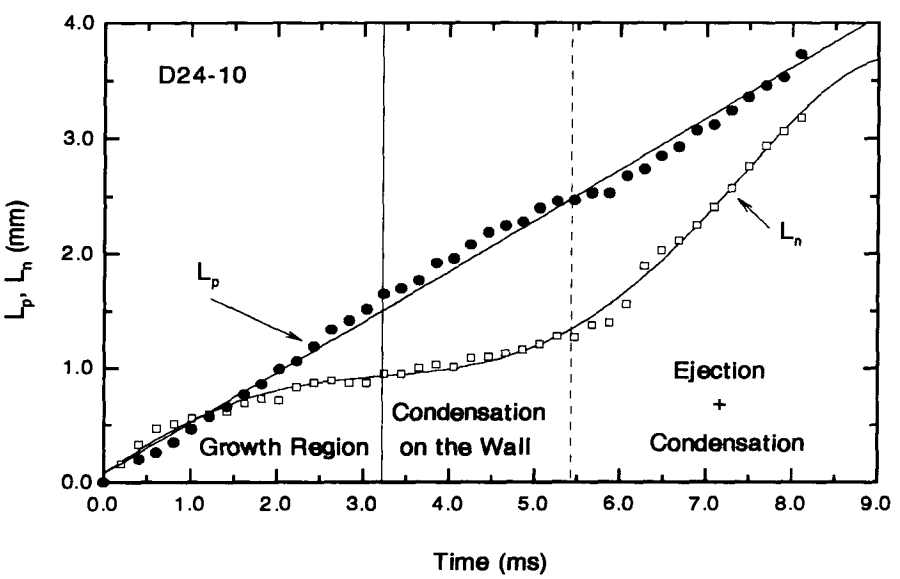

Figure 4.5. Normal and parallel displacement of the centroid of bubble

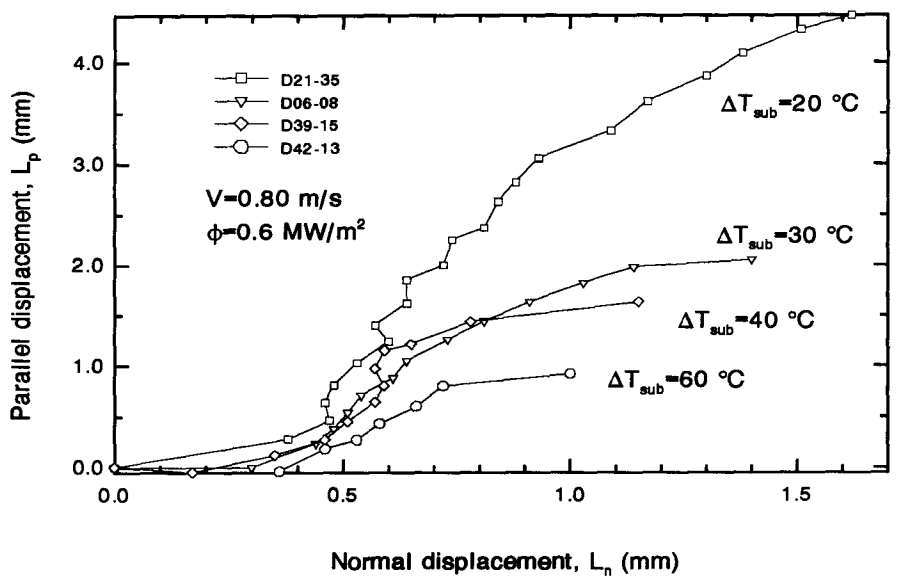

Figure 4.6. Bubble path in different liquid bulk subcooling.

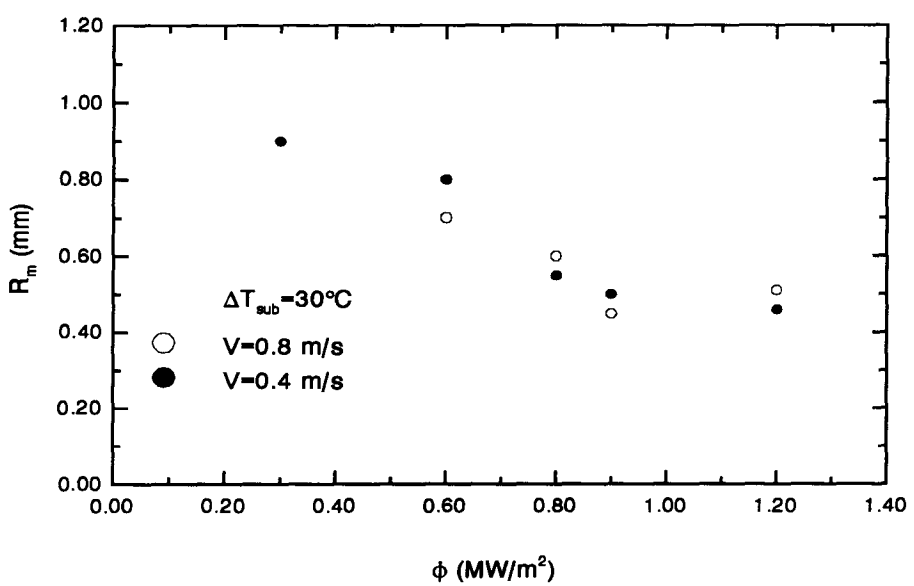

Figure 4.7. Effect of heat flux and flow velocity on bubble maximum radius.

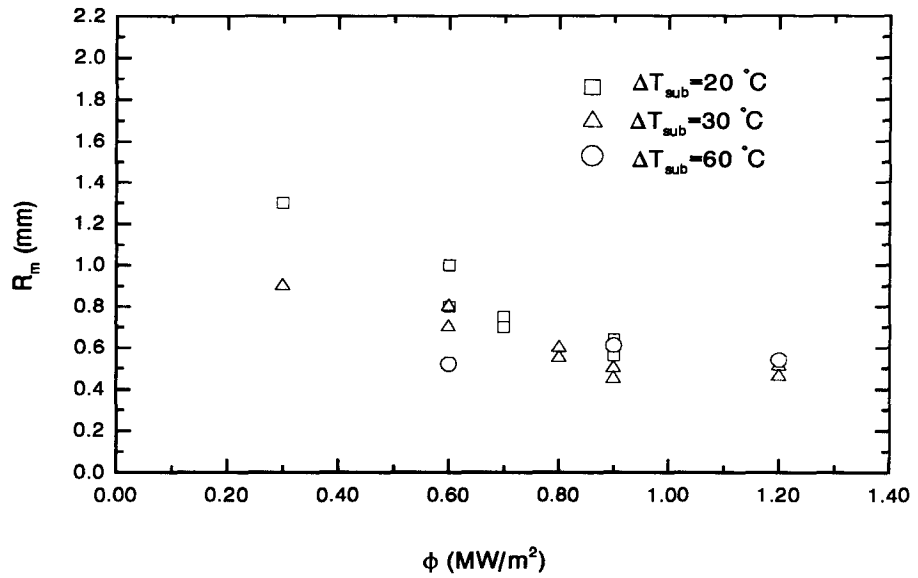

Figure 4.8. Effect of heat flux and subcooling on maximum bubble radius.

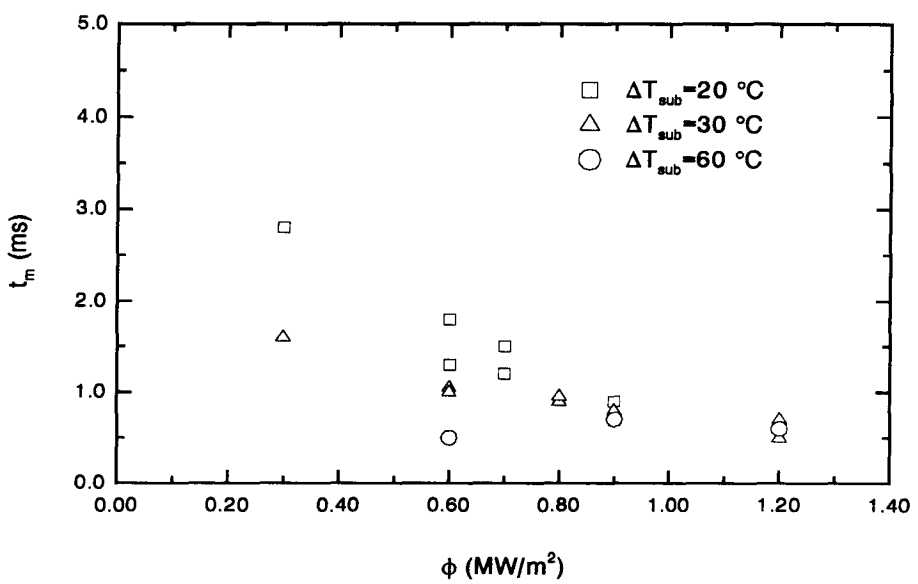

Figure 4.9. Effect of heat flux and subcooling on bubble growth time.

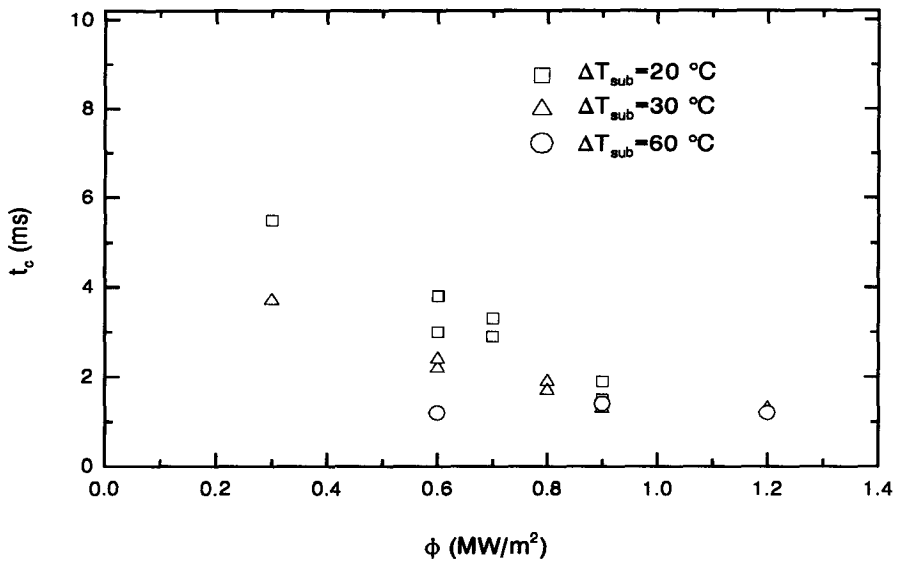

Figure 4.10. Effect of heat flux and subcooling on bubble condensation time.

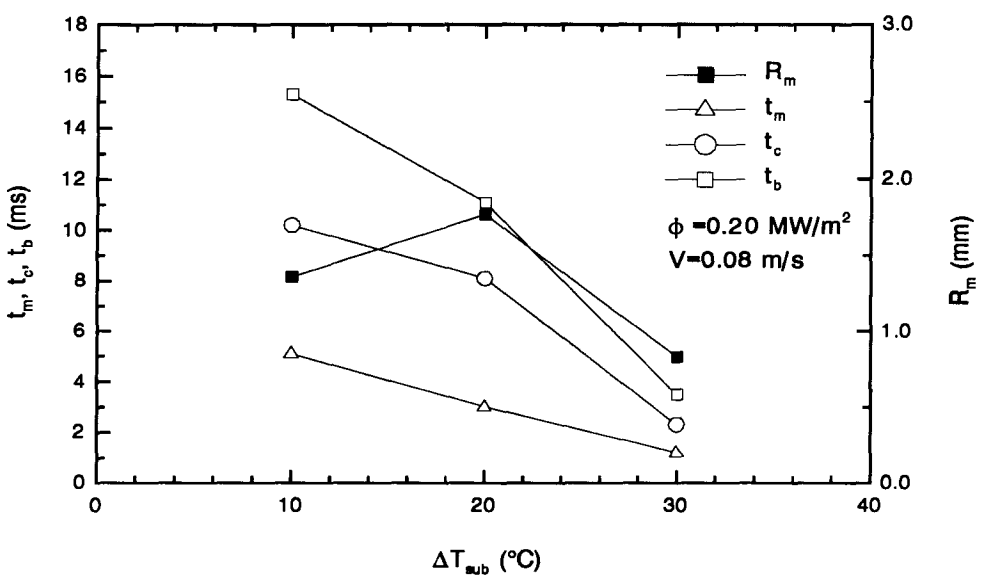

Figure 4.11. Effect of subcooling on bubble parameters at V=0.08 m/s.

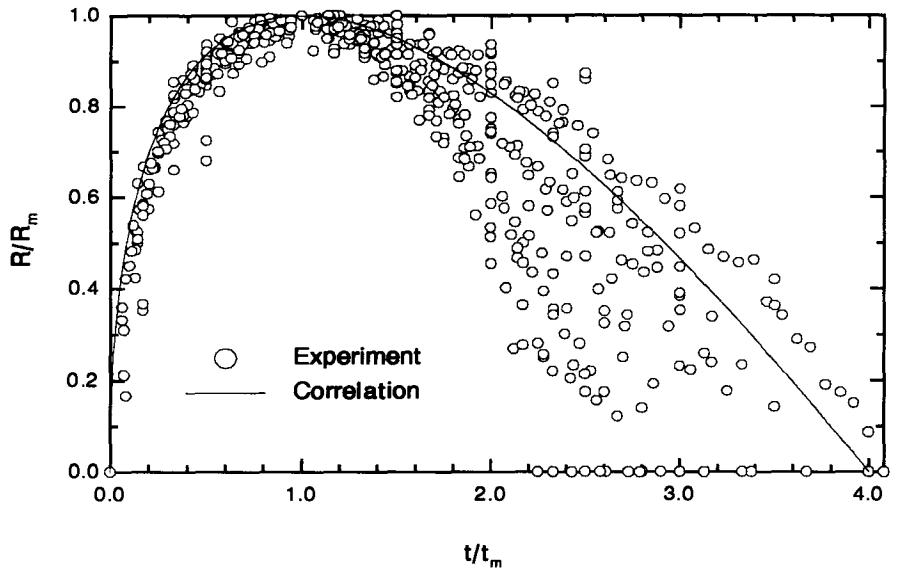

Figure 4.12. Comparison of experimental growth and collapse rate with Zuber[23].

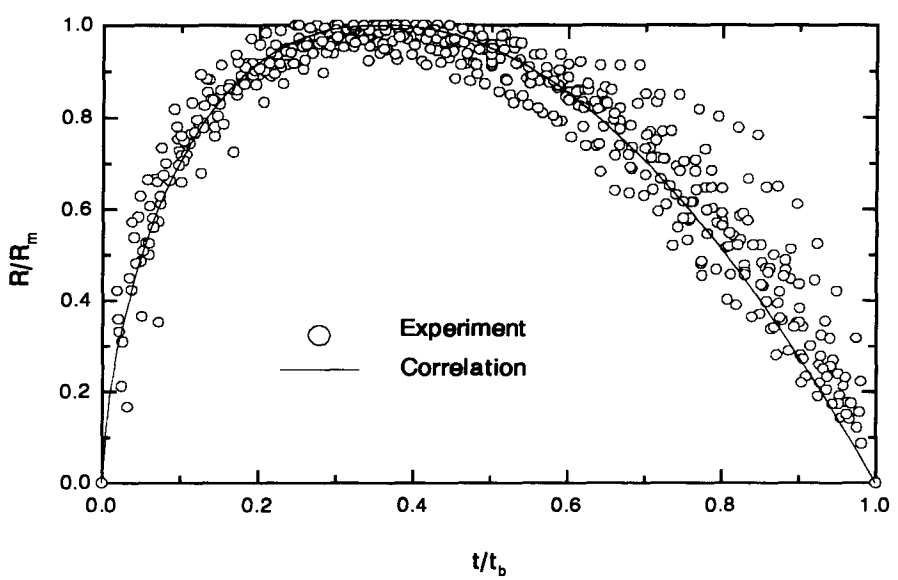

Figure 4.13. Correlation of bubble growth and collapse rates.

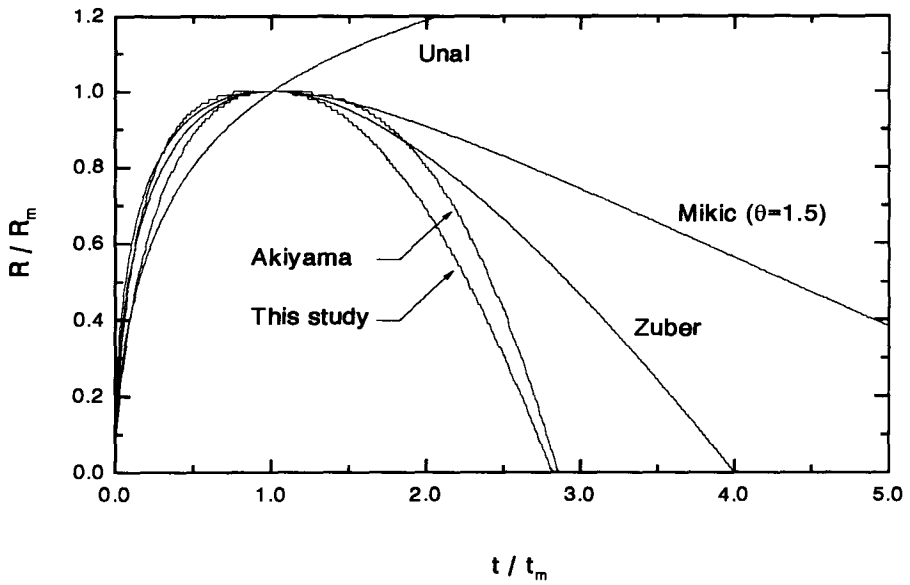

Figure 4.14. Comparison of experimental bubble growth rate Equation (4.6) with Akiyama[38] Zuber[23], Mikic et al.[24], and Unal[28].

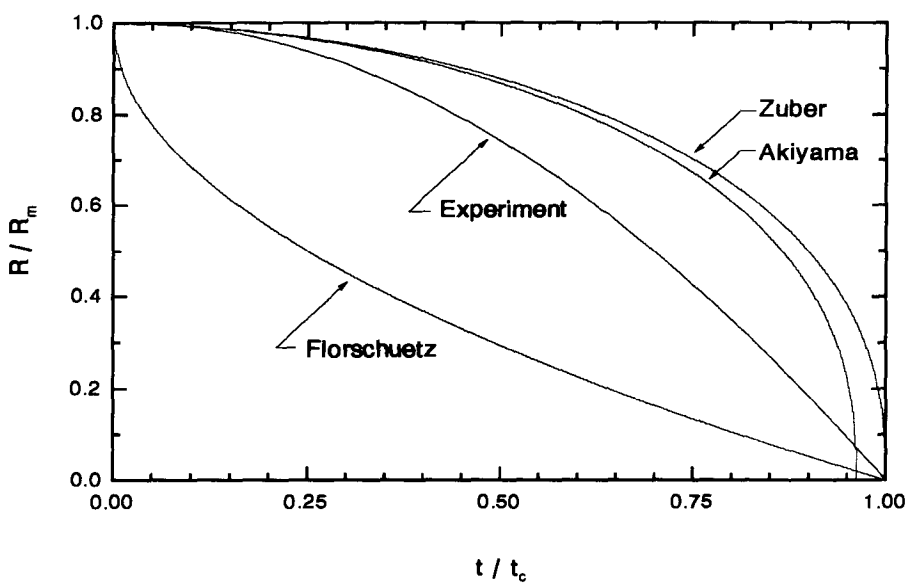

Figure 4.15. Comparison of experimental condensation rate Equation (4.6) with Akiyama[30], Zuber[23], and Florschuetz and Chao[31].

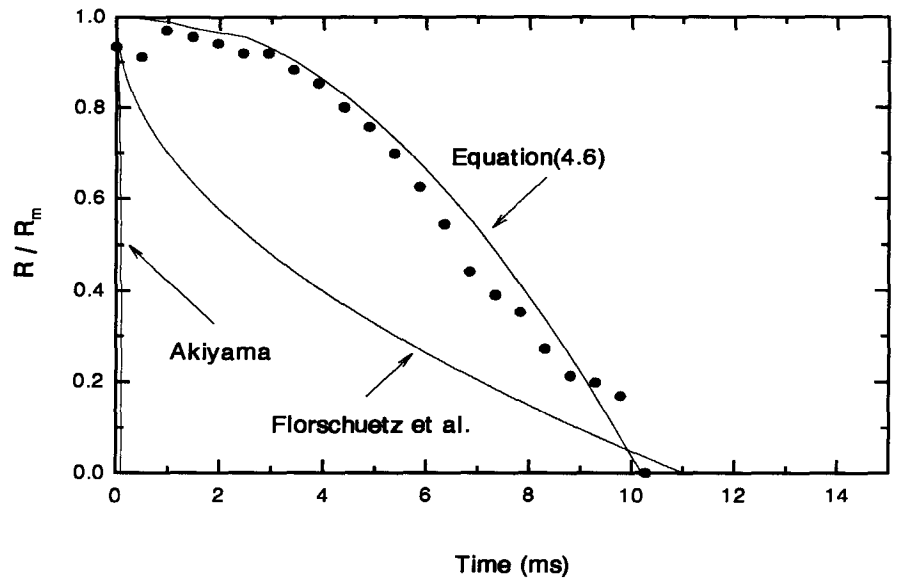

Figure 4.16. Comparison of experimental condensation rate at low subcooling with condensation models of Florscuetz and Chao[31] and Akiyama[30].

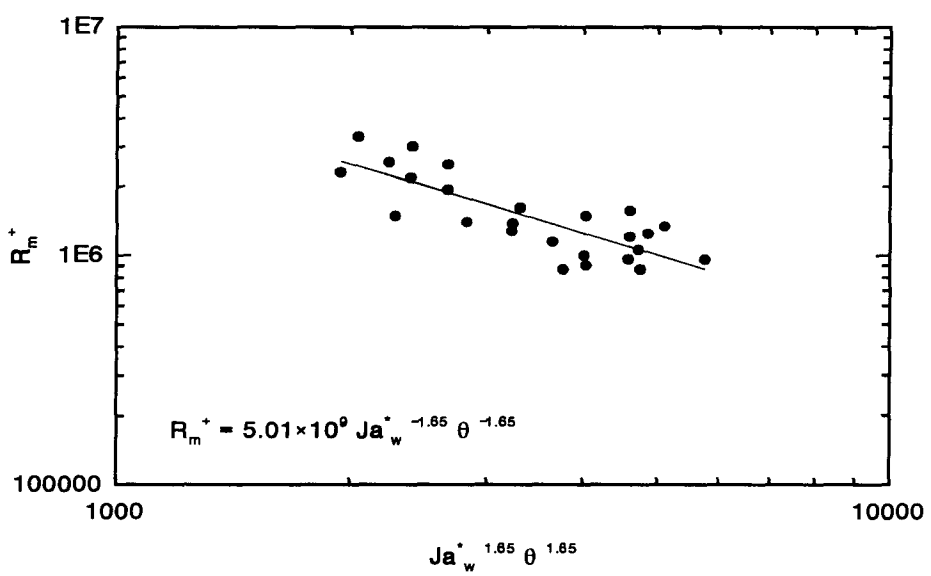

Figure 4.17. Correlation of maximum radius with Ja* and θ (average correlation error =20%).

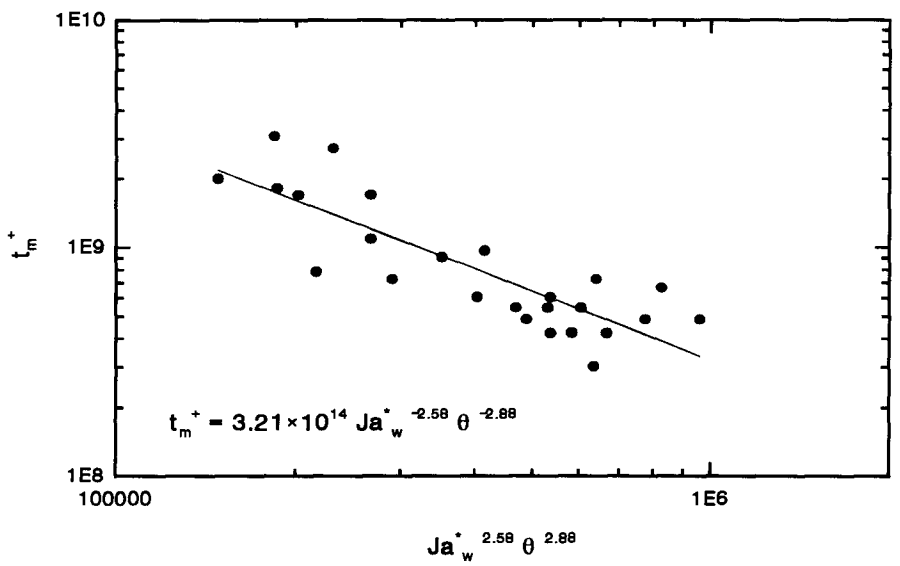

Figure 4.18. Correlation for growth time with Ja* and θ (average correlation error = 28%).

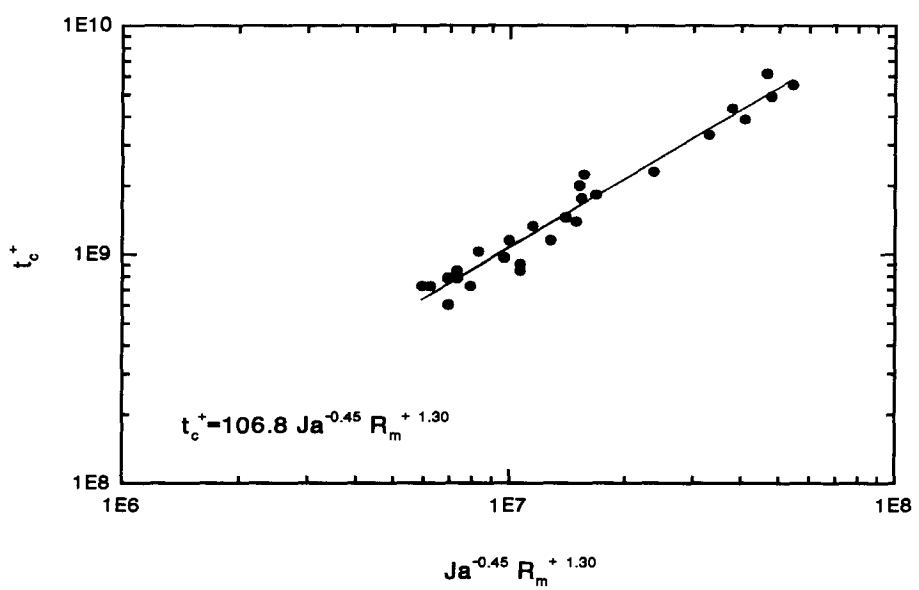

Figure 4.19. Correlation for condensation time with *Ja* and the non-dimensional maximum radius (average correlation error =12%).

CHAPTER 5

CONCLUSIONS AND RECOMMENDATIONS

5.1 Conclusions

The growth and collapse of vapour bubbles in subcooled convective boiling of water were investigated by high-speed photography to obtain insight on the mechanism of void growth at atmospheric pressure, mass flow rate of 0.02-0.20 kg/s, liquid bulk subcoolings of 10-60 °C, and heat fluxes of 0.10-1.20 MW/m^2. The effect of mean flow velocity, heat flux and liquid bulk subcooling on maximum bubble radius, bubble growth time, and bubble condensation time were investigated. Observations were made on the bubble translational velocity, ejection velocity and change in bubble shape during the bubble lifetime. Based on the analysis of high-speed photography the following were concluded:

1. The bubble lifetime was divided into two distinct regions of growth and condensation. The condensation region was further subdivided into condensation with bubble sliding on the wall and condensation after bubble ejected into the flow.

2. At high bulk liquid subcooling most of the condensation occurred while bubbles were sliding on the wall, though ejection was still present. The bubble radius at ejection was smaller than the maximum bubble radius attained at the end of the growth stage.

3. Bubbles translated parallel to the wall with a constant velocity approximately equal to the mean flow velocity during both the growth and condensation periods. The ejection velocities of the bubbles were in the range of 0.36-1.13 m/s.

4. The effect of flow velocity on bubble parameters was found to be negligible in the range of this study. This was due to the translation of the bubbles with the cross-flow.

5. At low subcooling, the bubble radius, bubble growth time and condensation time decreased with an increase in the heat flux. The density of the nucleation sites and frequency of bubble formation were increased with an increase in the heat flux. At high subcooling, the bubble maximum radius, growth time, and condensation time were independent of the heat flux.

6. Bubble growth time and condensation time were proportional to the maximum radius. The ratio of bubble growth time to bubble lifetime fell in a range of 0.27-0.44 with an average value of 0.33±0.04.

7. Bubble growth and collapse curves were normalized with maximum bubble radius and bubble lifetime as follows:

$$\frac{R}{R_m} = 1 - 2^{2.2}\left|\frac{1}{2} - \left(\frac{t}{t_b}\right)^{0.67}\right|^{2.2} \tag{4.6}$$

8. Bubble growth rate and maximum bubble radii obtained in this study were compared with bubble growth models of Unal[28], Zuber[23] and Mikic et al.[24]. The experimental growth rates were well predicted by Zuber and Mikic et al.; however the

predictions of the maximum bubble radii did not agree well with the experimental results.

9. Bubble collapse rate and bubble condensation time were compared with the predictions of Akiyama[30] and Florschuetz and Chao[31]. The shape of the collapse curves were similar to the predictions of Akiyama; however the condensation times predicted by Akiyama were two orders of magnitude smaller than found in the present work. The shape of the collapse curve predicted by Florschuetz et al. deviated significantly from those measured in the present experiment.

10. Maximum bubble radius was correlated with wall superheat (Ja_w^*) and liquid bulk subcooling (θ) (average correlation error =20%):

$$R_m^+ = 5.01 \times 10^9 \, Ja_w^{*\,-1.65} \theta^{\,-1.65} \tag{4.10}$$

11. Bubble growth time was correlated with the same non-dimensional parameters as the maximum bubble radius. A simple expression was found relating the growth time to maximum bubble radius (average correlation error =28%):

$$t_m^+ = 3.21 \times 10^{14} \, Ja_w^{*\,-2.58} \theta^{\,-2.88} \tag{4.13}$$

$$t_m = 56.7 \, R_m^{1.49} \tag{4.15}$$

12. Bubble condensation time was correlated to the maximum radius (R_m^+) and liquid bulk subcooling (Ja) (average correlation error = 11.7%):

$$t_c^+ = 106.8 \, Ja^{-0.45} \, R_m^{+\,1.30} \tag{4.18}$$

5.2 Recommendations

1. Measure the temperature profile across the flow to obtain the local subcooling and the thickness of the superheated layer. The temperature measurements would determine the effect of true liquid subcooling and superheating on the bubble growth and collapse.

2. Perform additional experiments with higher flow velocities and different hydraulic diameters to investigate the effect of flow and geometery on the bubble parameters.

3. Investigate the effect of heat flux, local and bulk subcoolings and flow velocity on the density of nucleation sites and frequency of bubble formation as the present models of bubble growth do not include the effect of increased nucleation site density and frequency of bubble formation on bubble parameters.

4. Evaluate the variation of bubble parameters for different nucleation sites.

5. Develop a better method for analyzing the films so that more bubbles are digitized for one condition and statistical methods can be used for analyzing the data.

6. Simulate the bubble growth numerically by the use of different boundary conditions matching the bubble shape observed experimentally. This simulation for different boundary conditions will promote better understanding of the important parameters in bubble growth.

BIBLIOGRAPHY

[1] El-vakil M.M., Nuclear Heat Transport, The American Nuclear Society, (1978).

[2] Kay R.E., Stevens-Guille P.D. and Hillborn J.W., Jervis R.E. 'SLOWPOKE: A New Low-Cost Laboratory Reactor', *International Journal of Applied Radiation and Isotopes*, Vol. 24, pp. 509-518, (1973).

[3] Rogers J.T., Salcudean M., Abdullah Z., Mcleod D. and Poirier D., 'The onset of significant Void in Upflow Boiling of Water at Low Pressure and Velocities', *Int. J. Heat Mass Transfer*, Vol. 30, No. 11, pp. 2247-2260, (1987).

[4] Mcleod R.D., 'Investigation of Subcooled Void Fraction Growth in Water Under Low Pressure and Low Flow rate Conditions', M.A.Sc. Thesis, Carleton University, Ottawa, (1986).

[5] Abdullah Z., 'Investigation of Onset of Significant Void and Void Fraction Under Conditions of Low Pressures and Flow Velocities', B.A.Sc. Thesis, Dept. of Mechanical Engineering, University of Ottawa, (1982).

[6] Bibeau E.L., 'Experimental Investigation of Subcooled Void Growth for Upflow and Downflow at Flow velocities and Low Pressure', M.A.Sc. Thesis, University of British Columbia, (1988).

[7] Salcudean M. and Bibeau E.L., 'Experimental Investigation of Flow Direction Effect on Void Growth at Low velicities and Low pressure', *Second World Conference on Experimental Heat Transfer*, Fluid Mechanics and Thermodynamics, Yugoslavia, (1991).

[8] Bibeau E.L. and Salcudean M., 'The effect of flow direction on Void Growth at Low Velocities and Low Pressure', *Int. Comm. Heat Transfer*, Vol. 17, pp. 19-25, (1990).

[9] Bibeau E.L. 'Void Growth in Subcooled Flow Boiling for Circular and Finned Geometries for Low Values of Pressure and Velocity', Ph.D. Thesis, University of British Columbia, (1993).

[10] Rouhani S.Z. 'Calculation of Steam Volume Fraction in Subcooled Boiling', *J. of Heat Transfer*, Vol. 90, pp. 158-163, (1968).

[11] Rouhani S.Z. and Axelsson E., 'Calculation of Void Volume Fraction in the Subcooled and Quality Boiling Regions', *J. of Heat Transfer*, Vol. 13, pp. 383-393, (1970).

[12] Chatoorgoon V., 'A Generation-Condensation Void Transport Model for Low Pressure', *AECL Publication*, (1992).

[13] Tsung-Chang G. and Bankoff S.G., 'On the Mechanism of Forced Convection Subcooled Nucleate Boiling', *J. Heat Transfer*, Vol.112, pp. 213-218, (1990).

[14] Dhir V.K., 'Nucleate and Transition Boiling Heat Transfer under Pool and External Flow Conditions', *International Heat Transfer Conference, 9th*, Proc, Jerusalem, Israel, Vol. 1, pp.129, (1990).

[15] Van Stralen S.J.D., 'The Growth rate of Vapor Bubbles in Superheated Pure Lquids and Binary Mixtures', *Int. J. Heat Mass Transfer*, Vol. 11, pp. 1467-1489, (1968).

[16] Mayinger F. and Chen Y.M., 'Heat Transfer at the Phase Interface of Condensing bubbles', *Int. Heat Transfer Conference, 8th* , San Fransisco, USA, Vol.4, pp. 1913-1918, (1986).

[17] Collier J.G., Convective Boiling and Condensation, McGraw-Hill, (1972).

[18] Strenge P.H., Orell A. and Westwater J.W., 'Microscopic Study of Bubble Growth During Nucleate Boiling', *A.I.Ch.E. Journal*, Vol.7, No.4, pp. 578-583, (1961).

[19] Plesset M.S. and Zwick S.A., 'The Growth of Vapor Bubbles in Superheated Liquids', *J. Appl. Phys.*, Vol. 25, pp. 493-500, (1954).

[20] Forster H.K. and Zuber N., 'Growth of vapor bubbles in superheated liquid', *J. Appl. Phys.*, Vol. 25, No.4, pp. 474-478, (1954).

[21] Plesset M.S. and Zwick S.A., 'A Nonsteady Heat Diffusion Problem with Spherical Symmetry', *J. Appl. Phys.*, Vol. 23, No. 1, pp. 95-98, (1952).

[22] Mikic B.B., Rohsenow W.M. and Griffith P., 'On Bubble Growth Rates', *Int. J. Heat Mass Transfer*, Vol. 13, pp. 657-666, (1970).

[23] Zuber N., 'The dynamics of vapor bubbles in nonuniform temperature fields', *Int. J. Heat Mass Transfer*, Vol. 2, pp. 83-98, (1961).

[24] Mikic B.B. and Rohsenow W.M., 'Bubble Growth rates in non-uniform temperatures field', *Progress in Heat and Mass Transfer*, Vol. 2, pp. 283-293, (1969).

[25] Cooper M.G. and LLoyd A.J.P., 'The Microlayer in Nucleate Pool Boiling', *Int. J. Heat Mass Transfer*, Vol.12, pp. 895-913, (1969).

[26] Cooper M.G., 'The Microlayer and Bubble Growth in Nucleate Pool Boiling', *Int. J. Heat Mass Transfer*, Vol. 12, pp.915-933, (1969).

[27] Sernas V. and Hooper F.C., 'The Initial Vapor Bubble Growth on a Heated Wall During Nucleate Boiling', *Int. J. Heat Mass Transfer*, Vol.12, pp. 1627-1639, (1969).

[28] Unal H.C., 'Maximum Bubble Diameter, Maximum Bubble-Growth Time And Maximum Bubble-Growth Rate During the Subcooled Nucleate Flow Boiling of Water up to 1.77 MPa', *Int. J. Heat Mass Transfer*, Vol. 19, pp. 643-649, (1976).

[29] Srinivas N.S. and Kumar R., 'Prediction of Bubble Growth Rates and Departure Volumes in Nucleate Boiling at Isolated Sites', *Int. J. Heat Mass Transfer*, Vol.27, No. 8, pp.1403-1409, (1984).

[30] Akiyama M., 'Spherical Bubble Collapse in Uniformly Subcooled Liquids', *Bulletin of JSME*, Vol. 8, pp. 683-694, (1965).

[31] Florschuetz L.W. and Chao B.T., 'On the Mechanics of Vapor Bubble Collapse', *J. of Heat Transfer, Trans. ASME, Series C*, Vol. 87, pp. 209-220, (1965).

[32] Voloshko A.A. and Vurgaft A.V., 'Study of Condensation of Single Vapor Bubbles in a Layer of Subcooled Liquid', *Heat Transfer-Soviet Research*, Vol. 3, No. 2, pp.160-164, (1971).

[33] Unal H.C., 'Determination of the Initial Point of Net Vapor Generation in Flow Boiling Systems', *Int. J. Heat Mass Transfer*, Vol.18, pp.1095-1099, (1975).

[34] Shoukri M., Donevski B., Judd R.L. and Dimmick G.R., '*Experiments on Subcooled Flow Boiling and Condensation in Vertical Annular Channels*', International Conference in Multiphase Flow, Yugoslavia, May 14-18, (1990).

[35] Gunther F.C., 'Photographic Study of Surface-Boiling Heat Transfer to Water with Forced Convection', *ASME Transactions*, Vol. 73, pp. 115-123, (1951).

[36] Abdelmessih A.H., Hooper F.C. and Nangia S., 'Flow Effects on Bubble Growth and Collapse in Surface Boiling', *Int. J. Heat Mass Transfer*, Vol. 15, pp. 115-125, (1972).

[37] Del Valle V.H. and Kenning D.B.R., 'Subcooled Flow Boiling at High Heat Flux', *Int. J. Heat Mass Transfer*, Vol. 28, No. 10, pp. 1907-1920, (1985).

[38] Akiyama M. and Tachibana F., 'Motion of Vapor Bubbles in Subcooled Heated Channel', *Bulletin of JSME*, Vol. 17, No. 104, pp. 241-247, (1974).

[39] Tolubinsky V.I. and Kostanchuk D.M., 'Vapor bubble Growth Rate and Heat Transfer Intensity at Subcooled Water Boiling', *Int. Heat Transfer Conference, 4th, Paris*, Vol. V, Paper B2.8, (1970).

[40] Kamei S. and Hirata M., 'Condensing Phenomena of a Single Vapor Bubble into Subcooled Water', *Experimental Heat Transfer*, Vol. 3, pp. 173-182, (1990).

[41] Kamei S. and Hirata M., 'Study on Condensation of a Single Vapor Bubble into Subcooled Water, Part 2 - Experimental Analysis', (1990).

[42] Tao Z., Simpson H.C. and Bradford A.M., 'Steam Bubble Formation and Detachment at a Submerged Orifice in Subcooled Water', *Int. Heat Transfer Conference, 9th*, Jerusalem, Israel, Vol. 6, pp. 101-106, (1990).

[43] Simpson H.C., Beggs G.C and Isikan O.M., 'Collapse of Steam Bubbles in Subcooled Water', *Int. Heat Transfer Conference, 8th*, San Fransisco, USA, Vol.4, pp.1919-1924, (1986).

[44] Brucker G.C. and Sparrow E.M., 'Direct Contact Condensation of Steam Bubbles in Water at High Pressure', *Int. J. Heat Mass Transfer*, Vol.20, pp .371-381, (1977).

[45] Hahne E., Spindler K. and Shen N., 'Incipience of Flow Boiling in Subcooled Well Wetting Fluids', *Int. Heat Transfer Conference, 11th, Proc, Jerusalem*, Vol. 2, pp. 69-74, (1990).

[46] Hino R. and Ueda T., 'Studies on Heat Transfer and Flow Characteristics in Subcooled Flow Boiling-Part2. Flow Characteristics', *Int. J. Multiphase Flow*, Vol. 11, No. 3, pp. 283-297, (1985).

[47] Beer F.B. and Johnston E.R., Vector Mechanics for Engineers, McGraw-Hill, (1984).

[48] Jiji L.M. and Clark J.A., 'Bubble Boundary Layer and Temperature Profiles for Forced Convection Boling in Channel Flow', *J. of Heat Transfer*, Transaction of the ASME, Vol.86, pp. 50-58, (Feb. 1964).

[49] Forster K. E., 'Growth of a Vapor-Filled Cavity near a Heating Surface and Some Related Questions', *The Physics of Fluids*, Vol. 4, No.4, pp. 448-455, (April 1961).

[50] Cooper M.G., Mori K. and Stone C.R., 'Behaviour of Vapour Bubbles Growing at a Wall with Forced Flow', *Int. J. Heat Mass Transfer*, Vol.26, No.10, pp. 1489-1507, (1983).

[51] Dimic M., 'Collapse of One-Component Vapor Bubble with Translatory Motion', *Int. J. Heat Mass Transfer*, Vol. 20, pp.1325-1332, (1977).

[52] Devore J.L., Probability and Statistics for Engineering and the Sciences, Wadsworth Inc., (1987).

Appendix A

Bubble Growth Model (Mikic[22])

In this approach the total kinetic energy of the moving liquid at any time is equal to the work done at the liquid boundaries. The bubble is assumed to be spherical, and expanding in an infinite incompressible liquid. The kinetic energy of the liquid is given by:

$$K.E. = \frac{\rho_l}{2}\int_R^\infty u^2 d(Vol) \tag{A.1}$$

where u is the radial velocity of the liquid element. The equation of continuity is given by:

$$u = \left(\frac{R}{r}\right)^2 \dot{R} \tag{A.2}$$

Substituting (A.1) into (A.2) and integrating yields:

$$K.E. = 4\pi\frac{\rho_l}{2}\int_R^\infty \left\{\dot{R}\left(\frac{R}{r}\right)^2\right\}^2 r^2 dr = 2\pi\rho_l R^3 \dot{R}^2 \tag{A.3}$$

The net work to the liquid is expressed as:

$$W = 4\pi\int_0^R (p_v - p_\infty) R^2 dR \tag{A.4}$$

Assuming that the variation in the vapour pressure during the bubble growth is not large, (A.4) can be approximated by:

$$W \cong \frac{4}{3} R^3 (p_v - p_\infty) \tag{A.5}$$

Equating the net work done on the liquid boundary (A.5) with the total kinetic energy (A.3), one obtains:

$$\dot{R}^2 = \frac{2}{3}\frac{p_v - p_\infty}{\rho_l} \tag{A.6}$$

The pressure difference in Equation (A.6) can be approximated with the Clausius-Clayperon equation:

$$p_v - p_\infty = \frac{\rho_v i_{fg}(T_v - T_{sat})}{T_{sat}} \tag{A.7}$$

Using (A.7), Equation (A.6) becomes:

$$\dot{R}^2 = A^2 \frac{T_v - T_{sat}}{\Delta T} \tag{A.8}$$

Where

$$A = \left(\frac{2}{3}\frac{i_{fg}\rho_v(T_\infty - T_{sat})}{\rho_l T_{sat}}\right)^{1/2} \quad \text{and} \quad \Delta T = T_\infty - T_{sat} \tag{A.9}$$

A relationship expressing the rate of bubble growth with the vapour temperature was given by Plesset and Zwick [19] for bubble growth in an initially superheated liquid due to a constant temperature difference $(T_\infty - T_v)$:

$$\dot{R} = \frac{1}{2}\frac{B}{\sqrt{t}}\left(1 - \frac{T_v - T_{sat}}{\Delta T}\right) \tag{A.10}$$

where

$$B = \left(\frac{12}{\pi}\alpha_l\right)^{1/2} Ja^* \tag{A.11}$$

Solving for $\left(\frac{T_v - T_{sat}}{\Delta T}\right)$ in Equation (A.10), substituting in (A.8) and non-dimensionlizing the resulting expression, one obtains:

$$\frac{dR^+}{dt^+} = (t^+ + 1)^{1/2} - (t^+)^{1/2} \tag{A.12}$$

where

$$R^+ = \frac{AR}{B^2} \quad and \quad t^+ = \frac{A^2 t}{B^2} \tag{A.13}$$

Equation (A.12) integrates to:

$$R^{+} = \frac{2}{3}\left[\left(t^{+}+1\right)^{3/2} - \left(t^{+}\right)^{3/2} - 1\right] \tag{A.14}$$

This equation simplifies to Rayleigh's Equation (2.3) at $t^{+} << 1$ and to Plesset and Zwick's Equation (2.12) at $t^{+} >> 1$.

APPENDIX B

Bubble growth model (Unal[28])

Unal[28] assumed that a spherical bubble grows on a very thin, partially dried liquid film formed between the bubble and the heated surface (micro-layer). The bubble growth was due to the evaporation of the microlayer balanced by the dissipation of heat at the bubble top surface (see Figure B.1). The dry area under the bubble is assumed to be circular in shape. Over its growth period, the bubble takes up heat by the evaporation of the very thin liquid film over the area $\frac{\pi D^2}{4}\left(1-\frac{D_d^2}{D^2}\right)$ in which $\frac{D_d}{D}$ is assumed to be constant for a given pressure. The process of growth is assumed to be isobaric. The heat input to the bubble from the superheated layer is neglected compared to the heat from the thin liquid film, since the ratio of the thickness of the superheated layer to the maximum bubble diameter is assumed to be small. The dissipation of heat is assumed to occur at the bubble top surface since the bottom surface faces the heater, and is ineffective in dissipating heat. An overall energy balance on the bubble yields the following equation:

$$q_b \frac{\pi D^2}{4}(1-\frac{D_d^2}{D^2}) = h_{cb}\Delta T_{sub}\frac{\pi D^2}{2} + \frac{\pi}{6}\rho_v i_{fg}\frac{dD^3}{dt} \tag{B.1}$$

with initial condition of $t = 0$ $D = 0$. q_b in Equation (B.1) is the heat flux from the very thin liquid film under the bubble and is given by Sernas and Hooper[27] as follows:

$$q_b = \frac{\Delta T_{sat}\gamma k_l}{\sqrt{\pi\alpha_l t}} \tag{B.2}$$

where ΔT_{sat} is the initial superheat of the very thin liquid layer under the bubble:

$$\Delta T_{sat} = \left(\frac{q - h_{con}\Delta T_{sub}}{C^*}\right)^{1/3} \tag{B.3}$$

$$\gamma = \left(\frac{k_s \rho_s C_s}{k_l \rho_l C_{pl}} \right)^{1/2} \tag{B.4}$$

$$C^* = \frac{i_{fg} \mu_l \left(\dfrac{C_{pl}}{0.013 i_{fg} \Pr^{1.7}} \right)^3}{\left(\dfrac{\sigma}{g(\rho_l - \rho_v)} \right)^{1/2}} \tag{B.5}$$

h_{con} is evaluated from:

$$Nu = 0.023 \mathrm{Re}^{0.8} \Pr^{0.33} \tag{B.6}$$

The condensation heat transfer coefficient at the surface of the bubble, h_{cb}, in (B.1) is given by:

$$h_{cb} = \frac{C \Phi i_{fg} D}{2\left(1/\rho_v - 1/\rho_l \right)} \tag{B.7}$$

where

$$\Phi = \left(\frac{V}{V_o} \right)^{0.47} \quad for \quad V > 0.61 \ (m/s) \qquad V_o = 0.61 \ (m/s) \tag{B.8}$$

$$\Phi = 1 \quad for \quad V \leq 0.61 \ (m/s) \tag{B.9}$$

and C is pressure dependent constant. Substituting (B.2) and (B.7) in equation (B.1) yields the following equation:

$$\frac{dD}{dt} = a \alpha t^{-1/2} - C \Phi b D \tag{B.10}$$

where

$$a = \frac{(\Delta T_{sat} k_l \gamma)}{2 \rho_v i_{fg} (\pi \alpha_l)^{1/2}} \tag{B.11}$$

$$b = \frac{\Delta T_{sub}}{2\left(1 - \rho_v/\rho_l\right)} \tag{B.12}$$

$$\alpha = \left(1 - D_d^2/D^2\right) \tag{B.13}$$

Solution of equation (B.10) is given as follows:

$$D(t) = \frac{2a\alpha t^{1/2}(1 + \frac{1}{3}bC\Phi t)}{(1 + C\Phi bt)} \tag{B.14}$$

Differentiating (B.14) and equating to zero, the maximum diameter is obtained:

$$D_m = 1.21\frac{a\alpha}{(bC\Phi)^{1/2}} \tag{B.15}$$

$$t_m = \frac{1}{1.46bC\Phi} \tag{B.16}$$

To be able to calculate $D(t), D_m$ and t_m with the equation (B.14), (B.15) and (B.16), α and C must be known. Unal has shown that the value of $\frac{\alpha}{C^{1/2}}$ is constant for a given pressure and its value is found empirically from the experimental data available in the literature. The value of $\frac{\alpha}{C^{1/2}}$ is therefore correlated to the pressure as follows:

$$\frac{\alpha}{C^{1/2}} = 2 \times 10^{-5} P^{0.709} \tag{B.17}$$

By substituting (B.17) in (B.15), the maximum bubble diameter for atmospheric pressure becomes:

$$D_m = \frac{2.42 \times 10^{-5} a}{(b\Phi)^{1/2}} \tag{B.18}$$

where a, b and Φ are defined by (B.11), (B.12), (B.8) and (B.9). The range of applicability of (B.18) is:

$$P = 0.1 - 17.7 \ Mpa,$$

$$q = 0.47 - 10.64 \ MW/m^2,$$

$V = 0.08 \ -9.15 \ m/s,$

$\Delta \ T_{sub} = 3\text{-}86 \ K,$

$D_m = 0.08 \ -1.24 \ mm$

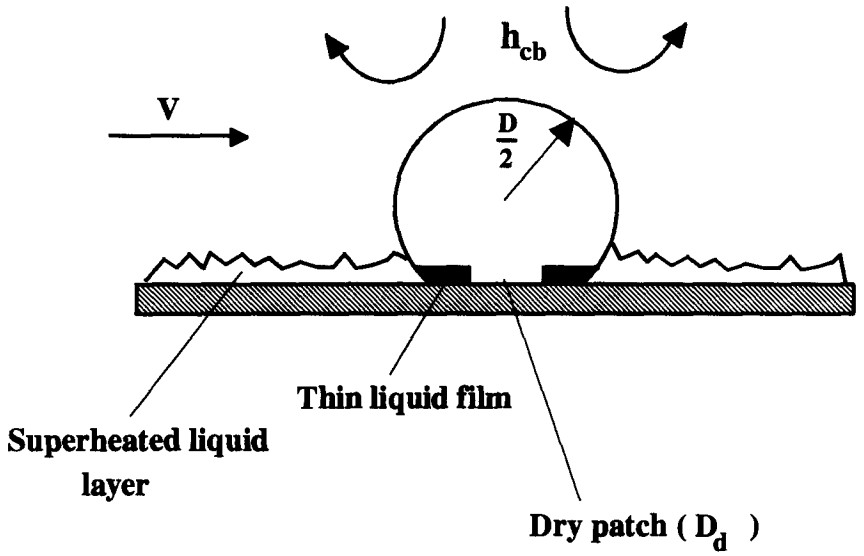

Figure B.1. Bubble growth model proposed by Unal[28].

APPENDIX C

Evaluation of Bubble Volume

The following algorithm, written in C programming language, was employed to evaluate the bubble volume:

1. Pixels comprising the bubble projection area were scanned.
2. The area of projection of bubble was evaluated:

$$A = \int dA = A_{pixel} N_{pixel} = h^2 N_{pixel} \tag{C.1}$$

where $A_{pixel}(mm^2)$ is the area of a single pixel and N_{pixel} is the total number of pixels contained inside the contour of the bubble and including the pixels on the contour. A pixel was assumed to be square in shape with the dimension h *(mm/pixel)*. For a magnification of twenty times on the monitor, the value of h (screen resolution) was approximately *0.02 (mm/pixel)*.

3. Bubble centroid was found next by integrating the pixels as follows:

$$\bar{x} = \frac{1}{A}\int_A x dA = \frac{1}{A}\sum_{pixel=top}^{bottom}\sum_{pixel=left}^{right}\left(hx_{pixel} - \tfrac{1}{2}h\right)h^2 = \frac{h}{N_{pixel}}\sum_{pixel=top}^{bottom}\sum_{pixel=left}^{right}\left(x_{pixel} - \tfrac{1}{2}\right) \tag{C.2}$$

$$\bar{y} = \frac{1}{A}\int_A y dA = \frac{1}{A}\sum_{pixel=top}^{bottom}\sum_{pixel=left}^{right}\left(hy_{pixel} - \tfrac{1}{2}h\right)h^2 = \frac{h}{N_{pixel}}\sum_{pixel=top}^{bottom}\sum_{pixel=left}^{right}\left(y_{pixel} - \tfrac{1}{2}\right) \tag{C.3}$$

where x_{pixel}, y_{pixel} are the coordinates of the pixel (see Figure C.1).

4. The x-, y- and xy-moments of inertia of the projection area were found as follows:

$$I_x = \sum_A \left(I_{x'} + A_{pixel} y^2\right) = h^4 \sum_{pixel=top}^{bottom}\sum_{pixel=left}^{right}\left(\tfrac{1}{12} + \left(y_{pixel} - \tfrac{1}{2}\right)^2\right) \tag{C.4}$$

$$I_y = \sum_A \left(I_{y'} + A_{pixel}x^2\right) = h^4 \sum_{pixel=top}^{bottom} \sum_{pixel=left}^{right} \left(\tfrac{1}{12} + \left(x_{pixel} - \tfrac{1}{2}\right)^2\right) \tag{C.4}$$

$$I_{xy} = \sum_A \left(I_{x'y'} + Axy\right) = h^4 \sum_{pixel=top}^{bottom} \sum_{pixel=left}^{right} \left\{\left(x_{pixel} - \tfrac{1}{2}\right)\left(y_{pixel} - \tfrac{1}{2}\right)\right\} \tag{C.6}$$

where

$$I_{x'} = I_{y'} = \tfrac{1}{12}h^3 h \quad \text{and} \quad I_{x'y'} = 0 \tag{C.7}$$

5. The centroidal moments of inertia were found by the use of the parallel axis theorem: (see Figure C.2):

$$\bar{I}_{x''} = I_x - A\bar{y}^2 \tag{C.8}$$

$$\bar{I}_{y''} = I_y - A\bar{x}^2 \tag{C.9}$$

$$\bar{I}_{x''y''} = I_{xy} - A\bar{x}\,\bar{y} \tag{C.10}$$

6. The orientation of the of the principal centroidal axis of the area was found from [47]:

$$\tan 2\theta = -\frac{2\bar{I}_{x''y''}}{\bar{I}_{x''} - \bar{I}_{y''}} \tag{C.11}$$

where θ is the angle shown in Figure C.2.

7. These axis were drawn on the bubble and the axis of symmetry was chosen .
8. The area on both side of the axis of symmetry was evaluated and the centroid of each area was found in the same manner.
9. The volume of revolution of the areas on each side of the axis of symmetry was found as follows:

$$Vol_1 = 2\pi l_1 A_1 \tag{C.12}$$

$$Vol_2 = 2\pi l_2 A_2 \tag{C.13}$$

where l_1 and l_2 are distances as shown in Figure C.3.

10. The total volume was defined by the average volumes of revolution from equations (C.12) and (C.13):

$$Vol = \frac{Vol_1 + Vol_2}{2} \tag{C.14}$$

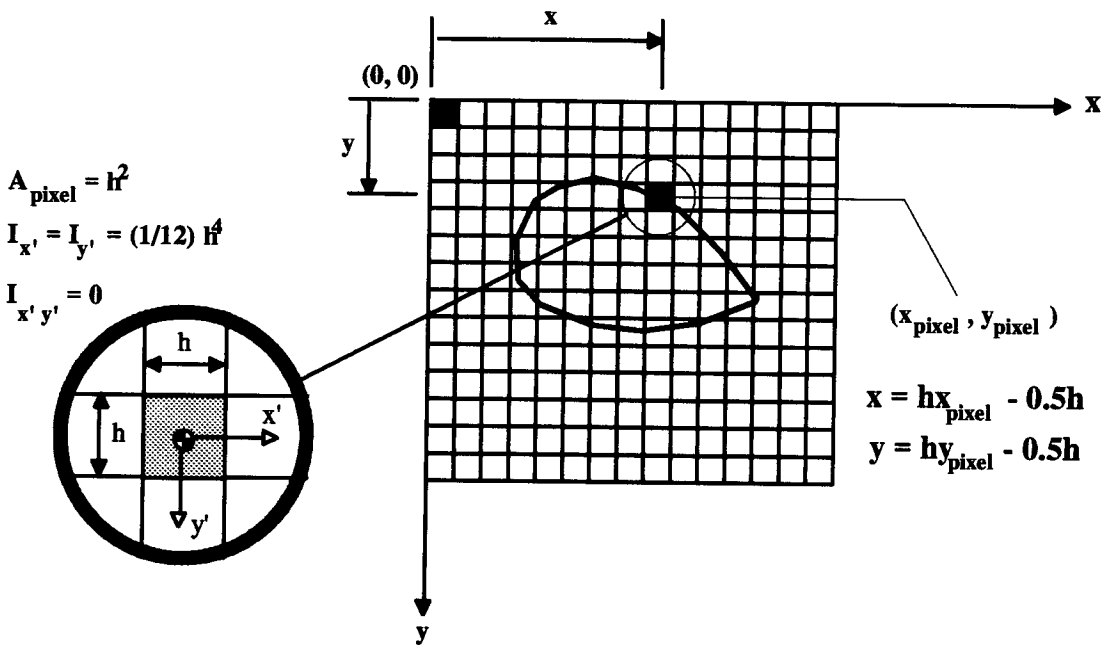

Figure C.1. Nomenclature used in pixel integration.

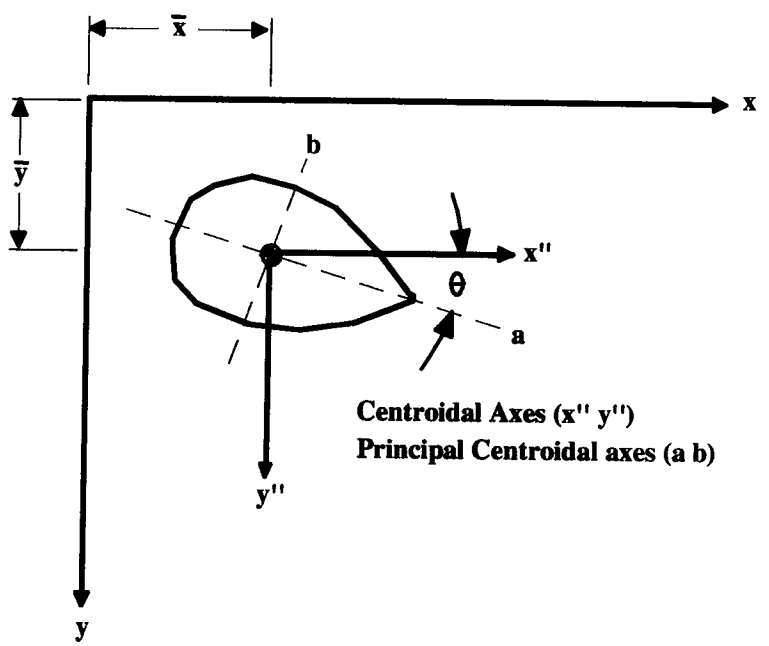

Figure C.2. Schematic diagram of the centroidal principal axes of the bubble.

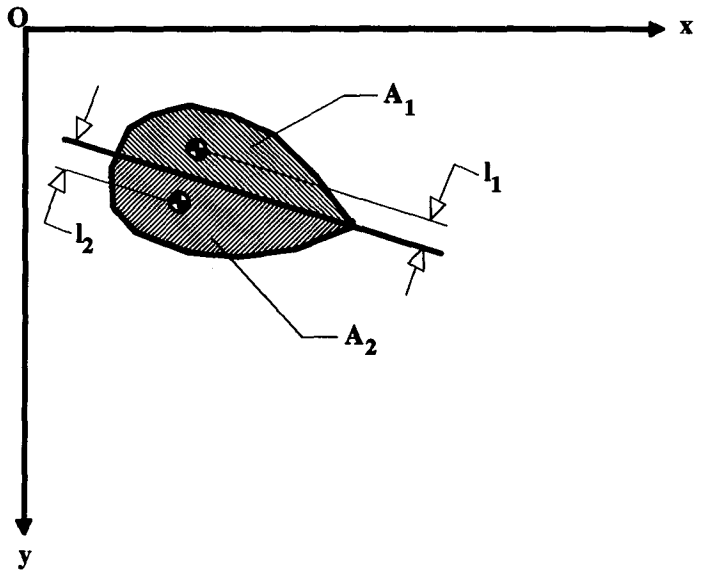

Figure C.3. Nomenclature used in evaluating the volume of revolution.

Appendix D

Error Analysis

Table D.1. lists the errors in the measured quantities in the experiment. The errors were either estimated from the manufacturers' specifications or obtained from reference[9].

Table D.1. Estimated errors in the measured quantities.

Measured Quantity	Estimated Error
Flow rate	±0.3%
Current	±1%
Voltage	±1%
Inlet temperature	±1 °C
Wall temperature	-2.2/+1.2 °C
Glass tube diameter	±0.09%
Heater diameter	±0.15%
Heater length	±0.2%

Inlet and wall temperature: The error in the temperature measurements consisted of the inherent error in the calibration of the thermocouple plus the error in the calibration of the instrumentation ($d(T_{in})=\pm\ 1\ ^\circ\ C$, $d(T_w)=\pm\ 1.7\ ^\circ\ C$). In the case of the wall temperature measurements, an additional error was present due to convection of heat from the stripped end of the thermocouple (7 mm). The error in the temperature measurement due to effect of forced convection was estimated to be -0.5 °C [9].

Heat flux: The error in the heat flux measurements was calculated mathematically from the uncertainty of the input power measurements (± 2%) i.e. error in the measurements of voltage and current.

Bulk subcooling: The error in the calculated bulk temperature at the filming location was calculated mathematically by differentiating the following with respect to inlet temperature, heat flux and mass flow rate:

$$T_B = T_{in} + \frac{\phi P l}{\dot{m} C_{pl}} \tag{D.1}$$

$$dT_B = \frac{\partial T_B}{\partial T_{in}} dT_{in} + \frac{\partial T_B}{\partial \phi} d\phi + \frac{\partial T_B}{\partial \dot{m}} d\dot{m} \tag{D.2}$$

$$dT_B = dT_{in} + (T_B - T_{in})\left[\frac{d\phi}{\phi} + \frac{d\dot{m}}{\dot{m}}\right] \tag{D.3}$$

The maximum temperature difference between the inlet and the filming location was 60°C. The various error terms in (D.3) are given in table D.1.

$$d(\Delta T_{sub}) = dT_B \cong (1°C) + (60°C)(0.020 + 0.003) = \pm 2.4°C$$

Time: The error in the time measurement is made up of: error in the assumption of constant film speed (0.01 ms); accuracy of the pulse generator (±0.01 ms); and the error in zero time. In this experiment, the zero time corresponds to the frame preceeding the first appearance of the bubble. At a camera speed of 5000 fps the zero time error will be 1/(5000fps) = 0.2 ms. In this experiment since the same convention is used to determine the zero time for every bubble cycle, this error is not added to the overall error in the time measurement .

Volume, Normal and Parallel diameters: Errors were calculated by measuring the volume, and maximum and minimum diameters of an apple with the pixel integration technique and comparing it with the direct measurement of the volume of the apple (±5%).

Radius: Error in the radius was obtained by differentiating Equation (3.5):

$$\frac{dR}{R} = \frac{1}{3}\frac{d(Vol)}{Vol} = \frac{1}{3} \times 0.05 = \pm 1.67\%$$

Normal and Parallel Displacement: Errors included uncertainty in the location of the nucleation site (2 pixels) and uncertainty of the centroid (2 pixels). The resolution of magnified images were 0.02 mm/pixel.

Repeatability of Results Obtained from Film Analysis: Figure D.1-D.3 show the digitization results for condition D22-30 for two different measurements of the same bubble cycle. The error involved in the repeatability of the digitization results is due to the tracing of the bubble outline and is caused by human error.

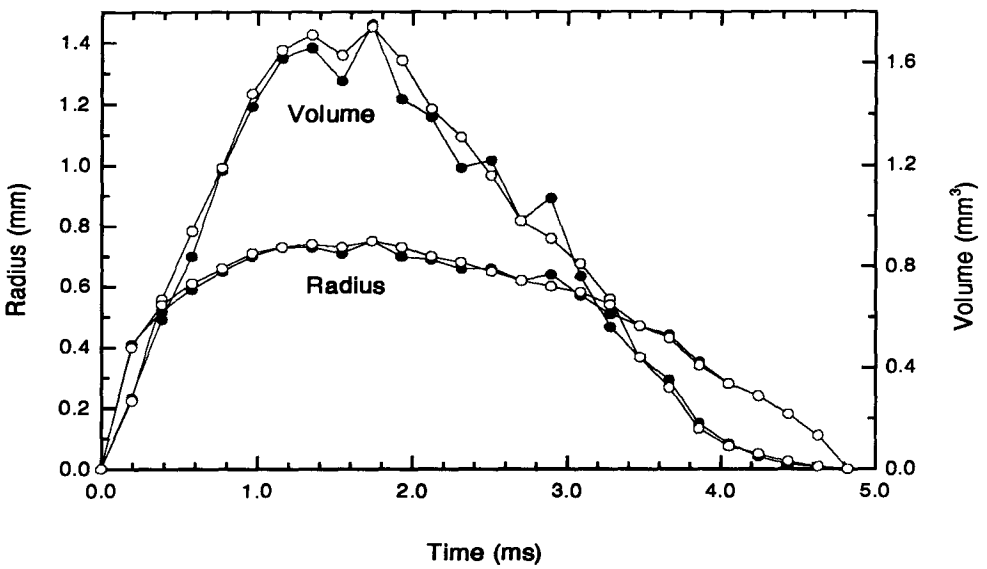

Figure D.1. Repeatability of bubble volume and radius measurements

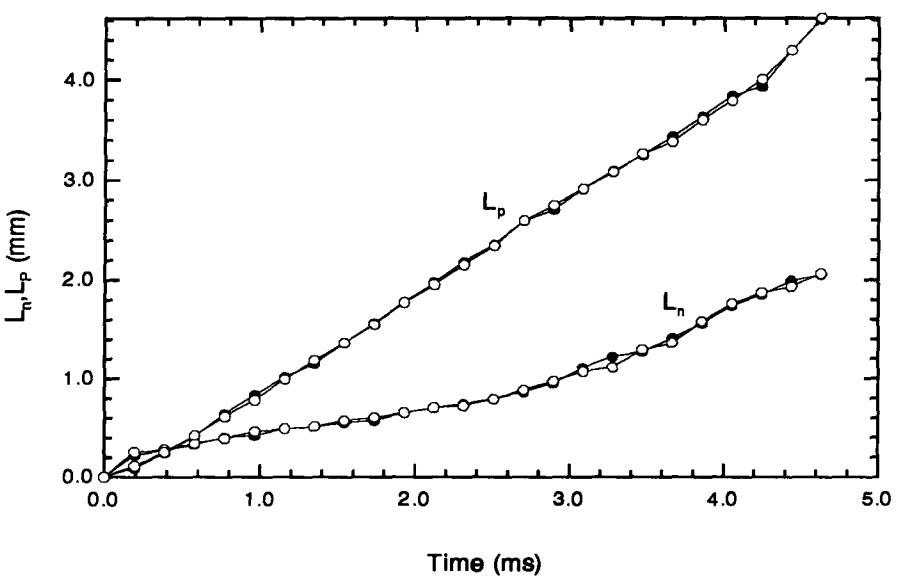

Figure D.2. Repeatability of normal and parallel displacement measurements.

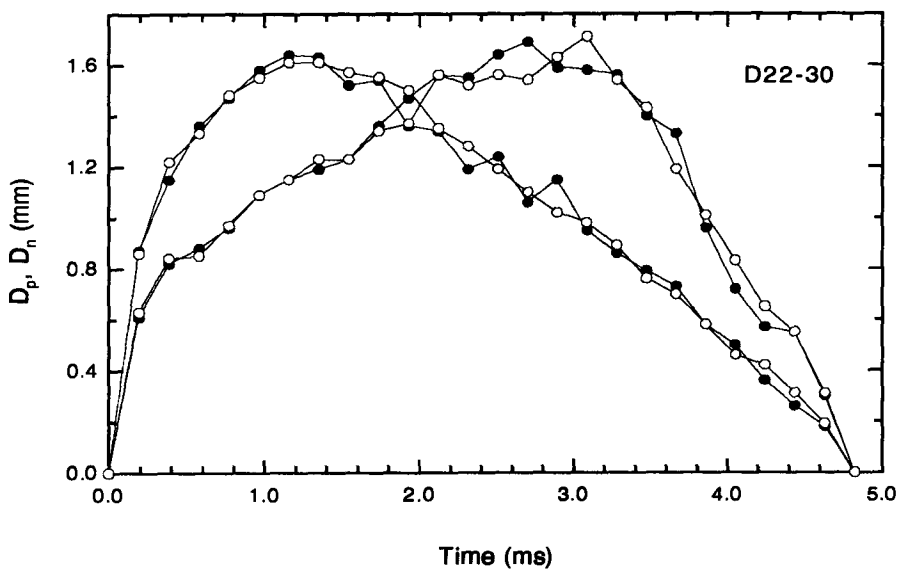

Figure D.3. Repeatability of measurements of diameters normal and parallel to centroidal principal axis of bubble.

Appendix E

A Sample of Correlation Procedure

The following general form was assumed to correlate the bubble maximum radius with experimental conditions:

$$R_m^+ = KJa_w^{*x}\theta^y \tag{E.1}$$

where K, x, and y are constants to be determined from multiple regression analysis. Equation (E.1) was linearised by taking the log on both sides of the expression:

$$\ln R_m^+ = \ln K + x \ln Ja_w^* + y \ln \theta \tag{E.2}$$

Using the least square method, the values of the constants in (E.2) were obtained from the solution of the following matrix[52]:

$$\begin{bmatrix} \ln K \\ x \\ y \end{bmatrix} = \begin{bmatrix} n & \sum \ln Ja & \sum \ln \theta \\ \sum \ln Ja_w^* & \sum (\ln Ja_w^*)^2 & \sum \ln Ja_w^* \ln \theta \\ \sum \ln \theta & \sum \ln \theta \ln Ja_w^* & \sum (\ln \theta)^2 \end{bmatrix}^{-1} \begin{bmatrix} \sum \ln R_m^+ \\ \sum \ln R_m^+ \ln Ja_w^* \\ \sum \ln R_m^+ \ln \theta \end{bmatrix} \tag{E.3}$$

where n is the number of different conditions tested and $\sum = \sum_n$. The coefficient of multiple determination (R^2) is defined as:

$$R^2 = 1 - \frac{\sum (y_i - \hat{y}_i)^2}{\sum (y_i - \bar{y}_i)^2} \tag{E.4}$$

where y is the experimental value, $\hat{y}$ is the predicted value based on the correlation, and $\bar{y}$ is the average of experimental values (y is denoted as the parameter to be correlated, i.e., in this case R_m^+).